X-671-74-33

PREPRINT

NASA TM X- 70803

HYDRODYNAMIC MODELS OF A CEPHEID ATMOSPHERE

ALAN H. KARP

(NASA-TM-X-70803) HYDRODYNAMIC MODELS OF A CEPHEID ATMOSPHERE Ph.D. Thesis - Maryland Univ., College Park (NASA) 192 p HC $7.00 CSCL 03A
N75-15520
Unclas
G3/89 07328

NOVEMBER 1974

GODDARD SPACE FLIGHT CENTER
GREENBELT, MARYLAND

For information concerning availability
of this document contact:

Technical Information Division, Code 250
Goddard Space Flight Center
Greenbelt, Maryland 20771

(Telephone 301-982-4488)

HYDRODYNAMIC MODELS OF A CEPHEID ATMOSPHERE

by

Alan H, Karp

Work performed under the auspices of the Laboratory for Optical Astronomy, Code 670, Goddard Space Flight Center, Greenbelt, Maryland and presented as a dissertation for the Ph.D. at the University of Maryland, College, Park, Md.

ABSTRACT

A method for including the solution of the transfer equation in a standard Henyey type hydrodynamic code has been developed. This modified Henyey method has been used in an implicit hydrodynamic code to compute deep envelope models of a classical Cepheid with a period of 12^d including radiative transfer effects in the optically thin zones.

There are two secondary features on the light curve of the model, a shoulder during rising light and a distinct bump during falling light. It is shown that the shoulder during rising light is caused by a deep envelope pressure wave and that the bump during falling light may be due to an atmospheric oscillation. It is shown that the atmospheric oscillation mechanism is consistent with the Hertzsprung sequence and the period-luminosity relation.

The structure of each hydrodynamic model was used as a snapshot of the temperature and pressure structure of the atmospheric layers. After using line blocking factors to account for the effect of spectral lines on the spectral energy distributions computed for the models, broad band UBVRI colors were calculated. The light and color curves of the models reproduce the observed amplitude and asymmetry of Cepheids in this period range. In addition, the color-T_{eff}

relations derived from the models were found to agree with those derived independently. It was found that the colors of the equilibrium model are best reproduced if the intensity mean of the magnitudes, $<B>_I - <V>_I$, is used to compute mean colors. It was also found that loops in the (U-B)-(B-V) diagram are probably due to the dependence of the continuous opacity on the electron pressure.

Line profiles were then computed using the moving atmospheres from the hydrodynamic models. It was found that the velocity gradients in the atmosphere are not responsible for the large microturbulent velocities observed in Cepheids but may be responsible for the occurrence of supersonic microturbulence. The total observed microturbulence was found to be consistent with the linear sum of the classical microturbulence and that caused by the velocity gradients. It was also found that the splitting of the cores of the strong lines is due to shock induced temperature inversions in the line forming region.

The adopted light, color, and velocity curves were used to study three methods frequently used to determine the mean radii of Cepheids. It was found that an accuracy of 10% is possible only if high quality observations are used.

ACKNOWLEDGEMENTS

In principle, a doctoral dissertation represents the work of an individual. In practice, however, many people make important contributions. Heading the list of people I would like to thank is my thesis advisor, Dr. J. P. Harrington. His probing questions and incisive suggestions were of immeasurable help. I was also fortunate enough to have two unofficial advisors, Drs. David Fischel and Warren Sparks. They were always available when problems arose, and they made the thesis work very much easier. The other members of my thesis committee also contributed. Dr. Roger Bell, in addition to supplying the line blocking factors and the continuous opacity code, was always able to answer my questions about stellar atmospheres. Dr. W. K. Rose, who first suggested the atmospheric oscillation mechanism to me, was a great help when problems arose during the hydrodynamic calculations.

There are several others I would like to thank: Drs. W. M. Sparks and G. S. Kutter for supplying the implicit hydrodynamic code that provided the basis for this work, Dr. D. S. King for providing the opacity and equation of state tables, Dr. D. A. Klinglesmith who generated the plates, Dr. S. B. Parsons for sending me copies of his model atmospheres on computer cards, Denise Lengyel-Frey, for suggesting the method used to find the velocity of a spectral line with a split core. In addition, Dr. John Fowler helped greatly by teaching me how to use the computer system efficiently. My thanks also go to the staff of the Laboratory for Optical Astronomy at Goddard Space Flight Center for providing an amiable atmosphere in which to work.

I would also like to thank Nancy Rosander and Robin Farber for typing the manuscript and Paul Marionni for helping with the proofreading and preparation of the text.

Above all others I would like to thank my wife, Nancy, for her patience and understanding. Above and beyond the moral support she provided, she typed the drafts of the manuscript and made numerous improvements to the text.

Computer time was provided under the budget of the Laboratory for Optical Astronomy, Goddard Space Flight Center, NASA. Financial support provided by NASA grant NGL 21-002-033 is gratefully acknowledged.

TABLE OF CONTENTS

LIST OF FIGURES

Plate

LIST OF TABLES

NOTATION

The choice of notation always presents a problem. One would like to have each symbol represent a single quantity. On the other hand, one would also like to use standard notation wherever possible. These two criteria are often incompatible. In the following standard notation is used whenever possible. If a symbol has more than one meaning, the context in which it is used is sufficient to remove any ambiguity. The following is a partial list of the symbols used.

a	radiation density constant = 7.565 x 10^{-15} erg cm^{-3} deg^{-4}
B	$L/L_\odot$, or Planck function
B_λ	monochromatic Planck function
b'	$k/\mu m_H$
c	speed of light = 2.998 x 10^{10} cm s^{-1}
E	total energy
E_{ion+ex}	energy contained in ionization and excitation of atoms
E_r	radiation energy density
F_λ	flux in erg s^{-1} cm^{-2} $Å^{-1}$
F_ν	flux in erg s^{-1} cm^{-2} H_z^{-1}
g	gravitational acceleration
G	gravitational constant = 6.668 x 10^{-8} dyn cm^2 g^{-2}
I	specific intensity, or identity matrix
L	luminosity
m	mass inside a shell of radius r
m_H	mass of hydrogen atom

m_{min}	mass inside base of envelope
M	mass of star, or bolometric magnitude
M_o	mass of star, $M(1+\delta)$ where $\delta \sim 10^{-12}$
N	number of zones in model
P	period of star, or total pressure
P_a	natural period of atmosphere
P_e	natural period of envelope, or electron pressure
P_g	gas pressure
P_r	radiation pressure
P_o	total pressure at surface of model
q	artificial viscosity pressure
Q	pulsation constant = $P\sqrt{\rho}$, or Lagrangian mass coordinate
r	radius
r_o	radius at base of envelope
R	ln r, or stellar radius
S	natural log of Lagrangian mass coordinate
t	time
T	temperature, or effective temperature
T_{eff}	effective temperature
v	velocity
v_o	center of mass velocity of star
V	specific volume = $(\text{density})^{-1}$
W	ln V
Z	ln T
κ	Rosseland mean opacity

κ_c	Continuous opacity
κ_λ	monochromatic opacity
θ	parameter defining implicit-explicit mixture, or angle to line of sight
θ_{eff}	$= 5040/T_{eff}$
λ_o	line center wavelength
$\Delta\lambda_D$	Doppler width
μ	mean molecular weight, or cosine of angle to line of sight
Π	natural log of total pressure
ρ	mean stellar density
σ	Stefan-Boltzmann constant = 5.6692×10^{-5} erg cm^{-2} deg^{-4} s^{-1}
τ	Rosseland mean optical depth
τ_λ	monochromatic optical depth
Φ	phase = fractional part of $(t-t_o)/P$
$\|\|\cdot\|\|$	vector or matrix norm

CHAPTER I

INTRODUCTION

A. Historical review

In 1784, John Goodricke discovered the variability of δ Cephei. However not until 126 years after he published his findings was the importance of Cepheids as distance indicators realized. Although it was known that Cepheids differed from other variables in that their velocity curves are mirror images of their light curves (Belopsky 1895), it was not until 1912 that Leavitt discovered the period-luminosity relation (Pickering 1912). During Leavitt's study of variable stars in the Small Magellanic Cloud, she noticed that the brighter stars have longer periods. Since all stars in the Small Magellanic Cloud are nearly the same distance from the earth, she concluded that the correlation applied equally well to the absolute magnitudes.

Unfortunately, the early attempts by Hertzsprung (1913) and Shapley (1918) to find the zero point of the period-luminosity relation neglected the effects of interstellar absorption and were based on poor data. The resulting error of $1\overset{m}{.}5$ almost exactly compensated for the error introduced by using globular cluster Cepheids to find the absolute magnitudes of RR Lyrae stars. When the absolute magnitudes of RR Lyrae stars were found independently, the results supported Shapley's zero point. It was not until 1952 when Baade was unable to find RR Lyrae stars in M31--stars that he should have been able to see--that the error was discovered (Baade

1956). The importance of Cepheids as distance indicators was demonstrated by this correction which increased both the distance and time scales of the universe by a factor of two.

The discovery of the period-luminosity relation increased the theoreticians' interest in the nature of the Cepheid mechanism. While it was originally thought that Cepheids were binaries, difficulties reconciling this hypothesis with observations suggested that the light and velocity variations were due to radial oscillations. Although Ritter had suggested radial pulsations in 1879, and Shapley had introduced the idea into the astronomical literature in 1914, it was not until 1918 that a thorough study of linear, adiabatic pulsations was published by Eddington. In this work, he derived the period-mean density relation, $P\sqrt{\rho} = Q$, a constant, and showed that the sign of the second order terms dropped from the linearized equations indicated that these terms were responsible for the observed asymmetry of the light curves. He was unable to determine the nature of the driving mechanism but suggested that an increase of the energy generation at minimum radius would produce the desired effect. A more troubling problem was the cause of the 90° phase lag. Linear, adiabatic theory predicts that maximum light should be in phase with minimum radius, not with maximum expansion velocity as observed. If the light and velocity vary sinusoidally, this phase shift is 90°.

Partly because of these difficulties, geometric theories to explain the light and velocity variations were not abandoned. However, in 1926, Baade proposed a test of the pulsation theory. If the star is pulsating, the observations at two phases can be used in the relations

$$\frac{L_1}{L_2} = \frac{R_1^2}{R_2^2} \quad \frac{T_1^4}{T_2^4} \qquad \text{(I-1)}$$

and

$$R_2 - R_1 = \int_1^2 v\, dt \qquad \text{(I-2)}$$

Since he had no knowledge of the color-temperature relation and the necessary velocity measurements had not been made, he was unable to apply this method. The first successful radius determination using this method was made by Becker in 1940, but the results were not very accurate. Wesselink (1946) improved Baade's method by selecting phases of equal color. If equal color was assumed to imply equal temperature, no temperature calibration was needed in equation (I-1). The radius determinations made using Baade's, and later, Wesselink's methods firmly established the validity of the pulsation hypothesis.

The nature of the driving mechanism continued to be a problem. Four possibilities had been suggested:

1. ϵ mechanism: During contraction, the energy generation increases. Since heat is added to the star when it is hottest, thermal energy is converted into mechanical energy (Eddington, 1918).
2. κ mechanism: During contraction, the opacity in some region increases. Since less heat is lost at maximum temperature, the stability of the star is decreased (Zhevakin, 1953).
3. γ mechanism: An ionization zone will remain cool during compression since some energy will be used to ionize the gas. The gas will absorb heat when hottest, destabilizing the star (Cox, Cox, Olsen, King, Eilers, 1966).

4. r mechanism: At minimum radius, the increased curvature of the outer stellar layers traps radiation. Heat is added at maximum temperature, and the stability of the star is reduced (Baker, 1967).

The radius calculations of Becker (1940) indicated that the relative radius variations in Cepheids were too small for the r mechanism to be significant. In 1950, Epstein showed that the radius variations in the stellar core were so small that the ϵ mechanism must be negligible. Linear, nonadiabatic calculations of Baker and Kippenhahn (1962, 1965) and by Cox (1963) demonstrated the effectiveness of both the κ and γ mechanisms in the HeII ionization region.

B. Recent work

There were other problems that could not be investigated with the linear approximation. The nonlinear calculations of Christy, J. Cox, A. Cox, and King, among others (see King and Cox 1968, and Christy 1969, 1970 for references) have been used to study these problems. These models show that the present theories are adequate to describe the gross features of the pulsation such as the approximate light and velocity amplitudes, the phase lag between radius and temperature changes, and the shapes of the light and velocity curves. Other questions remain unanswered. Stobie's (1969c) calculations show that there is a line in the period-luminosity plane separating stars pulsating in the first harmonic from those pulsating in the fundamental. In general, stars with a period less the 7^d should be pulsating in the first harmonic; those with a period over 7^d, in the fundamental. On the other hand, Fernie (1968) has shown that the scatter in the empirical period-radius relation is reduced if some

Cepheids are treated as overtone pulsators. The stars that Fernie suggests are overtone pulsators are not confined to the period range predicted by Stobie. The discrepancy may be due to errors in the radius determinations inherent in the Wesselink method. These errors will be investigated in Chapter VI.

The nature and cause of the phase lag are also problems. Castor (1968) has suggested that the phase lag is caused by the hydrogen ionization region moving through mass as the star pulsates. Using results of linear theory, he concludes that the heat capacity of this region delays light maximum. He states that the rate at which the ionization region sweeps through mass should be in phase with the luminosity. Christy (1968) has studied this problem with his nonlinear calculations and finds that the phase shift through the hydrogen ionization region is only 30°. The remainder of the shift he attributes to skewing of the light curve by nonlinear effects. King, Cox, Eilers, and Davey (1973), on the other hand, find a 90° phase shift in their linear calculations and conclude that the phase lag is a nonadiabatic effect and not a nonlinear effect. The phase lag will be investigated further in Chapter III.

Probably the most worrisome problem is the Cepheid mass discrepancy. Stellar evolution calculations show that the mass of a star near the Cepheid instability strip has a mass given by

$$M_{ev} \sim L^{\frac{1}{4}} \exp\,[2.3\ (X + 3Z)]$$

(Iben and Tuggle, 1972a). Masses of pulsating stars, on the other hand, can be found in one of two ways. The first uses the period-mean density relation, $P\sqrt{\rho} = Q$. Linear calculations can be used to find Q (Epstein 1950; Cogan 1970; Cox, King, and Stellingwerf 1972), and, if the radius can be found, the relationship yields the pulsation mass, M_Q. It should be noted that M_Q is sensitive to errors in the radius, since $M_Q \sim R^3$. The second method uses the phase of the second bump on the light curves of Cepheids with periods between 7^d and 15^d. Christy (1968) has proposed that this bump is the result of a pressure wave which travels into the star, is reflected from the core, and appears at the surface as a second bump on the next pulsation cycle. The time it takes the pressure wave to travel to the core and back is a measure of the stellar radius, while the period of the star depends on both the mass and radius. It is possible, therefore, to find the mass from the phase of the bump, M_Φ. Unfortunately, M_Q and M_Φ are typically half of M_{ev}.

Iben and Tuggle (1972a) have shown that the descrepancy between M_{ev} and M_Q can be removed by increasing the zero point of the period-luminosity relation by $0^m.2$ or adjusting the (B-V)-T_{eff} relation slightly. Fricke, Stobie, and Strittmatter (1971, 1972), however, have shown that the discrepancy cannot be removed if M_Φ is also considered. Since van Genderen (1970) has suggested that more than one mechanism produces bumps on Cepheid light curves, M_Φ may be unreliable. This point is examined further in Chapter III.

More complete reviews of the literature have been given by Rosseland (1949), Ledoux and Walraven (1958), King and Cox (1968), and Fernie (1969).

C. Hydrodynamic Cepheid atmospheres

One of the difficulties with the models discussed above is that they do not adequately represent the Cepheid atmosphere. Since the atmosphere is the only part of the star actually observed, the coarse zoning and use of the diffusion approximation in the optically thin zones of the models makes the comparison of the theoretical and observational results difficult. Recently Keller and Mutschlecner (1970, 1971) and Bendt and Davis (1971) have attempted to remove some of these difficulties by including the effects of radiative transfer. Their emphasis, however, is still on the envelope. In Chapters IV and V, an attempt will be made to answer some of the following questions raised by the observations:

1. How should light and color variations be averaged to best represent the equilibrium state of the star? For example, there is a systematic difference between

$$\frac{1}{P}\int_0^P (B-V)\,dt \qquad \text{and} \qquad -2.5\log\left\{\frac{\int_0^P 10^{-B/2.5}\,dt}{\int_0^P 10^{-V/2.5}\,dt}\right\}.$$

2. Why are weak lines asymmetric near phases of maximum velocity while strong lines are often asymmetric near phases of minimum velocity? For example, Bell and Rodgers (1964) find that the λ4508Å line of FeII is asymmetric in β Dor near the phase of maximum radius.

3. Why are the cores of the strongest lines sometimes split? Grenfell and Wallerstein (1969) and Wallerstein (1972) observe splitting in the core of H_α that indicate velocity differences of up to 100 km s^{-1}. Does this observation indicate actual mass motions or is there another explanation?

4. How well do the observed velocity curves represent the mass motions of the star? Since the continuous opacity scale changes during the pulsation cycle, the observed velocities do not necessarily correspond to a given mass element. The size of the discrepancy between the observed and actual velocity curves is not known.
5. What is the physical nature of the variable microturbulence observed in Cepheids and why is it occasionally supersonic?

These questions can best be answered by computing hydrodynamic model atmospheres. In Chapter II, the method used to compute the models is presented. Chapter III contains a discussion of the properties of the hydrodynamic envelopes including an investigation of the phase lag and second bump. In the next two chapters the models are treated as stellar atmospheres; Chapter IV contains a discussion of the continuous spectrum; Chapter V, a discussion of the line spectrum. The results obtained from these calculations are used in Chapter VI to examine several methods used to find Cepheid radii. Chapter VII summarizes the results and contains suggestions for further work.

CHAPTER II

METHOD OF COMPUTATION

A. Diffusion approximation models*

1. Differential and difference equations.

The hydrodynamic envelope of a Cepheid can be represented in a Lagrangian coordinate system by the following differential equations:

$$\frac{4\pi}{3} \frac{\partial r^3}{\partial m} = V, \qquad \text{(II-1)}$$

$$\frac{\partial v}{\partial t} + 4\pi r^2 \frac{\partial}{\partial m} (P + q) = \frac{-Gm}{r^2} , \qquad \text{(II-2)}$$

$$\frac{\partial E}{\partial t} = -\frac{\partial L}{\partial m} - (P + q) \frac{\partial V}{\partial t} , \qquad \text{(II-3)}$$

$$L = \frac{-256\sigma\pi^2}{3} \frac{r^4 T^3}{K} \frac{\partial T}{\partial m}, \qquad \text{(II-4)}$$

$$\frac{\partial r}{\partial t} = v \qquad \text{(II-5)}$$

representing conservation of mass (II-1), momentum (II-2), and energy (II-3), energy transport by radiation (II-4), and the definition of velocity (II-5). The symbols used are defined in the Notation section. Convection and thermonuclear energy generation have been neglected, and the diffusion approximation for radiative transfer has been used. The boundary conditions are

---

* Most of the material in this section is from working notes prepared by G. S. Kutter and W. M. Sparks. Kutter and Sparks (1972) contains a summary of these notes.

base of envelope: $v=0,\ L=L_0,\ r=r_0$ (II-6)

surface: $P=P_0,\ T^4 = \frac{3}{4}\ T^4_{eff}(\tau + \frac{2}{3})$ (II-7)

where L_0 and r_0 are constants, P_0 is the pressure on the surface, and τ is the Rosseland mean optical depth. When the constitutive equations defining P, q, E, and κ as functions of T and V are included, the differential equations represent a well-defined mathematical problem.

This system of coupled, nonlinear, first-order, partial differential equations cannot be solved analytically. To solve the system of equations numerically, the star is divided into N concentric mass shells whose interfaces are indexed from 1 at the base of the envelope to N+1 at the surface. These mass shells define a Lagrangian grid, $Q_i = 1 - m_i / M_0$, where $M_0 = M(1+\delta)$ and δ is a small number (typically 10^{-12}) used to avoid logarithmic singularities at the surface (Kippenhahn, Weigert, and Hofmeister 1967). The time grid is defined by a set of time steps $\Delta t^{n+\frac{1}{2}} = t^{n+1} - t^n$. In order to decrease the amount of interpolation to be done, the variables v, L, and r are defined at the interfaces while V, T, P, q, E, and κ are defined at the midpoints.

The difference equations at time t^{n+1} are

$$\frac{4\pi}{3M_0}\ \frac{r_i^3 - r_{i-1}^3}{Q_i - Q_{i-1}} = -V_{i-\frac{1}{2}} \qquad \text{(II-8)}$$

$$\frac{v_i - v_i^{\,n}}{\Delta t^{n+\frac{1}{2}}} = (1-\theta)F_i^{\,n} + \theta\, F_i$$

$$+ \frac{4\pi}{M_o Q_i} \quad \frac{1}{S_{i+\frac{1}{2}} - S_{i-\frac{1}{2}}} \qquad [(1-\theta)\,(r_i^{\,n})^2$$

$$\times \quad q_{i+\frac{1}{2}}^{n+\frac{1}{2}} \quad \frac{V_{i+\frac{1}{2}}}{V^n_{i+\frac{1}{2}}} \quad - \quad q^{n+\frac{1}{2}}_{i-\frac{1}{2}} \quad \frac{V_{i-\frac{1}{2}}}{V^n_{i-\frac{1}{2}}}$$

$$+ \ \theta\, r_i^{\,2} \left(q^{n+\frac{1}{2}}_{i+\frac{1}{2}} - q^{n+\frac{1}{2}}_{i-\frac{1}{2}} \right)] \qquad \text{(II-9)}$$

where $F_i = \frac{4\pi}{M_o} \quad \frac{r_i^{\,2}}{Q_i} \qquad \frac{P_{i+\frac{1}{2}} - P_{i-\frac{1}{2}}}{S_{i+\frac{1}{2}} - S_{i-\frac{1}{2}}} \quad - \quad \frac{Gm_i}{r_i^{\,2}}$,

$$S_{i+\frac{1}{2}} = \ln\,(Q_i\ Q_{i+1})\ ;$$

$$\frac{E_{i-\frac{1}{2}} - E^n_{i-\frac{1}{2}}}{\Delta t^{n+\frac{1}{2}}} = (1-\theta)\ G^n_{i-\frac{1}{2}} \qquad + \theta\ G_{i-\frac{1}{2}}$$

$$-\ q^{n+\frac{1}{2}}_{n-\frac{1}{2}} \quad V_{i-\frac{1}{2}} \quad \frac{W_{i-\frac{1}{2}} - W^{n}_{i+\frac{1}{2}}}{\Delta\ t^{n+\frac{1}{2}}} \quad , \qquad \text{(II-10)}$$

where $G_{i-\frac{1}{2}} = \frac{L_\odot}{M_o\ Q_{i-\frac{1}{2}}} \qquad \frac{B_i - B_{i-1}}{S_i - S_{i-1}}$

$$-\ P_{i-\frac{1}{2}}\, V_{i-\frac{1}{2}} \quad \frac{W_{i-\frac{1}{2}} - W^n_{i-\frac{1}{2}}}{\Delta\ t^{n+\frac{1}{2}}} \quad ,$$

$$W_{i-\frac{1}{2}} = \ln V_{i-\frac{1}{2}},$$

and
$$q^{n+\frac{1}{2}}_{i-\frac{1}{2}} = \begin{cases} 0 & \text{if } W_{i-\frac{1}{2}} \geq W^{n}_{i-\frac{1}{2}} \\ \dfrac{q_o\,(r_i - r_{i-1})^2\,(W_{i-\frac{1}{2}} - W^{n}_{i-\frac{1}{2}})^2}{V_{i-\frac{1}{2}}\,(\Delta t^{n+\frac{1}{2}})^2} & \text{if } W_{i-\frac{1}{2}} < W^{n}_{i-\frac{1}{2}} \end{cases}$$

q_o is discussed below;

$$B_i = \frac{256\,\sigma\,\pi^2}{3L_{\odot}M_o}\;\frac{r_i^{4}\,T_i^{4}}{\kappa_i}\;\frac{Z_{i+\frac{1}{2}} - Z_{i-\frac{1}{2}}}{S_{i+\frac{1}{2}} - S_{i-\frac{1}{2}}}\;; \qquad \text{(II-11)}$$

$$\frac{R_i - R_i^{n}}{\Delta t^{n+\frac{1}{2}}} = (1-\theta)\,\frac{v_i^{n}}{r_i^{n}} + \theta\,\frac{v_i}{r_i}\,. \qquad \text{(II-12)}$$

All quantities without a time superscript represent values at time t^{n+1}.

The parameter θ allows the expression of the time derivatives as a mixture of forward and backward differences. If $\theta = 1$, the equations are implicit; if $\theta = 0$, the equations are explicit. Using $\theta > 0$ relaxes the restriction put on the time step by the Courant condition. $\theta = 1$ was used to generate the stable model since the time step could become arbitrarily large as the model approached equilibrium. Using $\theta < 0.5$ in equations (II-8) to (II-12) produces numerical instabilities as shown by Kutter and Sparks (1972).

The boundary conditions at the base of the envelope are

$$v_1 = 0,\; B_1 = L_0/L_{\odot},\; r_1 = r_0 \qquad \text{(II-13)}$$

At the surface they are

$$F_{N+1} = -\frac{4\pi}{M_o}\,\frac{r_{N+1}^{2}\,(P_o - P_{N+\frac{1}{2}})}{Q_{N+1} - Q_{N+\frac{1}{2}}} - \frac{GM_o}{r_{N+1}^{2}} \qquad \text{(II-14)}$$

and

$$B_{N+1} = \frac{16\,\pi\sigma}{3\,L_\odot} \quad r^2_{N+1} \quad T^4_{N+\frac{1}{2}}$$

$$\times \left[\frac{2}{3} - \frac{M_o}{4\,\pi} \; \frac{\kappa_{N+\frac{1}{2}}\,(Q_{N+1} - Q_{N+\frac{1}{2}})}{2\,(r^3_{N+1} \cdot r_N)^{\frac{1}{2}}} \right]. \tag{II-15}$$

The constitutive equations are

$$P = b'T/V + P_r = \text{gas + radiation pressure} \tag{II-16}$$

$$E = \frac{3}{2}b'T + E_r + E_{i+e} = \text{thermal + radiation} \tag{II-17}$$

$$+ \text{ ionization + excitation energy}$$

where b' and E_{i+e} as well as κ are tabulated as functions of T and V and depend on the composition. In the diffusion approximation the radiation pressure $P_r = \frac{1}{3}\,aT^4$, and the radiation energy density $E_r = aT^4$.

2. Solving the difference equations.

The first step in solving the difference equations is to linearize by replacing the set $\left| v_i,\ B_i,\ R_i,\ W_{i+\frac{1}{2}},\ Z_{i+\frac{1}{2}} \right|$ with the set $\left| v_i + \delta\,v_i,\ B_i + \delta\,B_i,\ R_i + \delta\,R_i,\ W_{i+\frac{1}{2}} + \delta\,W_{i+\frac{1}{2}},\ Z_{i+\frac{1}{2}} + \delta\,Z_{i+\frac{1}{2}} \right|$. For example r_i^2 is replaced by $r_i^2(1+2\delta\,R_i)$ and $P_{i+\frac{1}{2}}$ by

$$P_{i+\frac{1}{2}} \left[1 + \frac{\partial\Pi}{\partial N}\bigg|_{Z_{i+\frac{1}{2}}} \delta\,W_{i+\frac{1}{2}} + \frac{\partial\Pi}{\partial Z}\bigg|_{W_{i+\frac{1}{2}}} \delta\,Z_{i+\frac{1}{2}} \right] .$$

The increments are now treated as the unknowns of the system. This leads to a system of 5N algebraic equations in 5N + 5 unknowns which combined with the 5 boundary conditions, $\delta\,v_1 = \delta\,B_1 = \delta\,R_1 = \delta\,W_{N+3/2} = \delta\,Z_{N+3/2} = 0$, is a well-defined system of equations.

An initial guess to the model at time t^{n+1} is obtained by extrapolating from the preceding model. In general, the difference equations will not be satisfied by the extrapolated variables. Henyey, Forbes, and Gould (1964) have described a method for solving the linearized equations. The system of equations for interface 2 is set up using the determinant elements given in Appendix A, and a Gauss-Jordan reduction is performed to reduce this block to a nearly diagonal form. This procedure is continued until the block for interface N+1 has been reduced. A schematic of the partially reduced matrix is shown in figure II-1. Since only the inhomogeneous terms and those elements denoted "X" in the figure need be saved, less computer memory is required than with other methods.

After the matrix has been reduced to the form of Figure II-1, a back solution is performed to find the set of increments to be added to the first guess. After updating the variables, the above procedure is repeated until either the increments or the inhomogeneous terms are sufficiently small.

Although the convergence is nearly quadratic for these models, it can be accelerated. If the convergence is monotonic, the increments can be multiplied by a number $\Delta > 1$; if the convergence is oscillatory, $\Delta < 1$ can be used. In these calculations $\Delta = 0.9$ produced the most rapid convergence.

3. Opacity Averaging.

When interpolations are needed, geometric means are used, i.e., $T_i = (T_{i+\frac{1}{2}} \cdot T_{i-\frac{1}{2}})^{\frac{1}{2}}$. The opacity, though, requires special handling. In the hydrogen ionization region (HIR) the opacity differs by several orders of magnitude between neighboring zones. If the geometric mean is used to find the opacity at the interface between these two zones, large variations are observed in the light curve every time a zone moves through the HIR. According to Stobie (1969a) this effect is caused by using too large an opacity at the interface, resulting in the zone on the high opacity side of the HIR not radiating as efficiently as it should. The excess energy retained by this zone is released in a very short time when the zone cools and its opacity drops. This zoning effect can amount to $0^{m}_{.}2$ on the light curve.

To avoid this problem, the opacity at the interface is defined by

$$\kappa_i = \kappa_+^{b} \, \kappa_-^{1-b} \tag{II-18}$$

where κ_+ is the larger opacity, κ_- is the lower opacity, and $0 < b < 1$ is a free parameter. Tests were made to determine the best value for b. With $b \geq 0.5$, the light curve was very jagged. With $b < 0.2$, the pulsation amplitude decreased. A value of $b = \frac{1}{3}$ did not noticeably affect the pulsation amplitude and produced a light curve with bumps due to the zoning of less than $0^{m}_{.}05$. This value of b was used throughout.

4. Artificial viscosity pressure.

The artificial viscosity pressure is an arbitrary quantity used to limit the discontinuity at shock fronts (Richtmeyer and Morton 1967). If no aritifical viscosity is included, shock fronts become smaller than one zone, and the time steps taken by the model become very short. The artificial viscosity pressure smooths the shock front over several zones and thereby limits the discontinuity of the shock front.

Kutter and Sparks (1972) have shown that the artificial viscosity pressure does not contribute to the mechanical flux and, therefore, does not affect the conservation of energy.

Stobie (1969a) used a constant value of q_0 (see equation II-10) throughout the envelope and has shown that the pulsation amplitude of his models decreases as the value of q_0 increases. Shocks only appear in the outer zones, though, and no artificial viscosity is needed deeper than the HeII ionization region. A variable q_0 can be used to account for this fact, i.e.,

$$(q_0)_{i-\frac{1}{2}} = q_e \exp\left(-P^n_{i-\frac{1}{2}}/P_H\right),$$

where q_e is a free parameter of order unity, and P_H was chosen as the pressure in the HIR in the equilibrium model. Tests were run to determine the best value of q_e. With $q_e < 2$, shocks were large and the time step small; with $q_e > 8$, the pulsation amplitude decreased. A value $q_e = 4$ was used and resulted in reasonably large time steps without affecting the pulsation amplitude. In fact, the pulsation amplitude was nearly independent of q_e for $2 < q_e < 6$. Changing P_H also had little effect on the pulsation as long as q_0 was small in the HeII ionization region.

The properties of the models computed using the methods presented in this section will be discussed in Chapter III and compared to the radiative transfer models discussed below.

B. Radiative transfer models.

1. Assumptions.

The diffusion approximation (equation II-4) represents the radiation field very well if the gas is optically thick. In the atmosphere, however, the radiation field is not isotropic, and a more exact solution to the transfer equation must be used. In order to simplify the calculations, the following assumptions were made:

1. The atmosphere of the model is plane parallel. Böhm-Vitense (1972) has shown that the effects of spherical symmetry are important for yellow supergiants only if $M_{BOL} < -7$.
2. The gas is in local thermodynamic equilibrium (LTE). This assumption is difficult to justify for a gas as tenuous as that of a Cepheid atmosphere but the problem would be intractable without it. The results obtained by Bell and Rodgers (1967), Parsons (1971b), and Schmidt (1971a, b) using LTE indicate that the non-LTE effects are not large.
3. The radiation field can be characterized by one frequency group whose opacity is the Rosseland mean. This gray approximation has been shown by Bendt and Davis (1971) to differ only slightly from the multi-frequency group solution although it may lead to an underestimate of the radiation pressure.
4. Terms of order v/c in the transfer equation can be ignored. Since velocities in Cepheids are typically less than 60 km s^{-1}, these terms should be negligible.
5. Energy transport is by radiation only. Although Cepheids are cool, the density in the envelopes is so low that convection is inefficient. In any case, an adequate theory of time-dependent convection is not available.

With these assumptions, the transfer equation can be written as

$$\mu \frac{dI}{d\tau} = I - \sigma T^4/\pi \tag{II-19}$$

where $\mu = \cos\theta$,

and $d\tau = \kappa\, dm$.

The physical parameters needed to solve the hydrodynamic equations (II-1) to (II-5) are the radiation energy density, E_r, the luminosity, L, and the radiation pressure, P_r, which are given by

$$E_r = \frac{4\pi}{c}\int_{-1}^{1} I\, d\mu\ , \tag{II-20}$$

$$L = 16\pi^2 r^2 \int_{-1}^{1} I\,\mu\, d\mu\ , \tag{II-21}$$

$$P_r = \frac{4\pi}{c}\int_{-1}^{1} I\,\mu^2\, d\mu . \tag{II-22}$$

2. Method of solution.

Due to the anisotropy of the radiation field, the transfer equation cannot be directly included in the hydrodynamic equations without introducing a great deal of complexity. It is possible to avoid this complexity by noting that the Henyey method is a special case of Newton's method for solving systems of nonlinear equations. Newton's method can be expressed as

$$\underline{x}^{(k)} = \underline{x}^{(k-1)} - J^{-1}\underline{f}(\underline{x}), \tag{II-23}$$

where $\underline{x}$ is the vector of unknowns (note that $\underline{x}^{(k)} - \underline{x}^{(k-1)}$ is the set of increments discussed in Section II-A), $\underline{f}(\underline{x})$ is the vector of inhomogeneous terms of the linearized equations, and J is the Jacobian of $\underline{f}$ with respect to $\underline{x}$, i.e., $J_{ij} = \partial f_i/\partial x_j$, and the superscript k counts the number of iterations. The system of equations is considered solved when $||\underline{f}(\underline{x})|| < \epsilon$, where ϵ is the convergence criterion.

If the Jacobian is exact, Newton's method converges quadratically (Ortega 1972); if J is only approximate, Newton's method may still converge but the rate of convergence will be slower than quadratic. This fact suggests a method for including the transfer equation in a Henyey type code. If the code is currently using $\underline{x}^{(k)} = \underline{x}^{(k-1)} - J_D^{-1}\underline{f}_D(\underline{x})$, where D signifies that the diffusion approximation was used to compute the quantity, try $\underline{x}^{(k)} = \underline{x}^{(k-1)} - J_D^{-1}\underline{f}_R(\underline{x})$, where R denotes that the transfer equation was used. The convergence properties of this method are discussed below.

3. Convergence of the modified Henyey method.

Theorem: Given

1. $\underline{x}^{(k+1)} = \underline{x}^{(k)} - J_D^{-1}\underline{f}_R(\underline{x}^{(k)})$, $k=0,1,2, \ldots$ (II-24)
2. $R \equiv J_R - J_D$ where J_R is the Jacobian of $\underline{f}_R$ with respect to $\underline{x}$,
3. $\underline{f}_R(\underline{x}^{(\infty)}) = 0$.

Show that for all $\epsilon > 0$, their exists a $\delta > 0$ and an $N > 0$ such that for $||\ R\ || < \delta$, $||\underline{x}^{(k)} - \underline{x}^{(\infty)}|| < \epsilon$ for $k > N$. In other words show that $\underline{x}^{(k)} \rightarrow \underline{x}^{(\infty)}$ as $k \rightarrow \infty$.

Proof:

Equation (II-24) can be expressed as a Picard iteration, i.e.,

$$\underline{x}^{(k+1)} = \underline{g}(\underline{x}^{(k)}), \qquad \text{(II-25)}$$

where $\underline{g}(\underline{x}) = \underline{x} - J_D^{-1}\underline{f}_R(\underline{x})$. By Ostrowski's theorem (Ortega 1972) the series (II-25) converges to $\underline{x}^{(\infty)}$ if $\rho(J_g) < 1$ when J_g is evaluated at $\underline{x}^{(\infty)}$ and if $||\underline{x}^{(0)} - \underline{x}^{(\infty)}\ ||$ is sufficiently small. Here J_g is the Jacobian of $\underline{g}(\underline{x})$ and $\rho(J_g)$ is the spectral radius (i.e., the largest eigenvalue) of J_g. The j component of $\underline{g}$ is

$$g_j = x_j - \sum_k (J_D^{-1})_{jk} f_k .$$

Then

$$(J_g)_{jm} = \frac{\partial g_j}{\partial x_m} = \delta_{jm} - \sum_k (J_D^{-1})_{jk} \frac{\partial f_k}{\partial x_m} - \sum_k \frac{\partial}{\partial x_m}(J_D^{-1})_{jk} f_k.$$

But $\underline{f}(\underline{x}^{(\infty)}) = 0$, so at $\underline{x}^{(\infty)}$

$$\frac{\partial g_j}{\partial x_m}\Big|_{\underline{x}^{(\infty)}} = \delta_{jm} - \sum_k (J_D^{-1})_{jk}(J_R)_{km}.$$

Therefore $J_g = I - J_D^{-1}J_R = I - J_D^{-1}(J_D + R) = -J_D^{-1}R$,

and $\rho(J_g) = \rho(J_D^{-1}R) \leq ||\ J_D^{-1} R\ || \leq ||\ J_D^{-1}\ || \cdot ||\ R\ ||$.

Choosing $\delta = ||\ J_D^{-1}\ ||^{-1}$ implies that $\rho(J_g) \leq ||\ R\ || / \delta < 1$ if and only if $||R|| \cdot ||J_D^{-1}|| < 1$.

The iteration, therefore, converges if $||R|| < ||J_D^{-1}||^{-1}$.

Q. E. D.

This method is analogous to using the secant method as an approximation to the Newton-Raphson iteration in the one dimensional case. Ortega (1972) has shown that the rate of convergence depends on the value of $\rho(J_g)$. If $\rho(J_g) = 0$, the convergence is quadratic. If $\rho(J_g) > 0$, as it is when R is non-zero, the convergence will be slower than quadratic. Since the matrix R is not known, it is not possible to verify a priori whether the iteration will converge to the desired solution. Ortega (1972) has shown that, if the procedure converges for $||\ \underline{x}^{(0)} - \underline{x}^{(\infty)}\ ||$ sufficiently small, it has converged to the correct solution. Unfortunately, it is impossible to define how small is sufficiently small. The radius of convergence can be found only by trial and error. In this code, the first guess is kept within the radius of convergence by limiting the time step.

4. Tests of the modified Henyey method.

As a check on this method, a model computed using gray, plane-parallel radiative transfer was allowed to evolve to hydrostatic equilibrium.

In the optically thick zones, the difference between the temperatures in the diffusion approximation and radiative transfer models was about 0.02%. In the optically thin zones, the model had a $T(\tau)$ that agreed with the exact solution of the gray transfer problem to better than 0.5%. A shock wave was then sent through the atmosphere. In the optically thin zones, a temperature inversion was observed at the shock front. No such temperature inversion was observed when the diffusion approximation was used.

Using J_D without modification produced very slow convergence. In the diffusion approximation the radiation field at a given point depends only on the local state of the gas. When using the transfer equation, however, the local radiation field depends on the state of the gas throughout the model. In a very optically thin zone, the radiation field is nearly independent of the local state of the gas. To account for this fact, J_D was modified by multiplying such terms as $\partial B/\partial T$ by $(1 - e^{-\tau})$. When these modifications were made to J_D, the rate of convergence improved without affecting the final results. The coefficients of the increments used for these models are given in Appendix B.

Using this method with gray, plane parallel radiative transfer takes about 30 minutes on the IBM 360/91 to compute one period of a Cepheid with a period of 12 days. About 25% of this time is used to solve the transfer equation. It would, therefore, take 8 additional minutes per frequency point for the non-gray problem, roughly a factor of four faster than the method of Keller and Mutschlecner (1970) and comparable in speed to the variable Eddington approximation used by Bendt and Davis (1971).

This method can be easily modified to include such effects as spherical symmetry or non-gray radiative transfer by replacing the transfer subroutine used here. In fact, the method has wider applicability. For example, a Henyey type evolution code could be modified to include deviations from hydrostatic equilibrium or convective overshoot.

This modified Henyey method has been used to compute deep envelope models of a 12^d classical Cepheid. The following chapters contain a discussion of the properties of these models.

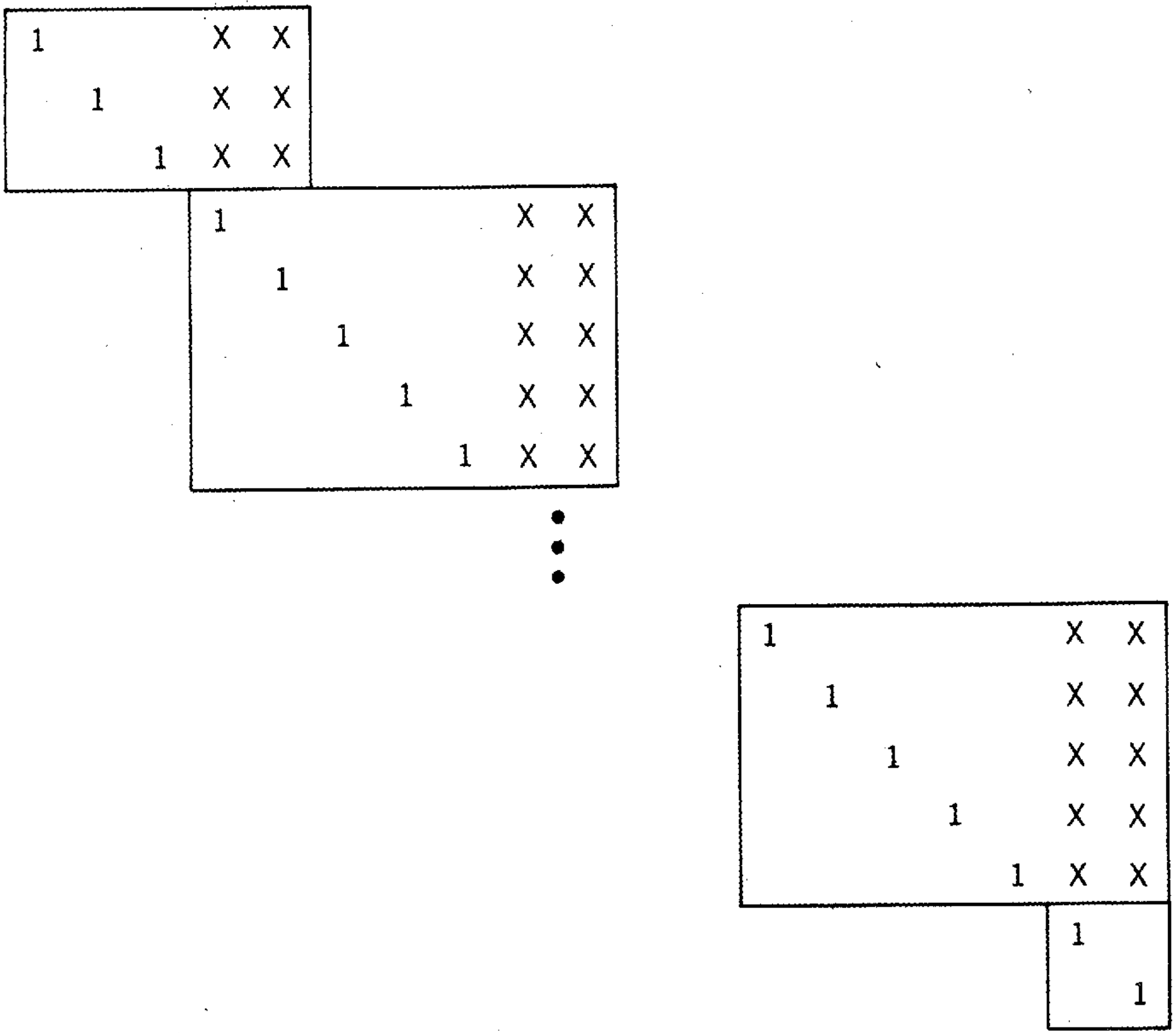

Figure II-1. Schematic of the partially reduced matrix of the coefficients. The x's denote non-zero matrix elements. All elements not shown are zero.

CHAPTER III

ENVELOPE OF THE MODEL

A. Equilibrium model.

1. Selection of the model.

There are two important criteria used to select a model for a study such as this. First, the model should represent a well-observed star to allow a comparison of theory with observation. Since there are bright Cepheids of many periods, this criterion does not greatly restrict the selection of model parameters. Second, the model should not present unnecessary computational problems. Stobie (1969c) has shown that short period Cepheids are more likely to be pulsating in a harmonic than in the fundamental mode and some may be pulsating in two modes simultaneously. Long period Cepheids also present problems. These stars are cool enough that convection is expected to be important. In addition, there is evidence of strong shocks in their atmospheres (Rodgers and Bell 1968; Dawe 1969).

These two criteria indicate that the model should be chosen to have a period between 8^d and 15^d. One further criterion is the availability of other theoretical results. Both Keller and Mutschlecner (1970, 1971) and Bendt and Davis (1971) computed models with periods of about 12^d. For these reasons a model with a period of 12^d was selected having T_{eff}=5700°K, $L=5000L_\odot$, and $M=5M_\odot$(Stobie 1969c).

2. The First Guess

Once the model has been selected, the first guess to the model at t=0 must be generated. Although experience has shown that the radius of convergence of the Henyey method is large, a reasonably accurate first guess to the initial model is needed. Simply taking a published envelope model will not suffice since difference in zoning, opacity, and mean molecular weight will cause problems. Either the iteration for the first time step will not converge or the model will develop such strong shocks that it will eject a large fraction of its mass. To avoid these problems the static envelope code used by Rose and Smith (1970, 1972) was modified to include the King IVa tables for opacity and mean molecular weight (King 1972). Table III-1 contains the number fractions of the elements included in calculating these tables.

After a static envelope having the desired mass, luminosity, and effective temperature was generated, the zoning criteria were selected. The total mass of the envelope was chosen so that the base of the envelope had $T=10^6$ °K since Stobie (1969a) has shown that including deeper zones does not appreciably affect the pulsation properties of the model. In order to have enough optically thin zones to study the atmosphere, a mass for the first zone of 1.5×10^{26} gm was selected. It is also necessary to have enough zones in the model to perform the numerical integration over depth with sufficient accuracy. The results of Stobie (1969a) and Bendt and Davis (1971) indicate that at least 50 zones are required. In order to minimize any problems associated with the zoning, 100 zones were used. This combination of 100 zones, mass of the surface zone of 1.5×10^{26} gm, and mass of the envelope of 0.5 $M_\odot$ resulted in a ratio of the mass of neighboring zones of 1.15. Once these parameters were selected, it was possible to interpolate in the static envelope model to obtain a first guess to the model at t=0.

3. Relaxation to equilibrium.

The first guess to the model at t=0 was used as input to the hydrodynamic code. Since the static envelope code included convection and the hydrodynamic code did not, the model was not quite in hydrostatic or thermal equilibrium. In order to decrease the computer time required for the model to evolve to equilibrium, the pulsation was artificially damped by converting some of the kinetic energy into thermal energy at each time step. With this damping the model reached equilibrium in about 4000 time steps.

The equilibrium model was found to have a slightly different effective temperature than the static envelope model. Some adjustment was, therefore, necessary. The two free parameters that determine the position of the model in the H-R diagram are the luminosity incident on the lower boundary, L_0, and the radius of the lower boundary, r_0. In equilibrium the luminosity leaving the surface must be equal to L_0. Thus, if L_0 is the luminosity selected for the static model, the effective temperature of the model can be changed by varying r_0. If r_0 is decreased, the model becomes more compressed, and T_{eff} increases; if r_0 is increased, T_{eff} decreases. After changing r_0 the model must be forced to return to equilibrium. This procedure of changing r_0 and forcing the model to return to equilibrium was continued until the model had the desired effective temperature.

The final equilibrium model, STB, has L=5000 $L_\odot$, M=5$M_\odot$, T_{eff} = 5730°K, and R_*=71.7 $R_\odot$. STB has 25 optically thin zones ranging from $\tau = 4.6 \times 10^{-4}$ to $\tau = 3$. Due to the large opacity in the hydrogen ionization region, the first optically thick zone is at $\tau = 580$. It is possible, therefore, to refer to the optically thin zones as the atmosphere without ambiguity. Since the atmosphere of STB has a thickness of only 1% of the radius of the model, the plane parallel assumption used in the radiative transfer calculations is justified.

Table III-2 contains the parameters of the final equilibrium envelope, and figures III-1 to III-3 show the logarithm of the temperature, pressure, and density, respectively, versus the logarithm of Lagrangian mass coordinate. Note the large temperature increase and the density inversion in the hydrogen ionization region. Both of these effects would be smaller, but not eliminated, if convection were included in the model (Latour 1970; Eoll 1973). However, the time it takes a convective element to travel one mixing length is comparable to the period of the Cepheid. Convection cannot be included correctly in the hydrodynamic models until a theory of time dependent convection is developed.

B. Full amplitude model.

1. Growth to full amplitude.

Once a static envelope with the desired luminosity and effective temperature has been generated, the pulsation can be initiated in one of two ways, by soft self-excitation or by hard self-excitation (Ledoux and Walraven 1958). The former approach allows the pulsation to grow from the computer round-off "noise" (Cox and Giuli 1968, pg 1125). The soft self-excitation requires no prior knowledge of the pulsation mode or the full amplitude velocity distribution, but the model must be followed for 5 to 10 e-folding times. The second approach has been used by Christy (1968) and Stobie (1969a) and consists of imposing a finite amplitude velocity distribution on the static model. The initial velocity field is usually chosen so that the initial kinetic energy amplitude is about 25% of its full amplitude value. If the imposed velocity distribution does not correspond to nearly a pure mode, transients will have a large amplitude and will take several e-folding times to die out. This method assumes a substantial amount of information about the full amplitude pulsation, but it allows full amplitude to be reached in only 2 or 3 e-folding times. Since Stobie (1969a) gives the initial velocity distribution for a wide variety of Cepheid models, and because e-folding times of Cepheids are of the order of 100 periods, the hard self-excitation approach was used.

Since the radiative transfer models take about five times more computing time per period than the diffusion approximation models, the diffusion approximation was used in generating the full amplitude model. The initial velocity distribution was given by

$$v = -v_0(r / r_p)^6,$$

where r_p = radius at $\tau = 1$,

and $v_0 = 10 \text{ km s}^{-1}$.

The maximum of the total kinetic energy in the envelope during a period, KE_{max}, provides the most reliable measure of the growth of the pulsation. After initiating the pulsation, it was found that KE_{max} decreased for two periods as the high order harmonics introduced by the initial velocity distribution died out. After about 8 periods these transients had a much lower amplitude than the fundamental mode.

In order to speed the growth to full amplitude, an artificial amplification was used (Stobie 1969a). Choosing a phase when all zones were moving outward with nearly their maximum velocity, the velocity in each zone was multiplied by 1.5, doubling the kinetic energy. Although this procedure introduced some transients, they quickly died out. At period 26 the method of opacity averaging at the HIR was changed to the method described in Chapter II. This change greatly reduced the zoning effects resulting in fewer shocks and, therefore, less damping due to the artificial viscosity. The rate of increase of KE_{max} then increased. The model was then allowed to pulsate for another 120 periods, about 3 e-folding times (Stobie 1969c). At this point KE_{max} was increasing by only 0.02% per period. Period 150 was chosen as the full amplitude, diffusion approximation model, IHC (for implicit hydrodynamic code). Figure III-4 shows the approach of KE_{max} to full amplitude.

IHC was used as the starting model for the radiative transfer calculation. As can be seen in figure III-4, KE_{max} decreased smoothly (indicating few transients) and approached a value about 10% lower than KE_{max} in IHC. After 30 more periods KE_{max} was decreasing by less than 0.1% per period. Period 180 was chosen as the full amplitude radiative transfer model, RDT. The smaller amplitude of RDT relative to IHC is due to changes in the structure of, and, therefore, the work done by, zones passing through the HIR. The ratio of $\int PdV$ in RDT to $\int PdV$ in IHC for those zones passing through the HIR is 0.85

accounting for the lower amplitude of RDT.

2. Properties of the full amplitude models.

The period of RDT is $12\overset{d}{.}05$, which combined with the mass and radius of STB gives $Q = P\sqrt{\rho/\rho_\odot} = 0.046$. Christy (1968) has shown that $Q=0.022(R/R_\odot)^{\frac{3}{4}}(M_\odot/M)^{\frac{1}{2}}$. Using the radius and mass of STB gives Q = 0.043 in good agreement with RDT.

A comparison between the full amplitude RDT and IHC models shows that, aside from differences due to the lower amplitude of RDT, the two models produce nearly identical light and velocity curves confirming the results of Bendt and Davis (1971) and Davis (1971). The major difference between the models is that IHC never has temperature inversions in the atmosphere while RDT does whenever there are sufficiently strong shocks present.

It is not difficult to understand this difference between the models. Consider a stellar atmosphere in radiative equilibrium. In the diffusion approximation

$$L \sim \frac{dB}{d\tau} = \frac{B_{i+1} - B_i}{\tau_{i+1} - \tau_i} \quad .$$

If the temperature in zone i+1 is increased, the luminosity will increase by an amount

$$\Delta L \sim \frac{\Delta B_{i+1}}{\tau_{i+1} - \tau_i}$$

If $\tau_{i+1} - \tau_i$ is small, as it is in the atmosphere, ΔL will be large. The excess thermal energy in zone i+1 will be radiated away and the atmosphere will rapidly return to equilibrium. On the other hand, the luminosity given by the transfer equation is

$$L \sim \int_{\tau_i}^{\infty} B(t)E_2(t-\tau)dt - \int_0^{\tau_i} B(t)E_2(\tau_i-t)dt,$$

where E_2 is the second exponential integral. Perturbing the temperature in zone i+1 results in

$$\Delta L \sim \Delta B_{i+1} \int_{\tau_i}^{\tau_{i+1}} E_2(t-\tau_i)dt.$$

If $\tau_{i+1} - \tau_i$ is small,

$$\Delta L \sim \Delta B_{i+1} \qquad (\tau_{i+1}-\tau_i).$$

In the atmosphere, then, ΔL will be small and the return to equilibrium will be slow. This behavior of the radiative transfer solution has been discussed by Whitney (1967).

Since the temperature inversions in RDT occur only above τ=0.01, they will be important only for spectral lines and will have only a small effect on the continuum. In fact, the continuum forming regions of the atmosphere are nearly in radiative equilibrium at nearly all phases as predicted by Whitney (1967). In the following discussion all values will be taken from RDT, but the conclusions reached apply equally well to IHC.

The relative radius change

$$\frac{\Delta R}{R} = \frac{R_{MAX} - R_{MIN}}{R_{MEAN}} = 0.11$$

is in good agreement with observed values (Nikolov and Tsvetkov 1972), as is the velocity amplitude $v_{max}-v_{min}$ = 45 km sec^{-1} (Stibbs 1955). Figure III-5 shows the bolometric light curve. The small ripples on the light curve are due to the zoning effects discussed in the preceding chapter and are small enough not to confuse the interpretation of the main features. The asymmetry of the light curve falls within the observed range (Nikolov 1968). In contrast, the models of Keller and Mutchlecner (1970, 1971) and Bendt and Davis (1971) are too asymmetric in the sense that the rising branches of their light curves are too steep. Since they use a shallow envelope driven from below by a coarsely zoned deep envelope model, and RDT was computed using fine zoning throughout, this difference is probably due to zoning.

Aside from the overall variation of the light curve and the zoning effects, there are three features of interest, a sudden decrease in light output at phase $\Phi = 0.15$, a shoulder on the rising branch near $\Phi = 0.2$, and a bump on the falling branch near $\Phi = 0.6$. All three features show zoning effects superimposed on them and, therefore, are probably not due to the zoning. The shoulder on the rising branch and the bump on the falling branch will be discussed in the next section but it should be noted that Cepheids with periods near 10^d often show similar features (van Genderen 1970).

The dip at $\Phi = 0.15$ is disturbing since it is not observed (Nikolov 1968). Bendt and Davis (1971) also see a similar feature on their light curves as do King, Cox, Eilers, and Davey (1973) in their coarsely zoned diffusion approximation model of an $11\overset{d}{.}5$ Cepheid. Since this feature is usually dismissed as a zoning effect, an attempt was made to find its cause. A detailed search of the computer output revealed nothing related to the zoning that could cause the dip. Hillendahl (1968) attributes the feature to the artificial viscosity. There is a pressure wave moving outward that produces the shoulder at $\Phi = 0.2$. The artificial viscosity causes the pressure to rise ahead of the temperature. The pressure rise causes the density to increase which, in turn, raises the opacity. When this region of increased opacity reaches τ=1, the amount of light emitted decreases. An opacity increase of 3% is sufficient to produce the dip observed on the theoretical light curve. The same mechanism will produce a dip preceding the bump at Φ = 0.6. The bump on the falling branch would look more like a shoulder if the artificial viscosity could be removed.

Figure III-6 shows the velocity corresponding to τ = 0.2. The shoulder on the rising branch cannot be seen, but the bump on the falling branch is quite pronounced. Since the velocity curves are usually used to classify the bumps in the models, this model would be described as having a single bump on the falling branch. According to the Hertzsprung sequence a Cepheid with a period of 12^d should have a bump on the rising branch. If the velocity curve was used to classify this model, it would be concluded that the model had the wrong mass. This problem of classifying bumps on the light curves can contribute to the Cepheid mass discrepancy (see Chapter I).

Figure III-7 shows the velocity curves for τ = 10^{-3}, 10^{-1}, 1 and for a mass zone having τ = 0.2 in STB. The feature on the rising branch appears only for the most optically thin zones and may be responsible for the peculiarities in the cores of the Ca II H and K lines observed at this phase (Kraft 1967). The progressive nature of the wave travelling through the atmosphere is readily apparent. Substantial velocity gradients are present in the atmosphere from Φ = 0.3 to Φ = 0.7. The velocity curve following a given mass element is the same as that for τ = 1 except in the vicinity of the second bump even though τ = 1 moves through more than 10 mass zones. This point will be considered further in Chapter VI.

3. Phase lag.

The phase lag between the light and velocity curves, $\Delta \Phi$, depends on which velocity curve is used. The phase shift ranges from $\Delta \Phi = 0.06$ for $\tau = 1$ to $\Delta \Phi = 0$ for $\tau = 10^{-3}$. Linear, adiabatic theory predicts that light maximum should occur at minimum radius, not near equilibrium radius as observed. Explanations for the phase lag range from Eddington's suggestion in 1917 that the phase lag is a natural consequence of the processes limiting the amplitude of the star to Christy's in 1968 which attributes the phase lag to a skewing of the light curve due to non-linear effects. Since the linear calculations of King, Cox, Eilers, and Davey (1973) show the phase lag, it is probable that the lag is the result of non-adiabatic, not non-linear effects.

Castor (1968) treating the HIR as a discontinuity, has suggested that a theory proposed by Eddington (1926) is correct. The large heat capacity of the HIR delays light maximum. Since the HIR lies at the top of the transition region between the quasi-adiabatic envelope and the non-adiabatic atmosphere, the luminosity gets "frozen-in" at the top of the HIR.

The phase lag can be seen in Figure III-8 which is a 3-D plot showing the variation of luminosity, L/L_{STB}, as a function of mass point and phase as viewed from the center of the star. Note that phase increases from right to left. The inset is a schematic representation and will be used to define points of reference in the figure. Point A is in the He II ionization zone. This part of the model is nearly adiabatic, and, as expected, the luminosity maximum coincides with radius minimum. By the time the He I ionization zone is reached at point B, there is a substantial phase shift. A further, small phase shift is introduced in the HIR, the region between B and C. The "freezing-in" of the flux in the atmosphere, point C, is seen as luminosity perturbations moving outward at constant phase.

Plate I is a different representation of the same data and shows two periods of the motion. The abscissa is the time coordinate, the ordinate is the Lagrangian radial coordinate. Large values of L/L_{STB} appear as bright areas while small values appear dark. The base of the envelope is at the top of the figure. The bright area nearest the top of the figure corresponds to point A in figure III-8. As can be seen the phase of light maximum increases continuously until the atmosphere is reached. At this point the flux becomes "frozen-in" and the maximum moves outward at constant phase. The model, therefore, suggests that the HIR plays only a small role in generating the phase shift. The phase shift appears to vary continuously through the transition region between the quasiadiabatic envelope and the non-adiabatic atmosphere.

Plate I shows another interesting phenomenon. In the He II ionization region light minimum follows light maximum by about half the period. In the He I ionization zone this phase difference is still nearly half the period. Only in the atmosphere is the light curve very asymmetric. The asymmetry of the light curve is, therefore, either an atmospheric phenomenon or due to the HIR. This effect will be discussed in the next section.

C. Cause of the second bumps.

1. Christy mechanism.

In 1926, Hertzsprung classified Cepheids by the shape of their light curves (Payne-Gaposhkin 1951). Short period Cepheids have very asymmetric, smooth light curves. As the period increases the curves become more symmetric and a second bump appears on the falling branch in Cepheids with a period near 7^d. This bump moves closer to the primary maximum until at 10^d the bump appears to coincide with maximum light. Near a period of 12^d the light curves often show two shoulders, one on the rising and one on the falling branch. Cepheids with longer periods show a single bump on the rising branch. Near a 15^d period the curves again become smooth and asymmetric. Figure III-9 taken from Payne-Gaposhkin (1951) illustrates this sequence.

Christy (1970) using the results of his nonlinear calculations explains the second bump in the following manner. Near the phase of maximum compression the He II ionization zone is rapidly heating causing the zone to expand. This expansion sends a pressure wave outward which appears at light maximum. The expansion also sends a pressure wave inward which is reflected by the core and appears at the surface during the next cycle as a second bump. He then finds that the time delay, D (in days), can be used to find the radius of the model from $R / R_\odot = 4.05D$. Since the period of the star depends on both its mass and radius, Christy can find both the mass and radius of a star from its period and the phase of its bump. In general, masses found in this way are about half those predicted by stellar evolution theory.

It should be noted, however, that the Hertzsprung sequence is an average property of Cepheids. Van Genderen (1970) has shown that the phase of the second bump of individual Cepheids having the same period varies over a wide range. He also shows that, while the Hertzsprung sequence holds on the average up to a period of 10^d, there is almost no correlation between bump phase and period from 10^d to 30^d. Beyond 30^d the bump appears near minimum light. In those Cepheids having two bumps on their light curves, he suggests that two independent phenomena are operating.

2. Hillendahl's mechanism.

The mechanism proposed by Christy explains part of the Hertzsprung sequence. It does not, however, explain the double bump Cepheids. Another mechanism is needed. Figure III-10 shows the velocity as a function of mass point and phase. The inset will be used to define points of interest in the figure. Effects due to the zoning have been labelled "z" and are quite small compared to the main features. The shaded area in the inset shows the bottom side of the surface while the dashed line follows the HIR. The point corresponding to maximum light is labelled "A"; B is the shoulder on the rising branch of the light curve, and C is the bump on the falling branch. The line marked D is an inward moving pressure wave discussed below, and line E indicates the location of the inward moving pressure wave described by Christy (1970).

Figure III-11 is a different view of the same data. After reaching maximum expansion velocity near D the atmosphere begins to slow down under the influence of gravity along line E. However, a disturbance originating at point A changes the sign of the acceleration and propogates both outward toward B and inward toward C. The velocity reaches a second maximum near F and then decreases under the influence of gravity along G. The curve marked H indicates the velocity curve deeper in the envelope. Figure III-12 shows the origin of the inward and outward moving pressure waves. The line marked A is the locus of points of maximum velocity in the atmosphere; line B marks the locus of points of maximum velocity in the envelope. As is evident, the atmosphere reaches maximum velocity before the envelope and starts to slow down while the envelope is still accelerating compressing a region near the HIR. This compression generates pressure waves moving both outward (line AB on figure III-11) and inward (line AC on figure III-11). Line D(E) shows the inward (outward) moving pressure disturbance described by Christy (1970).

Figure III-13 clearly shows that the Christy pressure wave from the preceding cycle (line C) arrives at the surface of the model near light maximum (A), not near the second bump (B). In fact, this pressure wave reaches $\tau = 1$ very near $\Phi = 0.2$ and is responsible for the shoulder on the rising branch of the light curve.

Figure III-14 illustrates one possible explanation for the second bump proposed by Hillendahl (1969, 1970). The points A, B, and C correspond to the three local maxima on the light curve at phases $\Phi = 0.2$, 0.35, 0.6, respectively. The Christy pressure wave reaches the top of the envelope at point D and is responsible for the feature at B. According to Hillendahl, the local velocity minimum at E is the result of a rarefaction wave moving inward. The feature at C can then be attributed to a secondary, "blow-off" shock. The inward moving pressure disturbance (line C in figure III-12) is then a second rarefaction wave. In Hillendahl's interpretation, the features labelled z in figure III-10 are further blow-off shocks. This effect can also be seen in plate II. Here large positive velocities appear bright, zero velocity gray, and large negative velocities dark. Two periods are shown, i.e., phase increases from 0 to 2 from left to right, and the base of the envelope is at the top of the figure. The local velocity minimum preceding the second bump (line AB in figure III-11) can be followed backward in time into the envelope. Hillendahl considers this minimum to be a result of the rarefaction wave following the deep envelope pressure disturbance (line C in figure III-13). The inward moving pressure wave (line AC in figure III-11) he associates with a second rarefaction.

There are several problems with this interpretation. Hillendahl predicts as many as 5 blow-off shocks per period. All features on the light and velocity curves following the bump on the falling branch can be associated with zones moving through the HIR. While these zoning effects may be masking the secondary blow-off shocks, it is unlikely that the shocks would not be seen at all. Another difficulty is the inward moving pressure wave (AC in figure III-11). If this feature is to be associated with rarefaction following the secondary shock causing the bump, it should follow the local velocity maximum. It does not. It appears to originate before the second velocity maximum. The Christy mechanism cannot explain this feature either. Hillendahl's mechanism also predicts that all Cepheids should have a second bump on the falling branch since the primary expansion should always cause a secondary, blow-off shock.

3. Atmospheric oscillation mechanism.

Since neither Christy's nor Hillendahl's mechanisms adequately explain the Hertzsprung sequence a third mechanism was sought. Inspection of figure III-11 shows that the surface layers appear to be pulsating nearly sinusoidally from point J to point B with a period roughly 2/3 the period of the envelope. Figure III-15 shows the power spectra of two zones obtained from Fourier transforms of their velocity curves. The dashed line refers to a zone at the top of the envelope. No secondary periodicities are apparent with less than 3 times the frequency associated with the envelope period, ν_0. The amplitude of the feature near $\nu = 4\nu_0$ is so low that it may be due to noise generated in the transform process or to the inward moving pressure wave. The solid line, referring to an atmospheric zone, indicates a secondary periodicity near $2\nu_0$ with about 1/3 the amplitude of the main pulsation. The higher frequency features are probably the result of zoning effects or noise generated in the transform process.

The secondary periodicity can be understood in the following analysis which was used by Christy (1962) in an early attempt to predict the properties of Cepheid atmospheres. According to Lamb (1932) the critical period of an isothermal atmosphere is given by

$$P_a = 4\pi\, v_s/(\gamma g), \qquad \text{(III-1)}$$

where

$$v_s = \sqrt{\frac{2kT}{\mu m_H}},$$

$$\gamma = 5/3 \quad \text{for a neutral gas,}$$

$$g = \frac{GM}{R^2} = g_\odot \frac{M / M_\odot}{(R/R_\odot)^2}$$

Substituting values taken from STB shows that

$$P_a = 0\overset{d}{.}0025 \frac{(R/R_\odot)^2}{(M/M_\odot)} \qquad \text{(III-2)}$$

which gives $P_a = 2\overset{d}{.}5$ for STB. This period is too small to account for the secondary periodicity seen in the atmosphere of the model.

Gough, Ostriker, and Stobie (1965), on the other hand, have shown that a better approximation to the Cepheid atmosphere is an atmosphere with a constant temperature lapse rate. Choosing values from STB results in

$$P_a = 0\overset{d}{.}007 \quad \frac{(R\ /\ R_\odot)^2}{(M\ /\ M_\odot)} \quad , \qquad \text{(III-3)}$$

or $P_a = 7^d$ which is about 0.6 times the period of RDT. It appears that the bump on the light curve of RDT occurs because the atmospheric period, P_a, is comparable to, but less than, the envelope period, P_e.

The occurrence of two bumps on Cepheid light curves can be explained qualitatively as follows: Cepheids with periods less than 7^d have $P_a < 0.5\ P_e$. Since the atmosphere is being driven far from resonance, the amplitude of the atmospheric mode is low, and the atmosphere follows the motion of the envelope. Starting at 7^d, the driving frequency approaches the resonant frequency of the atmosphere, but not until about 10^d is the amplitude of the atmospheric mode large enough to produce an observable shock from the compression of the HIR. The multiple bumps seen on the rising branch of ultra-violet light curves of β Doradus by Hutchinson (1974) may indicate that the atmosphere is beginning to produce these shocks. In the period range 7^d to 10^d the bumps appearing on the falling branch are produced by the Christy mechanism. From 10^d to 12^d the Christy bump appears on the rising branch and the atmospheric oscillation bump appears on the falling branch. As the period increases beyond 12^d the amplitude of the atmospheric mode grows, but the compression of the HIR decreases as the atmosphere and envelope begin to oscillate in phase. There are no bumps from 15^d to 30^d since the compression of the HIR is too small to produce observable shocks. At about 25^d $P_a = P_e$, the atmosphere is oscillating at its maximum amplitude, but there are no bumps since the atmosphere and envelope are always in phase. Beyond 30^d bumps appear near minimum light as the envelope begins to slow down before the atmosphere leading to compression of the HIR near minimum light.

As shown by Payne-Gaposhkin (1951) Cepheids with periods near 10^d are anomalous compared to those at 8^d and 12^d. There is a dip in the velocity amplitude-period relation and in the upper envelope of the light amplitude-period relation near $P = 10^d$. The anomaly can be understood if primarily envelope oscillations are being observed up to 8^d, and atmospheric oscillations are being observed beyond 12^d.

4. Ratio of the atmosphere to the envelope period.

Further calculations will be needed to check the validity of the above picture, but it can be examined for consistency using published relations among L, P_e, R, and M. In the following discussion, R and M are given in solar units and periods in days. In logarithmic form, equation (III-3) becomes

$$\log P_a = -2.14 + 2 \log R - \log M \qquad \text{(III-4)}$$

while the relation $P_e\sqrt{\rho/\rho_\odot} = Q(M,R)$ results in

$$\log P_e = a + b \log R + c \log M. \qquad \text{(III-5)}$$

Combining the period-luminosity law and the mass-luminosity relation results in an equation of the form

$$\log M = d \log P_e + e, \qquad \text{(III-6)}$$

where the constants d and e depend on the choice of a mass-luminosity relation. The scatter introduced into (III-6) by multiple crossings of the instability strip will be small since 90% of the observed Cepheids are expected to be in the second crossing (Iben 1966). Similarly, Fernie (1968) has shown that a relationship of the form

$$\log R = f \log P_e + g \qquad \text{(III-7)}$$

can be expected. If equations (III-6) and (III-7) are to be consistent with (III-5)

$$a + bg + ce = 0, \qquad \text{(III-8)}$$

$$bf + cd = 1$$

The values of the constants in equations (III-5) to (III-7) can be found in the literature. Christy (1970) and Fricke, Stobie, and Strittmatter (1972) give essentially the same values for the constants in (III-5), namely

$$\log P_e = -1.62 + 1.72 \log R - 0.68 \log M. \qquad \text{(III-9)}$$

Using Stobie's (1969c) mass-luminosity law gives

$$\log M = 0.34 \log P_e + 0.33, \qquad \text{(III-10)}$$

where the constant, e, has been adjusted slightly to give the correct mass for RDT. Fernie (1968) has used the Wesselink method to find

$$\log R = 0.56 \log P_e + 1.24, \qquad \text{(III-11)}$$

where the zero point has been adjusted downward as suggested by Parsons (1972).

Equations (III-9) to (III-11) do not satisfy the consistency conditions (III-8). If the period-radius law, which was derived directly from observations, is redefined so the consistency conditions are satisfied

$$\log \bar{R} = 0.72 \log P_e + 1.07. \qquad \text{(III-12)}$$

The large change in the coefficients in the period-radius relation indicates that either the wrong mass-luminosity law was used, or there are systematic errors in the radii determined using the Wesselink method. The former possibility will be investigated below, and the latter in Chapter VI. Equation (III-12) agrees almost exactly with the relationship given by Wooley and Carter (1973) indicating an error in the Wesselink method as used by Fernie and Parsons.

The adopted relationships are

$$\log P_e = -1.62 + 1.72 \log R - 0.68 \log M, \qquad \text{(III-13)}$$

$$\log M = 0.34 \log P_e + 0.33, \qquad \text{(III-14)}$$

$$\log R = 0.72 \log P_e + 1.07 \qquad \text{(III-15)}$$

$$\log P_a = -2.14 + 2 \log R - \log M. \qquad \text{(III-16)}$$

Substituting equations (III-14) and (III-15) into (III-16) gives

$$\log P_a = 1.10 \log P_e - 0.33,$$

or

$$\log (P_a/P_e) = 0.10 \log P_e - 0.33 \qquad \text{(III-17)}$$

Equation (III-17) indicates $P_a = P_e$ near $\log P_e = 3$ which does not support the explanation of the double bump Cepheids give above.

Repeating this analysis using the results of stellar evolution theory as given by Iben and Tuggle (1972a) and again defining the period-radius law from the consistency conditions gives

$$\log P_e = -1.53 + 1.73 \log R - 0.79 \log M, \qquad \text{(III-18)}$$

$$\log M = 0.30 \log P_e + 0.56, \qquad \text{(III-19)}$$

$$\log R = 0.72 \log P_e + 1.14. \qquad \text{(III-20)}$$

Note that the period-radius law (III-20) is nearly the same as (III-15). The discrepancy with the observed relation (III-11) is, therefore, not due to the choice of a particular mass-luminosity law. Substituting (III-19) and (III-20) into (III-16) gives

$$\log (P_a/P_e) = 0.21 \log P_e - 0.30, \tag{III-21}$$

indicating $P_a = P_e$ near $P_e = 30^d$.

One of two conclusions can be reached from this analysis. Either the analysis of the atmospheric oscillations is in error, and the bump on the falling branch of the light curve has a different origin, or the mass-luminosity relation predicted by evolution theory is more nearly correct than that of pulsation theory. There is other evidence to support the evolution masses. If masses determined from the phase of the second bump are ignored, both Fricke, Stobie, and Strittmatter (1971, 1972) and Iben and Tuggle (1972, a,b) can explain the mass discrepancy. Since the pulsation masses depend critically on the calibration of the observations, reasonably small changes in the T_{eff} vs. (B-V) relation, the helium abundance, and the zero point of the period-luminosity law can remove the mass discrepancy. But, if there are two mechanisms which can produce bumps on the light curves, the bump masses should be ignored.

Although this discussion favors the evolution masses, the question cannot be settled without computing more models with many optically thin zones, a time consuming procedure. Additionally, more accurate values for the constants in equations (III-5) to (III-7) are needed. In particular, the variation of the pulsation constant, Q, with mass and radius is not well-known. The results of Cogan (1970), Cox, King, and Stellinwerf (1972) are considerably different from those of Christy (1970), Fricke, Stobie, and Strittmatter (1972), and Parsons and Bouw (1971). Further study including the effects of convection is needed.

TABLE III-1

NUMBER ABUNDANCES USED FOR KING IVa TABLES

X = 0.70 Y = 0.28 Z = 0.02

ELEMENT	ABUNDANCE
H	9.07156E-1
He	9.13793E-2
C	2.84443E-4
N	8.01673E-5
O	6.36793E-4
Ne	3.58809E-4
Na	1.42560E-6
Mg	1.79473E-5
Al	1.18576E-6
Si	2.27738E-5
Ar	2.38399E-5
Fe	3.69354E-5

TABLE III-2

EQUILIBRIUM MODEL

Zone	1 - Q	log T	log P	log ρ	log R	τ	κ
1	1.003(-1)	5.991	10.449	-3.705	11.9075	5.94(7)	8.53(-1)
2	8.724(-2)	5.950	10.267	-3.847	11.9453	4.70(7)	9.26(-1)
3	7.586(-2)	5.909	10.092	-3.983	11.9806	3.72(7)	9.60(-1)
4	6.597(-2)	5.870	9.924	-4.112	12.0138	2.96(7)	1.03
5	5.736(-2)	5.831	9.762	-4.236	12.0450	2.35(7)	1.07
6	4.988(-2)	5.793	9.606	-4.355	12.0742	1.86(7)	1.09
7	4.337(-2)	5.756	9.454	-4.470	12.1017	1.49(7)	1.10
8	3.772(-2)	5.721	9.306	-4.584	12.1277	1.20(7)	1.07
9	3.280(-2)	5.689	9.162	-4.698	12.1523	9.81(6)	1.06
10	2.852(-2)	5.658	9.022	-4.809	12.1758	8.12(6)	1.14
11	2.480(-2)	5.628	8.885	-4.917	12.1984	6.70(6)	1.19
12	2.156(-2)	5.598	8.752	-5.022	12.2200	5.54(6)	1.23
13	1.875(-2)	5.568	8.621	-5.125	12.2406	4.60(6)	1.30
14	1.631(-2)	5.539	8.493	-5.224	12.2604	3.80(6)	1.34
15	1.418(-2)	5.510	8.368	-5.322	12.2794	3.15(6)	1.35
16	1.233(-2)	5.483	8.245	-5.421	12.2975	2.63(6)	1.30
17	1.072(-2)	5.458	8.125	-5.519	12.3151	2.23(6)	1.33
18	9.323(-3)	5.434	8.006	-5.616	12.3320	1.89(6)	1.45
19	8.106(-3)	5.409	7.891	-5.709	12.3484	1.60(6)	1.56
20	7.049(-3)	5.383	7.777	-5.799	12.3643	1.35(6)	1.65
21	6.129(-3)	5.358	7.666	-5.887	12.3795	1.14(6)	1.71
22	5.330(-3)	5.333	7.557	-5.972	12.3941	9.55(5)	1.75
23	4.635(-3)	5.309	7.450	-6.056	12.4081	8.03(5)	1.79
24	4.030(-3)	5.285	7.345	-6.138	12.4216	6.77(5)	1.85
25	3.505(-3)	5.260	7.242	-6.218	12.4345	5.70(5)	1.91
26	3.048(-3)	5.236	7.141	-6.296	12.4468	4.79(5)	1.94
27	2.650(-3)	5.213	7.042	-6.373	12.4586	4.04(5)	1.96
28	2.304(-3)	5.190	6.945	-6.449	12.4700	3.41(5)	1.97
29	2.004(-3)	5.167	6.849	-6.523	12.4808	2.88(5)	2.00
30	1.742(-3)	5.145	6.754	-6.754	12.4913	2.44(5)	2.07
31	1.515(-3)	5.122	6.661	-6.667	12.5013	2.06(5)	2.14
32	1.318(-3)	5.100	6.570	-6.736	12.5108	1.74(5)	2.16
33	1.146(-3)	5.077	6.480	-6.804	12.5199	1.46(5)	2.17
34	9.964(-4)	5.055	6.391	-6.870	12.5287	1.23(5)	2.16
35	8.664(-4)	5.033	6.303	-6.936	12.5370	1.04(5)	2.14
36	7.353(-4)	5.012	6.216	-7.003	12.5450	8.85(4)	2.11
37	6.552(-4)	4.992	6.130	-7.068	12.5526	7.55(4)	2.12
38	5.697(-4)	4.971	6.046	-7.134	12.5600	6.44(4)	2.11
39	4.954(-4)	4.951	5.962	-7.199	12.5671	5.52(4)	2.10
40	4.308(-4)	4.932	5.878	-7.264	12.5739	4.74(4)	2.12
41	3.746(-4)	4.913	5.796	-7.329	12.5804	4.08(4)	2.11
42	3.257(-4)	4.895	5.715	-7.393	12.5868	3.53(4)	2.12
43	2.832(-4)	4.877	5.634	-7.458	12.5929	3.06(4)	2.13
44	2.463(-4)	4.859	5.554	-7.523	12.5989	2.66(4)	2.12
45	2.141(-4)	4.842	5.474	-7.588	12.6046	2.32(4)	2.17
46	1.862(-4)	4.825	5.396	-7.652	12.6102	2.03(4)	2.28
47	1.619(-4)	4.807	5.318	-7.714	12.6156	1.77(4)	2.36
48	1.408(-4)	4.790	5.241	-7.776	12.6209	1.54(4)	2.43
49	1.224(-4)	4.773	5.164	-7.837	12.6259	1.34(4)	2.48
50	1.064(-4)	4.755	5.089	-7.896	12.6308	1.17(4)	2.56

TABLE III-2 (continued)

Zone	1 - Q	log T	log P	log ρ	log R	τ	κ
51	9.253(-5)	4.738	5.014	-7.955	12.6356	1.01(4)	2.62
52	8.045(-5)	4.720	4.940	-8.012	12.6401	8.81(3)	2.69
53	6.995(-5)	4.702	4.866	-8.068	12.6445	7.65(3)	2.85
54	6.081(-5)	4.683	4.793	-8.120	12.6487	6.60(3)	2.98
55	5.287(-5)	4.663	4.721	-8.169	12.6527	5.67(3)	3.10
56	4.596(-5)	4.643	4.650	-8.216	12.6565	4.84(3)	3.18
57	3.995(-5)	4.622	4.580	-8.259	12.6601	4.11(3)	3.20
58	3.473(-5)	4.600	4.510	-8.299	12.6635	3.48(3)	3.15
59	3.018(-5)	4.578	4.440	-8.339	12.6666	2.95(3)	3.01
60	2.624(-5)	4.556	4.372	-8.380	12.6696	2.52(3)	2.83
61	2.280(-5)	4.536	4.303	-8.423	12.6723	2.17(3)	2.62
62	1.981(-5)	4.516	4.235	-8.468	12.6749	1.89(3)	2.45
63	1.722(-5)	4.498	4.168	-8.515	12.6773	1.67(3)	2.32
64	1.496(-5)	4.480	4.101	-8.563	12.6797	1.49(3)	2.30
65	1.299(-5)	4.462	4.034	-8.610	12.6819	1.33(3)	2.28
66	1.129(-5)	4.444	3.968	-8.657	12.6841	1.20(3)	2.25
67	9.800(-6)	4.425	3.903	-8.703	12.6861	1.09(3)	2.28
68	8.509(-6)	4.407	3.837	-8.747	12.6880	9.89(2)	2.31
69	7.386(-6)	4.388	3.773	-8.791	12.6899	9.03(2)	2.36
70	6.410(-6)	4.367	3.709	-8.831	12.6916	8.28(2)	2.45
71	5.561(-6)	4.345	3.645	-8.869	12.6933	7.60(2)	2.59
72	4.823(-6)	4.319	3.582	-8.900	12.6948	6.98(2)	2.85
73	4.181(-6)	4.287	3.519	-8.921	12.6963	6.39(2)	3.36
74	3.623(-6)	4.052	3.456	-8.629	12.6976	5.79(2)	3.74(1)
75	3.138(-6)	3.811	3.394	-8.223	12.6981	2.95	1.45(-1)
76	2.715(-6)	3.763	3.332	-8.236	12.6983	1.01	3.73(-2)
77	2.348(-6)	3.740	3.270	-8.275	12.6985	5.73(-1)	1.89(-2)
78	2.029(-6)	3.725	3.207	-8.323	12.6987	3.83(-1)	1.28(-2)
79	1.752(-6)	3.715	3.144	-8.375	12.6988	2.71(-1)	9.42(-3)
80	1.510(-6)	3.708	3.081	-8.431	12.6990	1.99(-1)	7.33(-3)
81	1.301(-6)	3.702	3.018	-8.489	12.6991	1.50(-1)	5.92(-3)
82	1.118(-6)	3.698	2.954	-8.549	12.6993	1.16(-1)	4.99(-3)
83	9.594(-7)	3.695	2.890	-8.610	12.6994	9.10(-2)	4.50(-3)
84	8.214(-7)	3.693	2.826	-8.672	12.6996	7.15(-2)	4.07(-3)
85	7.015(-7)	3.691	2.761	-8.735	12.6998	5.61(-2)	3.68(-3)
86	5.971(-7)	3.689	2.695	-8.799	12.6999	4.40(-2)	3.34(-3)
87	5.064(-7)	3.688	2.629	-8.864	12.7001	3.45(-2)	3.03(-3)
88	4.276(-7)	3.687	2.562	-8.930	12.7002	2.70(-2)	2.75(-3)
89	3.590(-7)	3.686	2.494	-8.998	12.7004	2.10(-2)	2.50(-3)
90	2.993(-7)	3.685	2.425	-9.066	12.7005	1.64(-2)	2.29(-3)
91	2.475(-7)	3.685	2.354	-9.137	12.7007	1.26(-2)	2.11(-3)
92	2.024(-7)	3.684	2.282	-9.209	12.7009	9.65(-3)	1.93(-3)
93	1.632(-7)	3.684	2.208	-9.284	12.7010	7.28(-3)	1.77(-3)
94	1.291(-7)	3.684	2.130	-9.361	12.7012	5.39(-3)	1.61(-3)
95	9.940(-8)	3.683	2.050	-9.443	12.7014	3.90(-3)	1.46(-3)
96	7.362(-8)	3.683	1.965	-9.529	12.7016	2.72(-3)	1.33(-3)
97	5.120(-8)	3.683	1.873	-9.622	12.7018	1.79(-3)	1.22(-3)
98	3.170(-8)	3.683	1.768	-9.729	12.7020	1.05(-3)	1.11(-3)
99	1.474(-8)	3.683	1.660	-9.840	12.7023	4.61(-4)	1.01(-3)

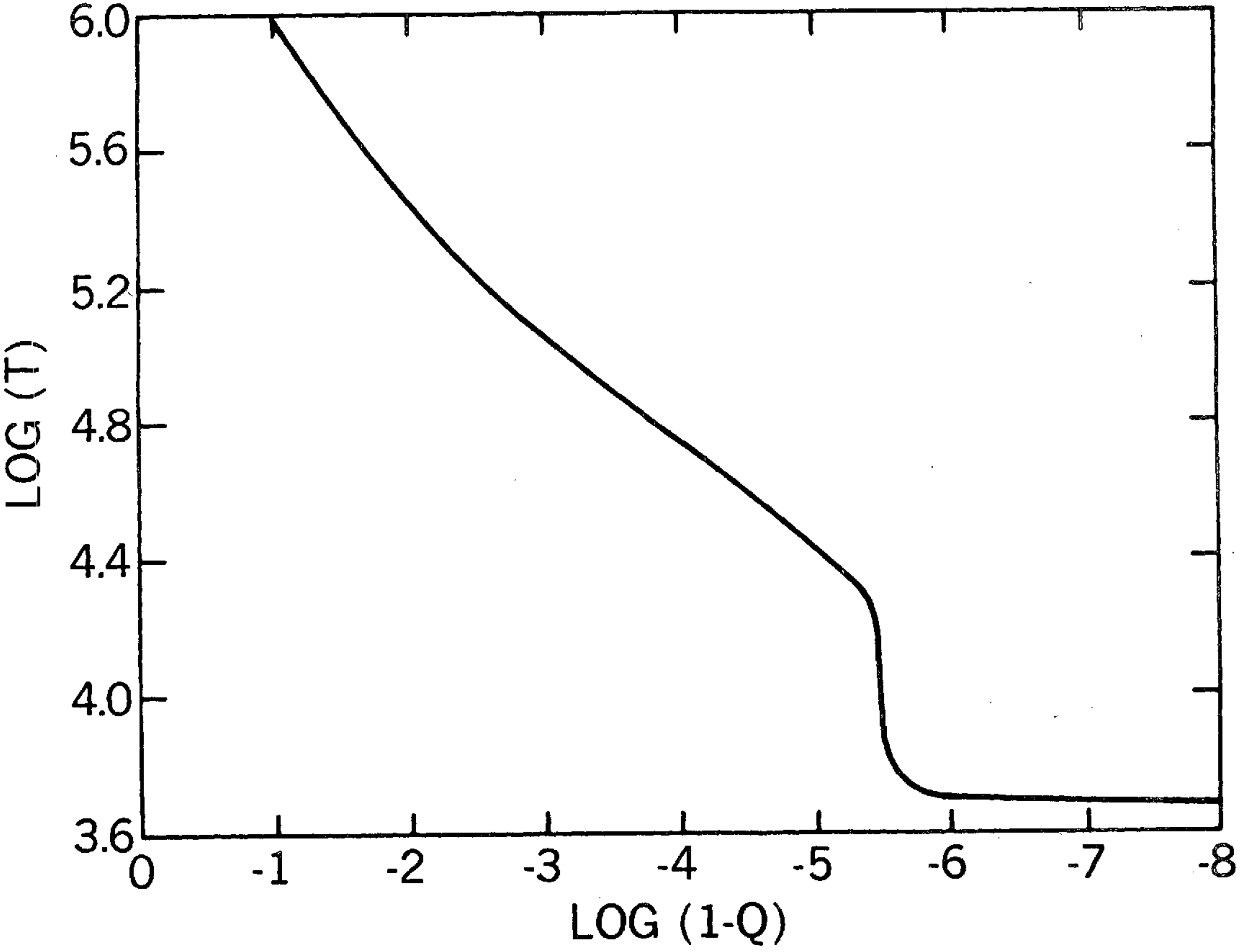

Figure III-1. log T vs. log (1-Q) in the equilibrium model

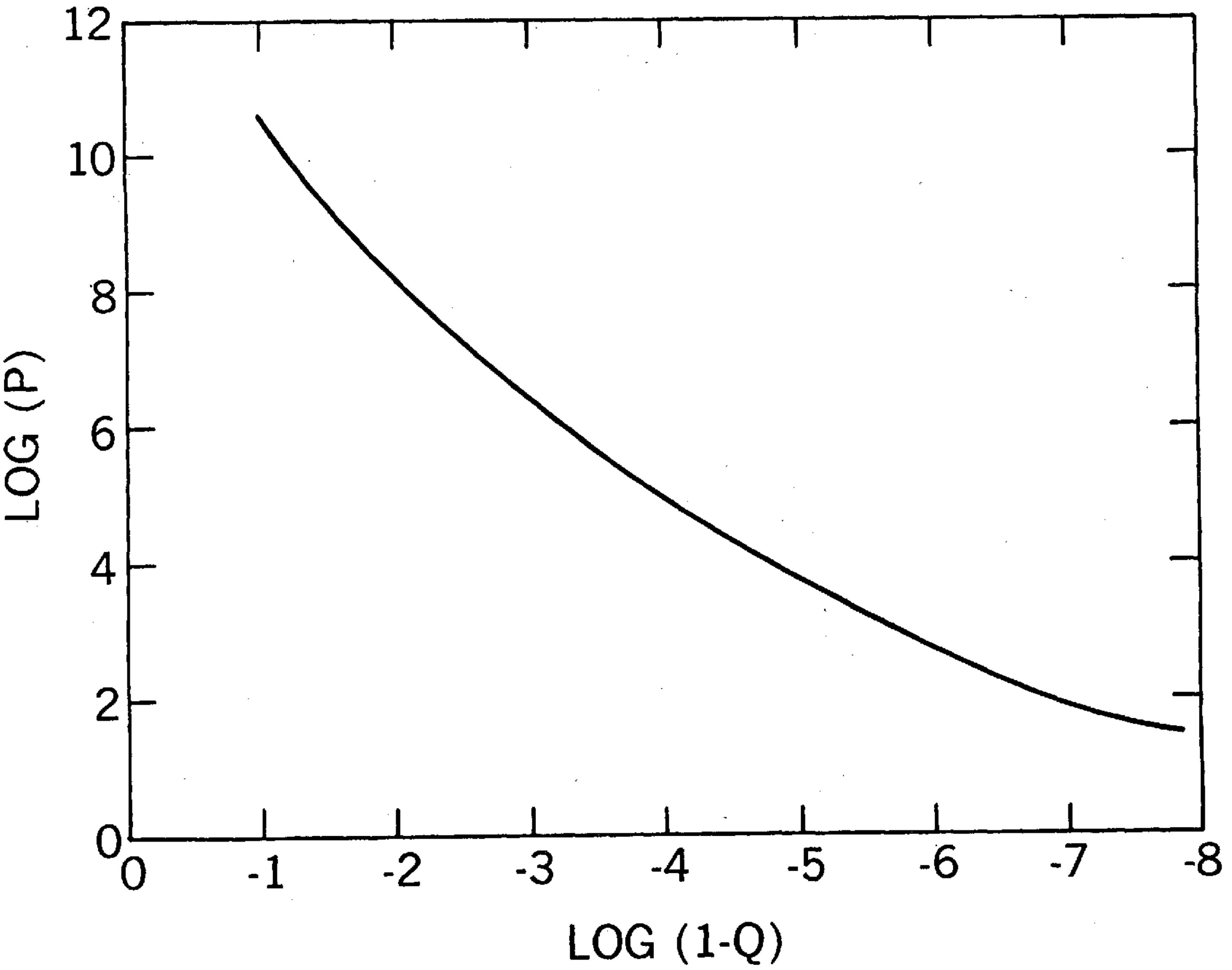
12
10
8
6
4
2
0
LOG (P)
0
-1
-2
-3
-4
-5
-6
-7
-8
LOG (1-Q)

[illegible]

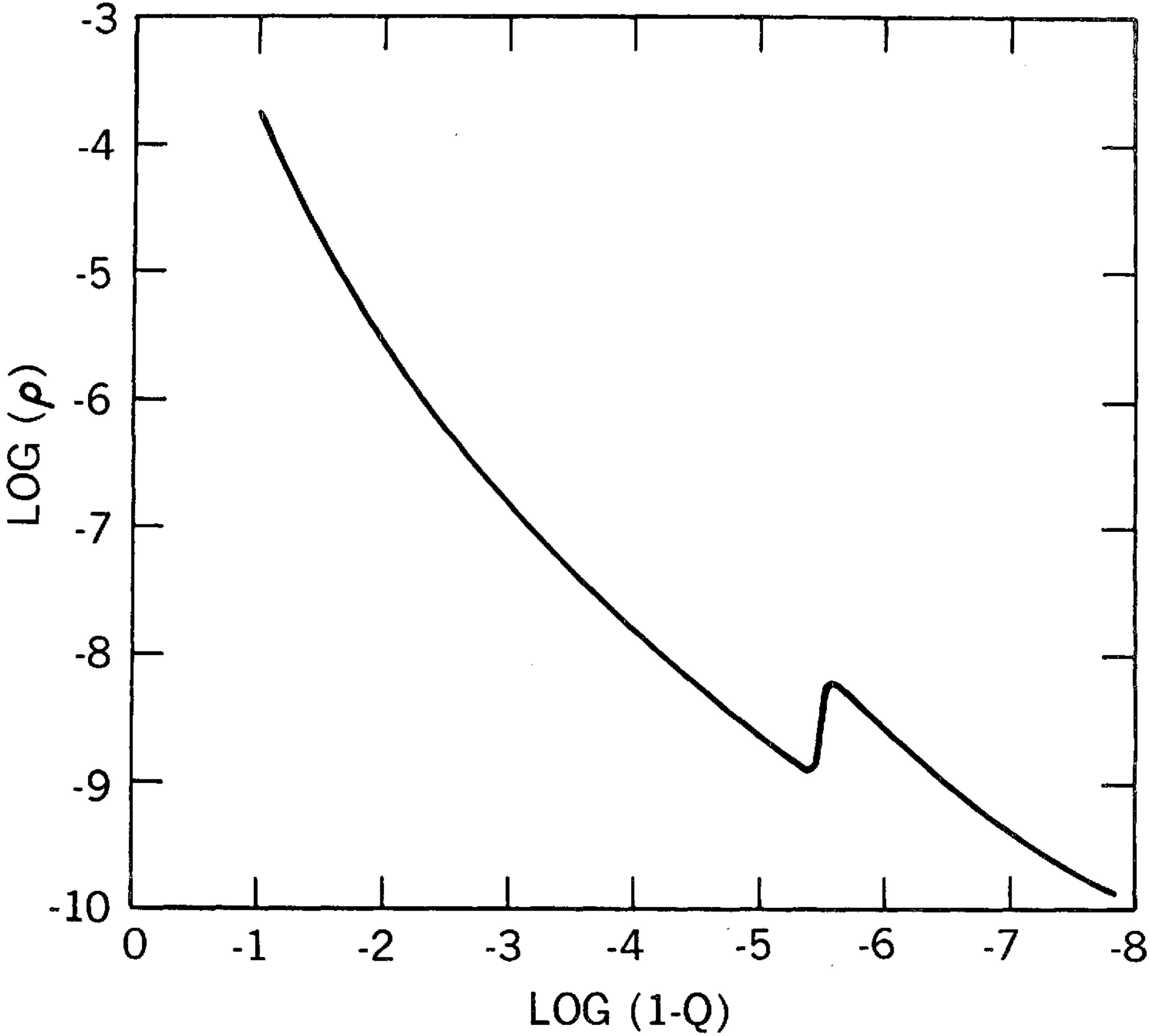

Figure III-3. log ρ vs. log (1-Q) in the equilibrium model

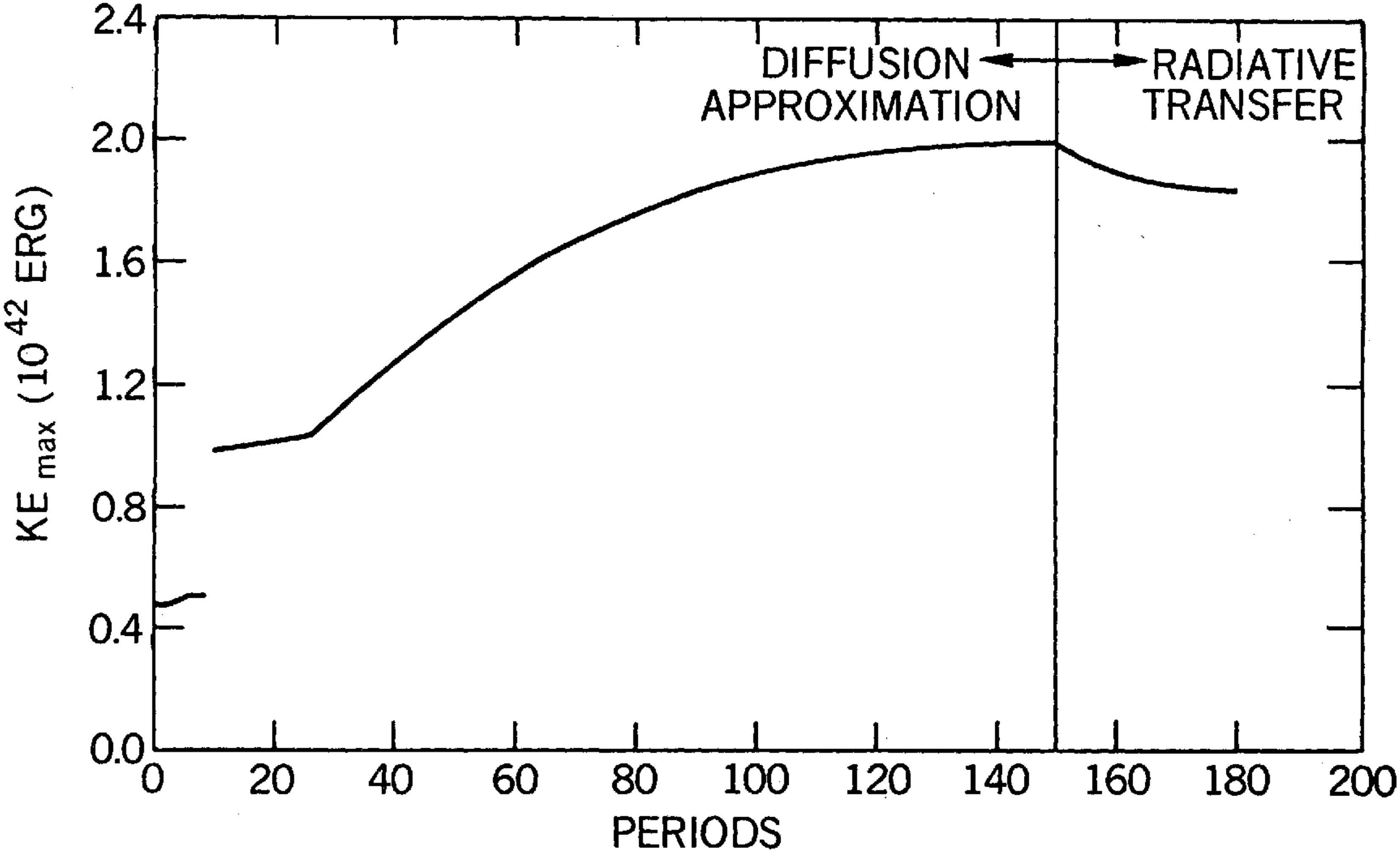

Figure III-4. Approach of KE$_{max}$ to full amplitude. The periods for which the diffusion approximation and solution of the transfer equation were used are indicated.

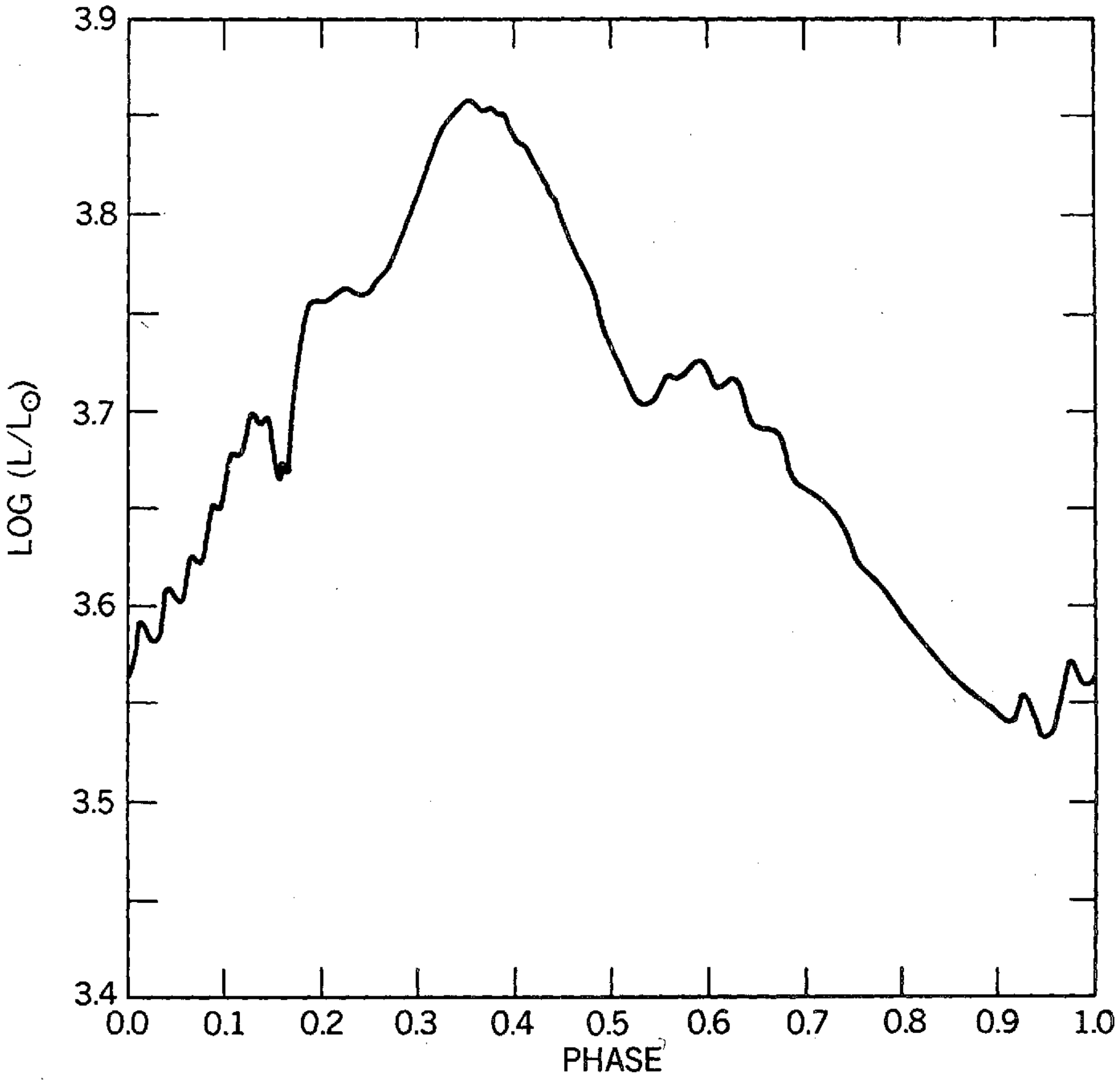

Figure III-5. log L/L$_\odot$ vs. phase for the full amplitude model

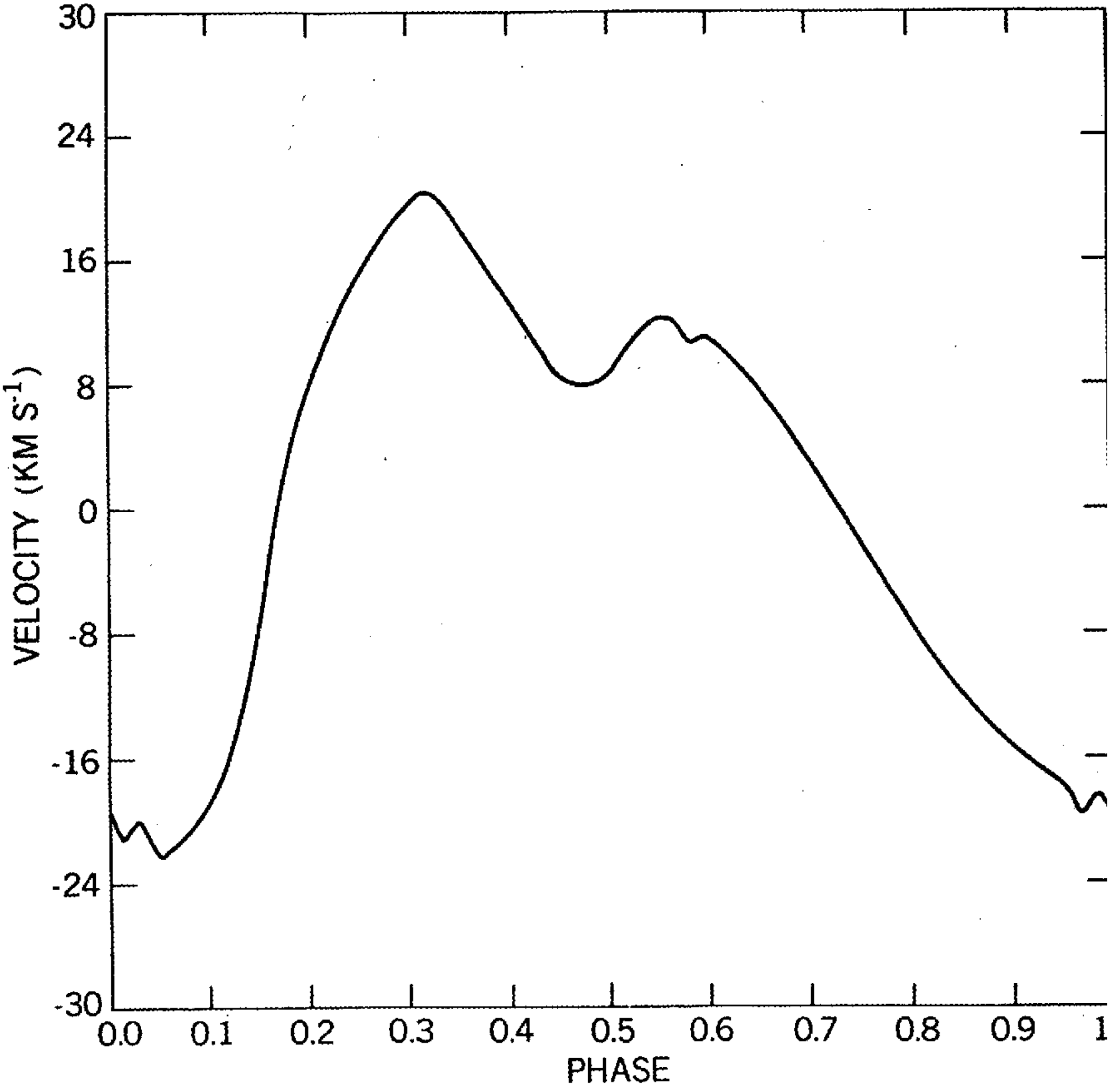

Figure III-6. Velocity at $\tau = 0.2$ vs. phase for the full amplitude model

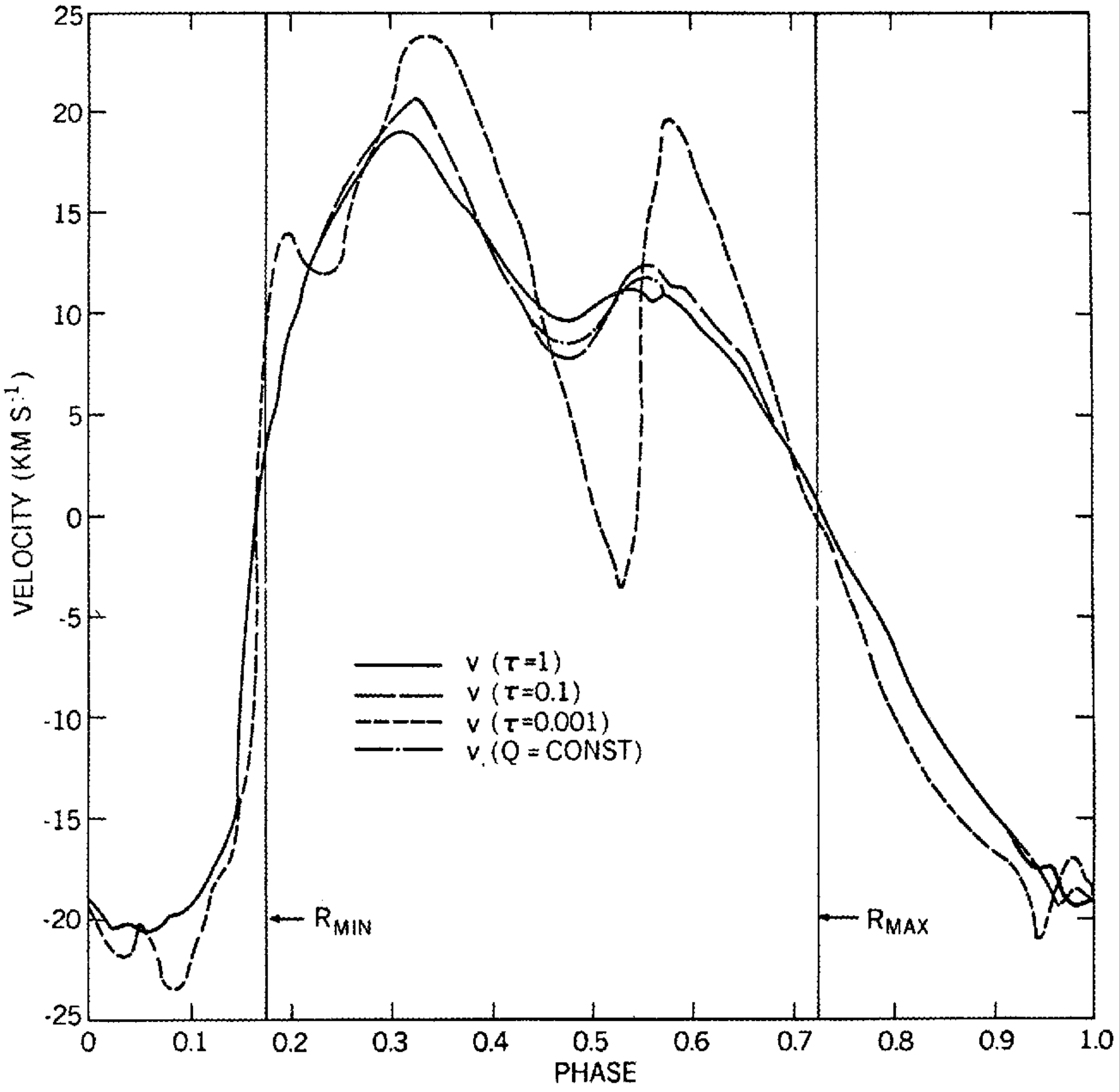

Figure III-7. Velocity curves for the full amplitude model

]

Figure III-8. Luminosity vs. mass point and phase. Every second mass point has been plotted. Point A is in the HeII ionization zone; point B, the top of the quasi-adiabatic envelope; point C, the atmosphere.

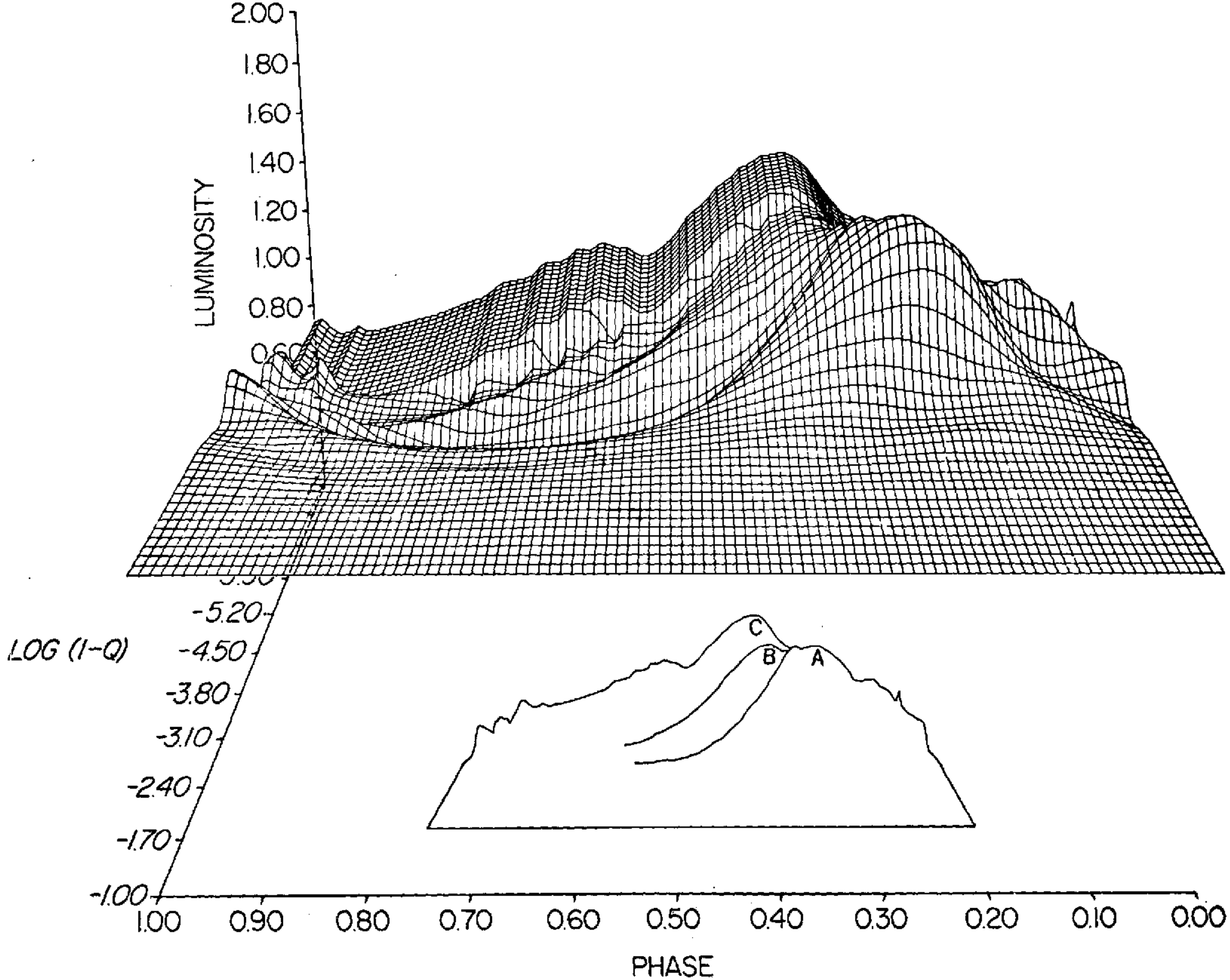
2.00
1.80
1.60
1.40
1.20
1.00
0.80
0.60
LUMINOSITY
LOG (1-Q)
-5.20
-4.50
-3.80
-3.10
-2.40
-1.70
-1.00
C
B
A
1.00
0.90
0.80
0.70
0.60
0.50
0.40
0.30
0.20
0.10
0.00
PHASE

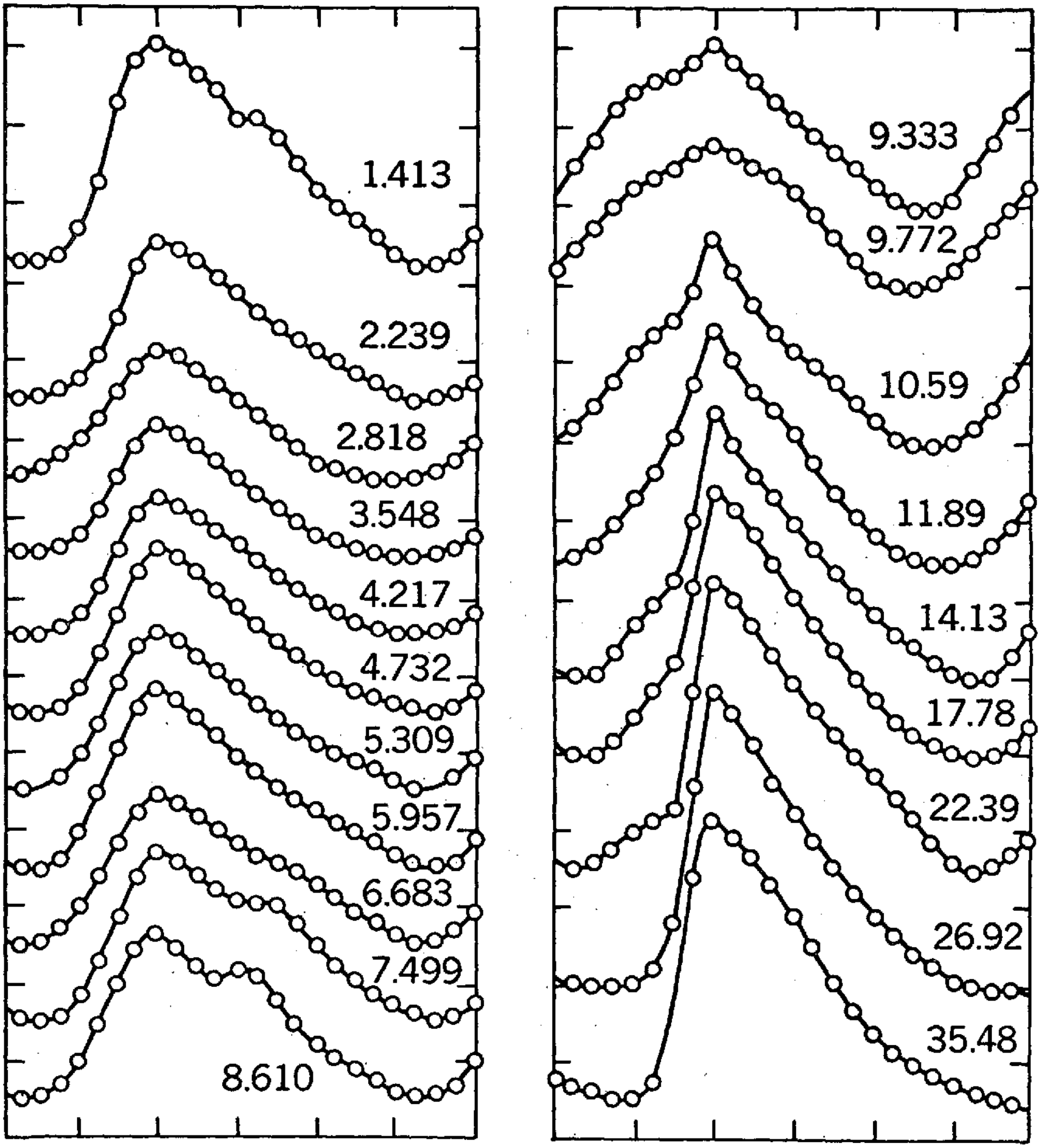

Figure III-9. Observed light curves of Cepheids illustrating the Hertzsprung sequence. (from Payne-Gaposhkin 1951).

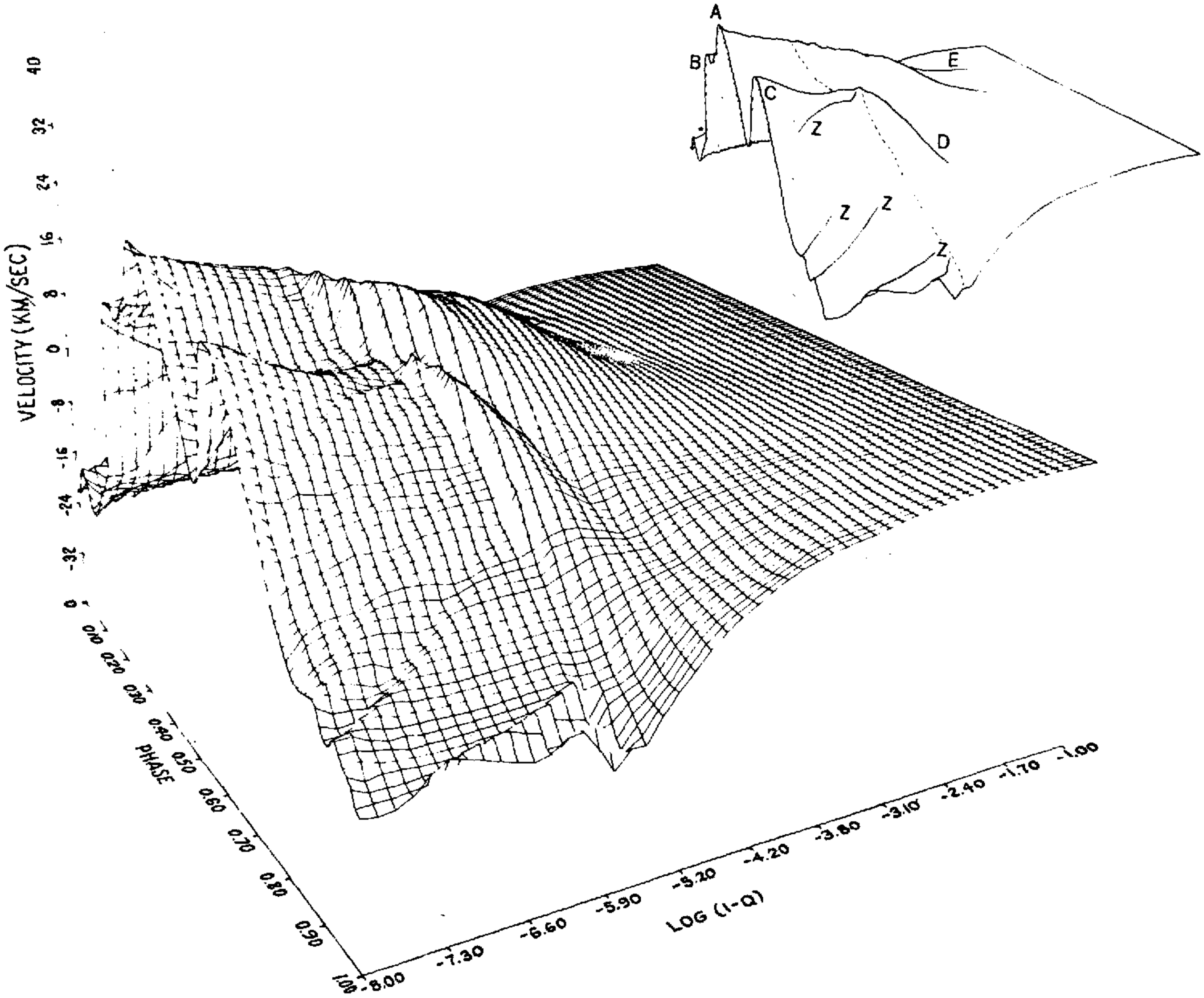

Figure III-10. Velocity vs. mass point and phase.

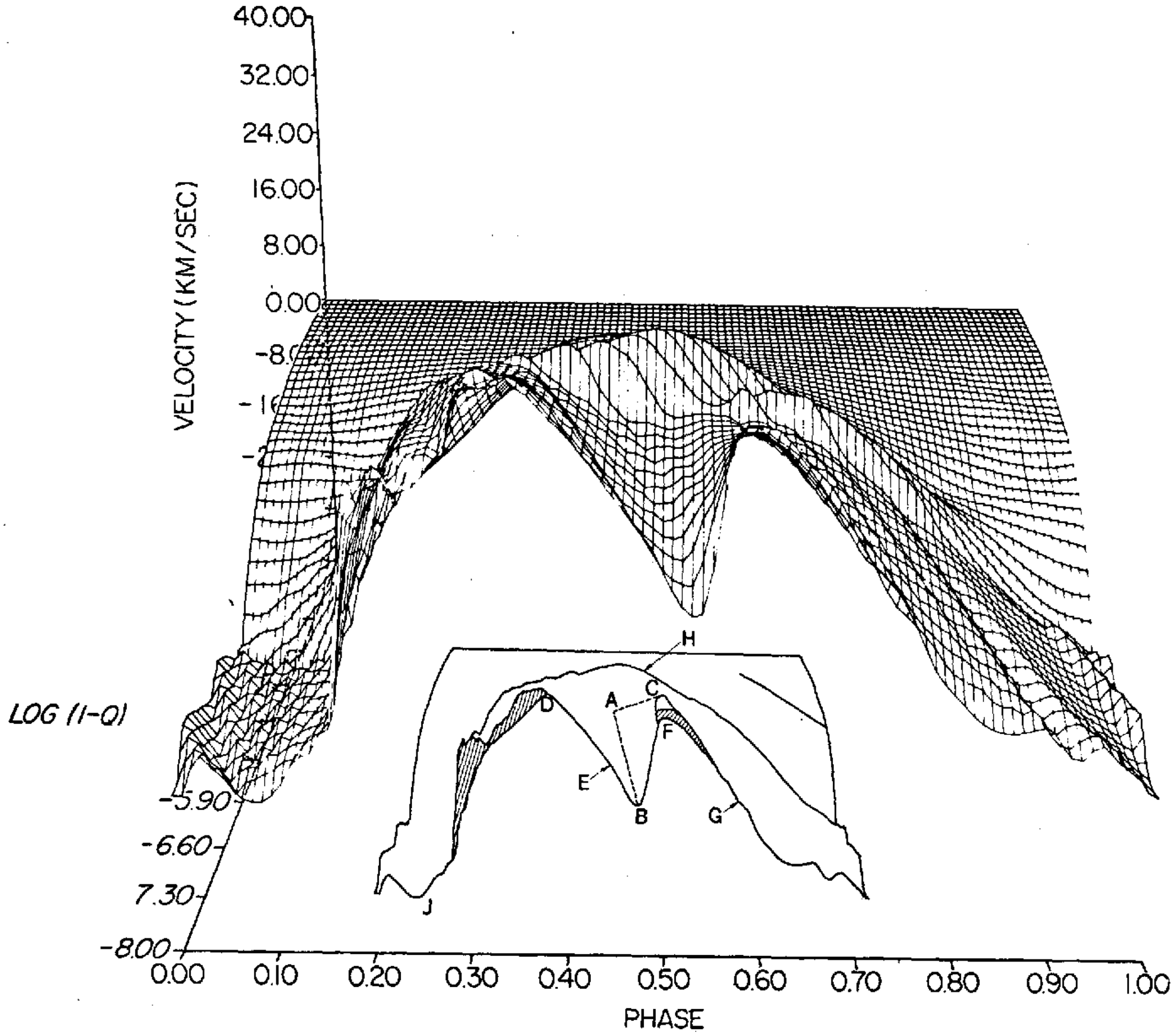

Figure III-11. Velocity vs. mass point and phase

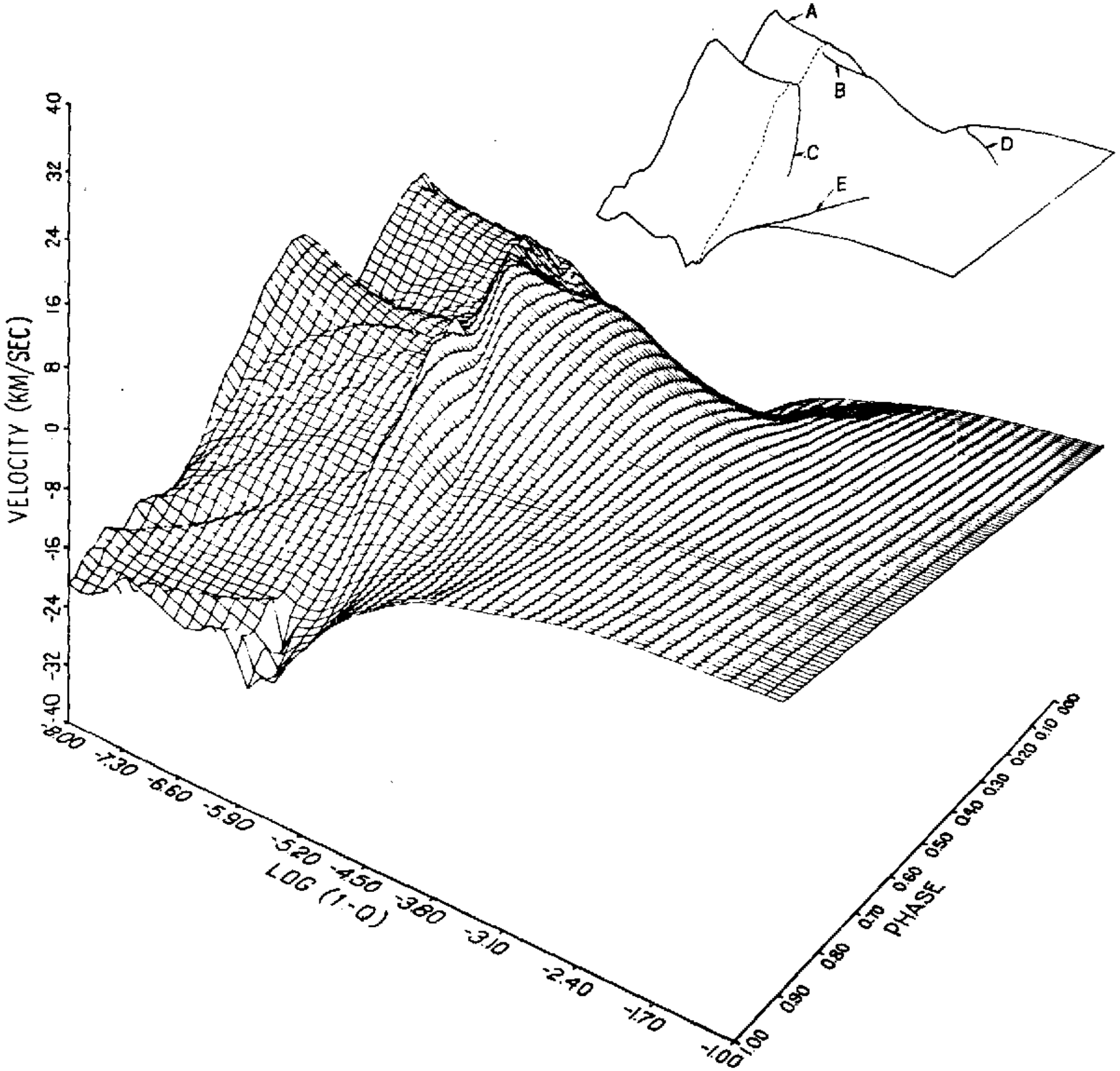

Figure III-12. Velocity vs. mass point and phase

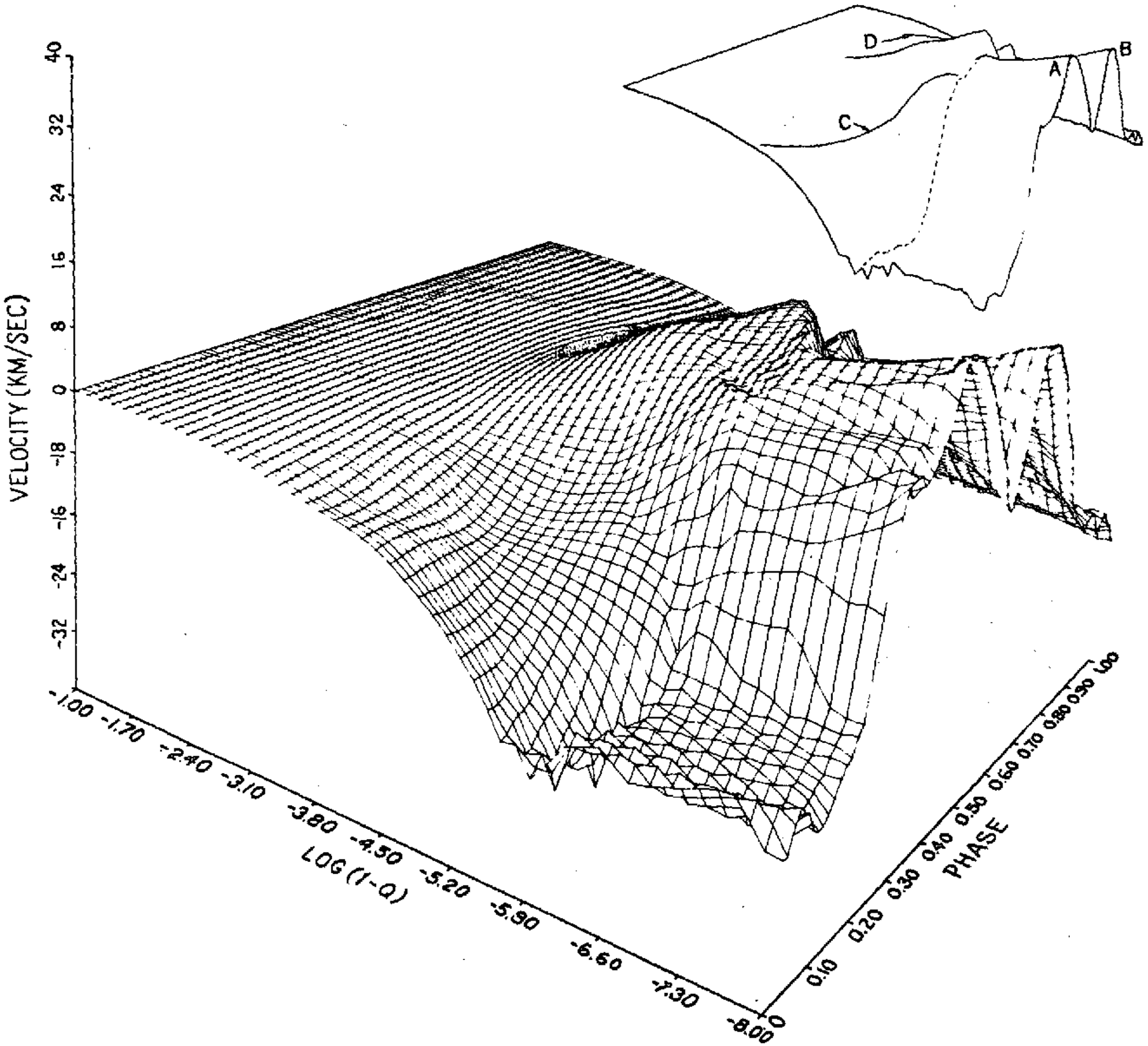

Figure III-13. Velocity vs. mass point and phase

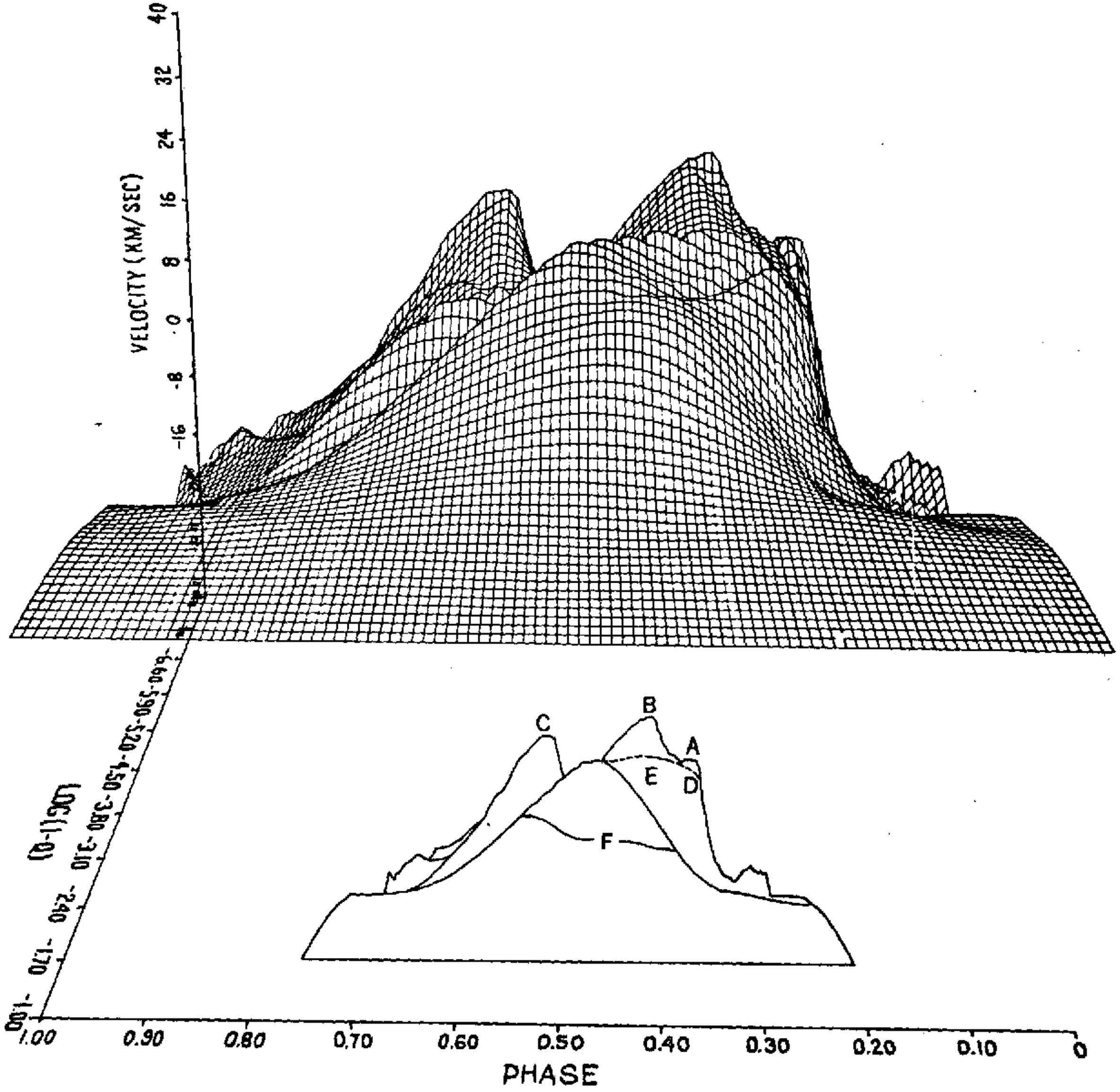

Figure III-14. Velocity vs. mass point and phase

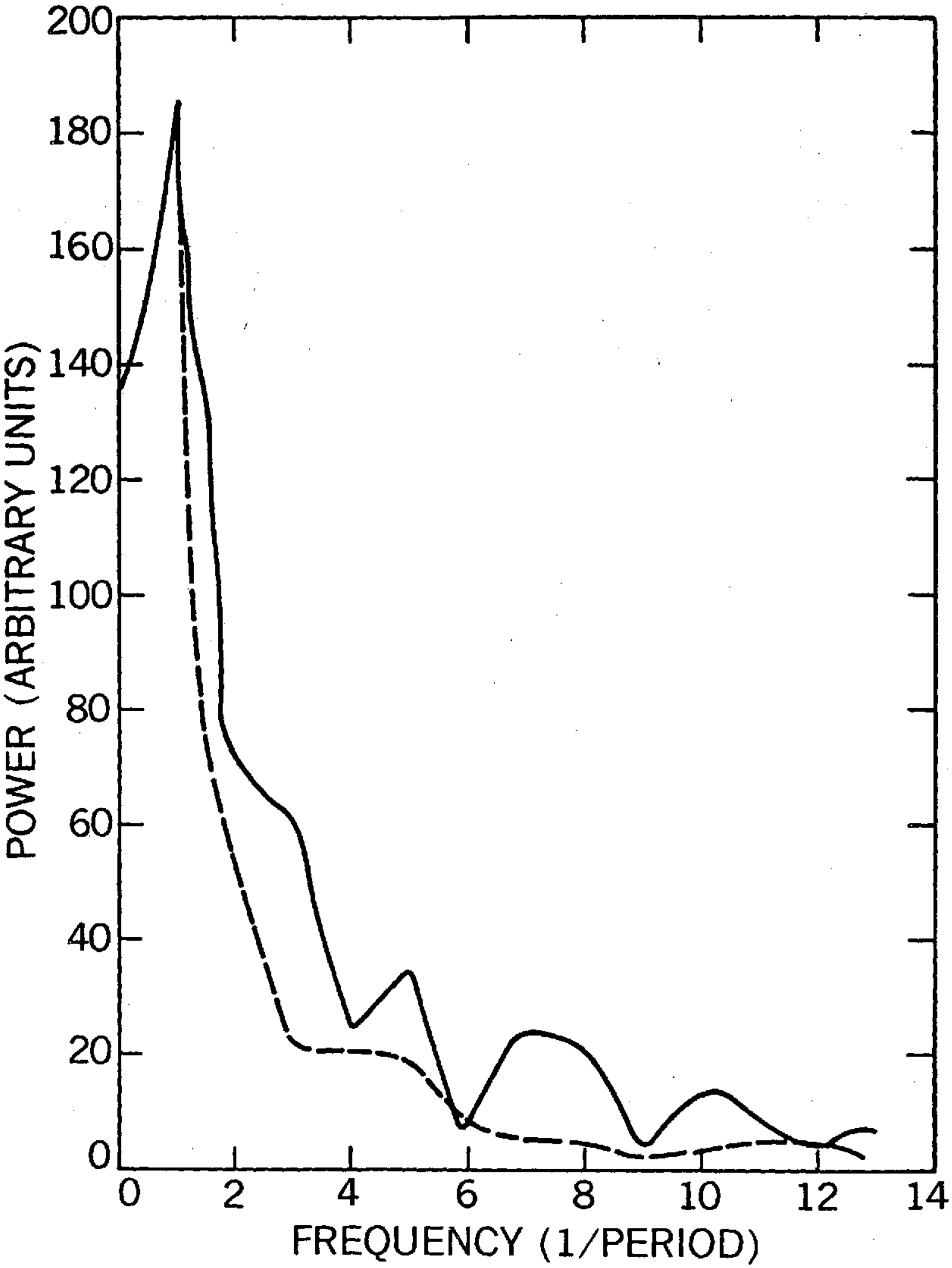

Figure III-15. Power spectra of velocity curves. —— atmospheric zone, --- envelope zone.

CHAPTER IV

CONTINUOUS SPECTRUM

A. Atmosphere calculation.

1. Snapshot approach.

In the preceding chapters the model has been discussed in terms of pulsation theory. Since many optically thin zones were included in the calculation of the hydrodynamic models, it is also possible to discuss the model in terms of stellar atmospheres. The hydrodynamic equations (II-1) to (II-5) are most easily solved if a Lagrangian mass coordinate is used as the independent variable. On the other hand, the light emerging from a model is more easily computed if the optical depth, τ, is the independent variable. The physical parameters of primary interest are also different. For example, while the total pressure is needed to calculate the hydrodynamic motions, the electron pressure is more important for determining the emergent spectrum.

To facilitate the stellar atmosphere calculations, the optically thin zones of the hydrodynamic models were used as snapshots of the atmospheric structure. Since all relevant physical variables change on a time scale much greater than the time it takes a photon to diffuse through the atmosphere, no large errors are introduced by using this snapshot approximation. This assumption is the same one made in dropping terms of order v/c in the transfer equation. After describing the methods used to convert the hydrodynamic models to a form suitable for the atmosphere calculations, the properties of the continuous spectrum will be discussed in the remainder of this chapter. Chapter V will be devoted to a discussion of the line spectrum.

2. Converting the models.

The hydrodynamic models at 200 phases at equal phase intervals of 0.005 period were converted to a form with Rosseland mean optical depth, $d\tau = \kappa\rho\, dr$, as the independent variable. The atmospheric models were computed starting at the surface and were continued inward until the temperature reached 25,000°K. In all cases the base of the atmosphere was at a large enough optical depth that including more points would not change the computed spectrum.

Before computing the emergent spectrum, the electron pressure, P_e, had to be determined. Since P_e depends on the number of free electrons determined from the Saha equation, and P_e is needed to compute the ionization fractions, an iteration must be performed to find P_e. This iteration is described in Appendix C. Knowing the variation of temperature, density, radius, and electron pressure with optical depth makes it possible to compute the spectral energy distributions of the models. The monochromatic opacity, κ_λ, was computed with a code written by Bell (1974) that includes the continuous opacities of H, H^-, H_2, H_2^-, He, He^-, SiI, MgI and Rayleigh scattering. Next the monochromatic optical depth scale was computed from

$$\tau_\lambda = \int_0^\tau \frac{\kappa_\lambda}{\kappa}\, d\tau,$$

and the transfer equation was solved to give the flux at the desired wavelength, F_λ.

The wavelength region from 912Å to 5μ was divided into 21 wavelength bands whose boundaries occur at the absorption edges of the continuous opacity sources. A Gauss-Lobatto quadrature using 4, 6, or 10 wavelength points was performed for each band. The sum of the contributions of these bands represents the total flux of the model

$$F = \int_0^\infty F_\lambda d\lambda = \sum_{i=1}^{134} F_{\lambda i} W_i = \sigma T_{eff}^4/\pi \tag{IV-1}$$

Equation (IV-1) was used to define the effective temperature of the model, T_{eff}, at each phase.

The total flux was defined as the integral of F_λ not F_ν since $F_\lambda(\lambda = 5\mu) / \max F_\lambda \sim 10^{-2}$ while $F_\nu\ (\lambda = 5\mu) / \max F_\nu \sim 10^{-1}$. Since there is essentially no flux shortward of 912Å for stars in this temperature range, the integration can be computed with fewer quadrature points if F_λ is used. Computing $\int_0^\infty B_\lambda d\lambda$ with these quadrature points resulted in an error of 0.3%. Before these fluxes can be used to compute colors, the effect of the spectral lines must be taken into account.

3. Line blocking approximation.

In the range of spectral types populated by Cepheids, the contribution of spectral lines to the total opacity is large in certain wavelength regions. Because including the effect of lines in the monochromatic opacity would require an excessive amount of computer time, the line blocking approximation was used. In this approximation, the flux in each wavelength band is multiplied by a line blocking factor, $0 \leq \eta \leq 1$, which represents the fraction of the flux absorbed by the lines in the band. The line blocked flux, F_B, is then defined by

$$F_B = (1 - \eta_\lambda)\, F_U, \qquad \text{(IV-2)}$$

where F_U is the flux computed including only continuum opacity sources. This approximation does not conserve energy since the flux removed by the lines is simply ignored; but, since gray radiative transfer was used to compute the hydrodynamic structure, it was felt that use of the line blocking approximation was warranted.

Figure IV-1 shows η vs. λ for a model taken from Parsons (1969) having T_{eff} = 6000°K and log g = 1.8. The line blocking factors are those of Bell (1974). Figure IV-2 illustrates the difference between F_B and F_U. The dashed line is the spectral energy distribution computed using only continuous opacity sources; the solid line includes the line blocking factors shown in Figure IV-1. Note the linear scale of the ordinate chosen to accentuate the difference between F_B and F_U. It is clear from Figure IV-2 that the line blocking has a reasonably large effect on the U, B, and V magnitudes but changes the R and I magnitudes only slightly.

The line blocking factors are in the form of tables of η vs. λ for a set of T_{eff} and g_{eff}. Before the line blocking factors can be applied to the hydrodynamic models, T_{eff} and g_{eff} must be defined. The method used is described in the following section.

4. Effective temperature and gravity.

The parameters of major importance in the hydrodynamic calculations were the luminosity emerging from the model and the radius of the photosphere. The line blocking factors, though, are tabulated in terms of T_{eff} and g_{eff}. The effective temperature of the model can be found by solving $L = 4\pi R^2 \sigma T_{eff}^4$, but determining g_{eff} is more complicated. A stellar atmosphere is hydrostatic equilibrium has a unique gravity,

$g = GM / r^2$. The hydrodynamic models, on the other hand, are experiencing accelerations and each zone has an effective gravity given by

$$g_{eff} = - \frac{dP}{dm} = - \frac{GM}{r^2} + \ddot{r}, \qquad \text{(IV-3)}$$

where $\ddot{r}$ is the acceleration of the zone. A suitable method for finding the mean value of g_{eff} in the line forming region of the atmosphere was needed.

A stellar atmosphere is normally defined in terms of T_{eff} and g_{eff}. T_{eff} is a measure of the temperature of the model; g_{eff}, of the pressure. For this reason, the mean effective gravity of the atmosphere, $\bar{g}_{eff}$, was defined from equation (IV-3) as

$$\bar{g}_{eff} = \frac{\int_0^\infty \left| \frac{dP}{dm} \right| e^{-\tau/\tau_o} \, d\tau}{\int_0^\infty e^{-\tau/\tau_o} \, dt} , \qquad \text{(IV-4)}$$

where $\tau_0 = 0.1$ was chosen to limit the average to the line forming region. This value of $\bar{g}_{eff}$ was used along with T_{eff} to determine the line blocking factors at each phase.

The variations of T_{eff} and g_{eff} with phase are shown in Figures IV-3 and IV-4, respectively. The large spike in log g_{eff} and the dip in T_{eff} near phase $\Phi = 0.15$ may be artifacts of the artificial viscosity (see Chapter III). The large increase in log g_{eff} near $\Phi = 0.5$, on the other hand, is real and is caused by a shock moving out through the atmosphere. If the feature near $\Phi = 0.15$ on the log g_{eff} curve is ignored, the variation is found to be less than has been observed by Schwartzchild, Schwartzchild, and Adams (1948), Schmidt (1971b), and Parsons (1971 a,b). This difference is not significant since g_{eff} of RDT was found by averaging over the entire atmosphere while the observed dynamic gravities refer to a small part of the atmosphere. The g_{eff} variation of a given zone is much larger but spurious accelerations due to zoning effects are also enhanced.

Oke, Giver, and Searle (1962) in their analysis of the RR Lyra star SU Draconis found a range of phases having roughly constant T_{eff} and g_{eff}. As shown in Figure IV-5, RDT behaves differently. Ignoring the effects of the atmospheric snock wave and the spike caused by the artificial viscosity (by following the dashed lines in Figure IV-5) gives an open curve in the log g_{eff} - log T_{eff} diagram. During rising and falling light, the atmosphere moves at nearly constant g_{eff}, i.e., isobarically, while near maximum and minimum light, it changes isothermally. If it is assumed that the pressure at some point in the atmosphere is proportional to g_{eff}, and that the perfect gas law with T_{eff} and this pressure can be used to find the specific volume, V, a P - V diagram can be constructed (Figure IV-6). The dashed lines in Figure IV-5 have been followed in constructing this diagram. Following the actual gravity variation instead results in the addition of two long, narrow loops containing little enclosed area. Since these loops needlessly clutter the diagram and contribute little to the discussion, they are not shown. The area enclosed by this curve indicates that the atmosphere has a destablizing effect on the model. Although this curve is not a proper thermodynamic integral since it does not follow a given mass element, Christy (1962), who constructed a similar diagram from observations of SU Dra, concludes that this P - V diagram reflects the influence of the HIR on the star.

5. Defining the color system.

Once T_{eff} and g_{eff} have been found for each model, the line blocking factors can be applied to the spectral energy distributions computed above, and the broad band UBVRI colors can then be calculated. The relative filter sensitivity functions for the U, B, and V filters were taken from Azusienis and Straizys (1969) and those of R and I from Johnson (1964). These magnitudes were on an arbitrary scale. In order to make comparisons with observations, V, U-B, B-V, V-R, and R-I were converted to Johnson's system using least squares fits to

$$C_J = a + bC, \qquad \text{(IV-5)}$$

where

C_J = color in Johnson' system,

C = color in arbitrary system.

Line blocked spectral energy distributions of Parsons' (1969) models were used for the calibration. Unfortunately, there was no single source available that gives the Johnson colors needed for the transformations (IV-5). The $(U-B)_J$ and $(B-V)_J$ colors were taken from Bell and Parsons (1974); $(R-I)_J$ was taken from Schmidt (1973); $(V-R)_J$ was computed from the calibration by Caputo and Natta (1973). The absolute visual magnitudes, V, were computed from the bolometric magnitude using the bolometric correction of Kraft (1961). All colors given in the following are on Johnson's system.

The absolute visual magnitude light curve, M_V vs. Φ is shown in Figure IV-7. Although the zoning effects are smaller than $0\overset{m}{.}05$, it was found that they masked features of interest on the HR and color-color diagrams. The light curves were, therefore, smoothed to minimize these zoning effects. These smoothed light curves shown in Figure IV-8 were used for the comparison with observations discussed in the next section.

B. Comparison with observations.

1. Light curve parameters.

The light curves computed in the previous section were compared with observations. Since the model was not selected to represent a specific star, the theoretical results were compared with the mean properties of Cepheids with periods near 12^d. In Figure IV-8, the increase of light amplitude with decreasing effective wavelength is readily apparent. Somewhat less apparent, but still discernable, is the phase shift noted by Stebbins, Kron, and Smith (1952) and Wisniewski and Johnson (1968). This phase shift is in the sense that long wavelength light curves lag short wavelength light curves. The phase shift between the U and I curves of RDT is about 0.04 period in good agreement with observations. Table IV-1 compares the light amplitude of RDT with observed values from Wisniewski and Johnson (1968). Unfortunately, the only Cepheid they observed with a period near 12^d is ζ Gem, a star with a low-amplitude, symmetric light curve. The table shows that the RDT amplitudes fall within the observed ranges.

RDT can also be compared with the light curve parameters published by Schaltenbrand and Tammann (1971). Table IV-2 compares RDT with all classical Cepheids in the period range 11^d to 13^d that they observed. Again the values for RDT fall within the range of observed quantities. Figure IV-9 and Table IV-3 give the adopted light and color curves for RDT.

2. Color-temperature relations.

A further check on the models can be made. By treating each of the 200 models as an independent observation, the color-temperature laws can be computed. Figure IV-10 shows the dependence of (U-B), (B-V), (V-R), and (R-I) on log T_{eff}. The dependence of (U-B) on g_{eff} produces the open curve in the (U-B)-log T_{eff} plane. The (B-V), (V-R), and (R-I) curves, on the other hand, closely approximate straight lines and should, therefore, be good temperature indicators. The fits to the relationships

$$\log T_{eff} = a + b(X-Y),$$

and

$$\theta_{eff} = c + d(X-Y),$$

where (X-Y) represents the color, are given in Table IV-3, as are the relationships derived by Schmidt (1971a). For comparison, Kraft (1961) gives $\log T_{eff} = 3.886 - 0.175\,(B-V)$ and Rodgers (1970) gives $\theta_{eff} = 0.64 + 0.337\,(B-V)$.

This agreement with the observed values is much better than expected and results from partial cancellation of two errors. Ignoring convection produces a model having too large a temperature gradient in the photosphere. Using the line blocking approximation, which neglects the backwarming effect of the line opacity, produces a model having too small a temperature gradient. Ignoring both effects results in a temperature structure closely approximating that of the stars studied. Since the observed color-temperature laws were derived using nonpulsating super-giants and hydrostatic model atmospheres, the accuracy of the color temperature fits indicates that deviations from radiative equilibrium must be small, as predicted by Whitney (1967). The use of static model atmospheres to study the colors of Cepheids should, therefore, produce reliable results.

C. Loops in the (U-B)-(B-V) diagram.

Having established that the colors of RDT reproduce the observed colors allows the models to be used to answer questions requiring a theoretical approach. One of these questions has already been answered. The hydrodynamic atmospheres are nearly in radiative equilibrium at most phases and can be approximated by a series of hydrostatic model atmospheres.

Another interesting question is the cause of the loops in the (U-B) - (B-V) diagram. Abt (1959) has suggested that the loops are caused by

a) excess ultraviolet emission from shocks,
b) sensitivity of the continuous opacity, κ_C, to the electron pressure, P_e,
c) unusual line blanketing,
d) lines being partially filled in by emission lines,
e) continuous emission possibly originating in a chromosphere, or
f) non-thermal dependence of line strength (i.e., with P_e).

Figure IV-11a shows the color-color diagram for RDT. The curve resembles that of η Aql and would be classified by Nikolov and Kunchev (1969) as being linear or nearly linear. The curve is noticeably open from phase $\Phi = 0.1$ to $\Phi = 0.5$ having a maximum width of $0\overset{m}{.}04$ in (U-B). Since neither emission lines nor chromospheric emission was included in the model, the loops could not be produced by (d) or (e). Figure IV-11b shows the color-color diagram for RDT excluding the line blocking factors. Due to the change of scale the curve appears to be much more open but still has a maximum width of $0\overset{m}{.}05$ in (U-B). Since lines have not been included in calculating this case, the openness cannot be explained by (c) or (f). There is a strong shock in the atmosphere only near $\Phi = 0\overset{m}{.}5$ and the excess emission amounts to about $0\overset{m}{.}02$ in (U-B). Possibility (a), therefore, can be excluded. Only (b), the sensitivity of κ_C to P_e, remains. In the temperature range of RDT, the continuous opacities of H and H^- are the primary opacity sources. In the atmosphere, most of the free electrons come from the metals, and the ionization of the metals depends linearly on P_e through the Saha equation. Since the wavelength dependences of the H and H^- continuous opacities differ, a change of P_e at fixed temperature will change H^-/H and, therefore, the wavelength dependence of κ_C. Since the U filter contains the Balmer jump, this effect will be more pronounced in U than in B or V, producing a loop in the color-color diagram.

D. Mean colors of Cepheids.

Figure IV-12 indicates another problem. The model traces an open path in the HR Diagram running nearly parallel to the lines of constant period and covering the entire width of the instability strip. Many attempts at defining period-luminosity or period-luminosity-color relations depend on the mean values of the luminosity and colors. There are at least 3 distinct methods for computing these means,

a) the intensity mean of the color-$\langle B-V\rangle_I$,

b) the magnitude mean of the color-$\langle B-V\rangle_M$,

c) the difference of the intensity means of two magnitudes-$\langle B\rangle_I - \langle V\rangle_I$,

Unfortunately, these method do not give the same results. Table IV-4 compares these means with the colors of STB. Method (c) is normally considered to be the most physically meaningful average since conservation of energy in a steady state system requires

$$\langle L \rangle = \frac{1}{P}\int_0^P L dt = L_{STB},$$

where L is the bolometric luminosity and P the period. There is nothing to require this relationship to hold in a limited wavelength region, however, since the wavelength dependence of the luminosity varies during the cycle. Table IV-4 indicates, however, that method (c) does best reproduce the values for STB confirming the results of Cox and Wing (1973). The discrepancy between the mean values of (U-B) from methods (a) and (b) and that of STB is difficult to explain, but there appear to be two possibilities. First, since the U filter contains the Balmer jump, it is sensitive to the confluence of the hydrogen lines near 3650Å and, therefore, to g_{eff}. Second, the U filter contains the wavelengths with both the largest and the smallest opacities. The U magnitude, therefore, is affected by a larger region of the atmosphere than the other filters. Deviations from radiative equilibrium will affect the U magnitude for a larger fraction of the cycle than it will the other magnitudes. In either case, the larger amplitude in U will accentuate the differences among the averaging schemes.

E. Zero point of the P-L relation.

One further point of interest is the location of STB in the HR Diagram. The + in Figure IV-12 marks the location of STB and the dashed lines show the Sandage and Tammann (1969) instability strip and two lines of constant period. The location of STB indicates that the zero point of the Sandage and Tammann P-L-C relation should be lowered by $0^m.2$. Iben and Tuggle (1971b) suggest that this large a change is reasonable considering the uncertainties in defining the zero point. Unfortunately, they suggest an upward revision to remove the discrepancy between the pulsational and evolutionary masses. On the other hand, recent studies of the zero point using secular parallaxes indicate the adopted zero point might be too high. Jung (1970) finds that the shift should be $\Delta M = 0\overset{m}{.}4 \pm 0\overset{m}{.}4$ while Wielen (1974) gives $\Delta M = 0\overset{m}{.}2 \pm 0\overset{m}{.}4$. Wielen points out that the increase in the zero point required by Iben and Tuggle cannot be ruled out and is just barely tolerable.

Due to the approximations made in computing the models, the results presented in this chapter must be considered tentative. More accurate models are needed to verify the correctness of these conclusions. The inaccuracies of the models are even more important when the line profiles are considered in the next chapter.

Table IV-1

Comparison of observed and computed light amplitudes

STAR	P	ΔU	ΔB	ΔV	ΔR	ΔI
X CYG	16.4	2.4	1.6	1.0	0.60	0.42
RDT	12.1	1.9	1.6	1.0	0.55	0.45
U AQL	7.0	1.5	1.2	0.8	0.52	0.42

Table IV-2

Comparison of observed and computed light curve parameters

STAR	ΔV	Δ(B-V)	Δ(U-B)	ΔΦ
RX AUR	.692	.356	.461	.505
SS CMA	.992	.457	.485	.553
XX CAR	.835	.457	-	.642
RY CAS	.969	.494	.528	.599
XX CEN	.886	.453	.508	.511
KK CEN	.979	.539	-	.528
SU CRU	.678	.663	.668	.664
FZ CYG	.778	.525	.533	.519
AA GEM	.672	.434	.457	.532
UU MUS	1.031	.582	.705	.636
U NOR	.967	.472	.553	.541
SY NOR	.890	.334	.319	.646
SV PER	.787	.404	.293	.609
Z SCT	1.001	.549	.831	.596
TY SCT	.881	.453	.678	.534
DR VEL	.570	.342	-	.544
RDT	.99	.49	.46	.57

Table IV-3

Adopted light and color curves

Φ	M_{BOL}	M_V	U-B	B-V	V-R	R-I
0.00	-4.051	-3.922	0.648	0.807	0.674	0.461
0.05	-4.132	-4.039	0.553	0.736	0.627	0.427
0.10	-4.275	-4.223	0.445	0.628	0.555	0.380
0.15	-4.347	-4.310	0.381	0.568	0.517	0.351
0.20	-4.510	-4.500	0.345	0.490	0.454	0.314
0.25	-4.537	-4.525	0.351	0.506	0.463	0.313
0.30	-4.657	-4.647	0.327	0.439	0.426	0.298
0.35	-4.758	-4.758	0.338	0.423	0.402	0.289
0.40	-4.720	-4.717	0.360	0.460	0.426	0.306
0.45	-4.612	-4.592	0.383	0.513	0.470	0.336
0.50	-4.457	-4.403	0.434	0.611	0.544	0.372
0.55	-4.405	-4.337	0.467	0.642	0.565	0.390
0.60	-4.421	-4.354	0.483	0.649	0.567	0.393
0.65	-4.369	-4.290	0.543	0.704	0.597	0.411
0.70	-4.280	-4.174	0.607	0.763	0.641	0.436
0.75	-4.195	-4.062	0.678	0.833	0.681	0.457
0.80	-4.102	-3.944	0.717	0.843	0.706	0.482
0.85	-4.030	-3.854	0.754	0.871	0.725	0.497
0.90	-3.972	-3.782	0.781	0.914	0.746	0.503
0.95	-3.973	-3.802	0.752	0.886	0.725	0.493

Table IV-4

Color-temperature relations

$$\log T_{eff} = a + b(X-Y)$$

$$\theta_{eff} = c + d(X-Y)$$

	Present		Present		Schmidt (1971)	
	a	b	c	d	c	d
B-V	3.877	-.174	.642	.349	.641	.309
V-R	3.906	-.252	.583	.505	.543	.593
R-I	3.918	-.394	.561	.791	.574	.773

Table IV-5

Magnitude and intensity mean colors

	U-B	B-V	V-R	R-I	V
$\langle X-Y\rangle_I$	.507	.654	.571	.393	
$\langle X-Y\rangle_M$	.518	.665	.576	.396	-4.261
$\langle X\rangle_I-\langle Y\rangle_I$	.451	.614	.552	.386	-4.302
STB	.433	.634	.575	.386	-4.273

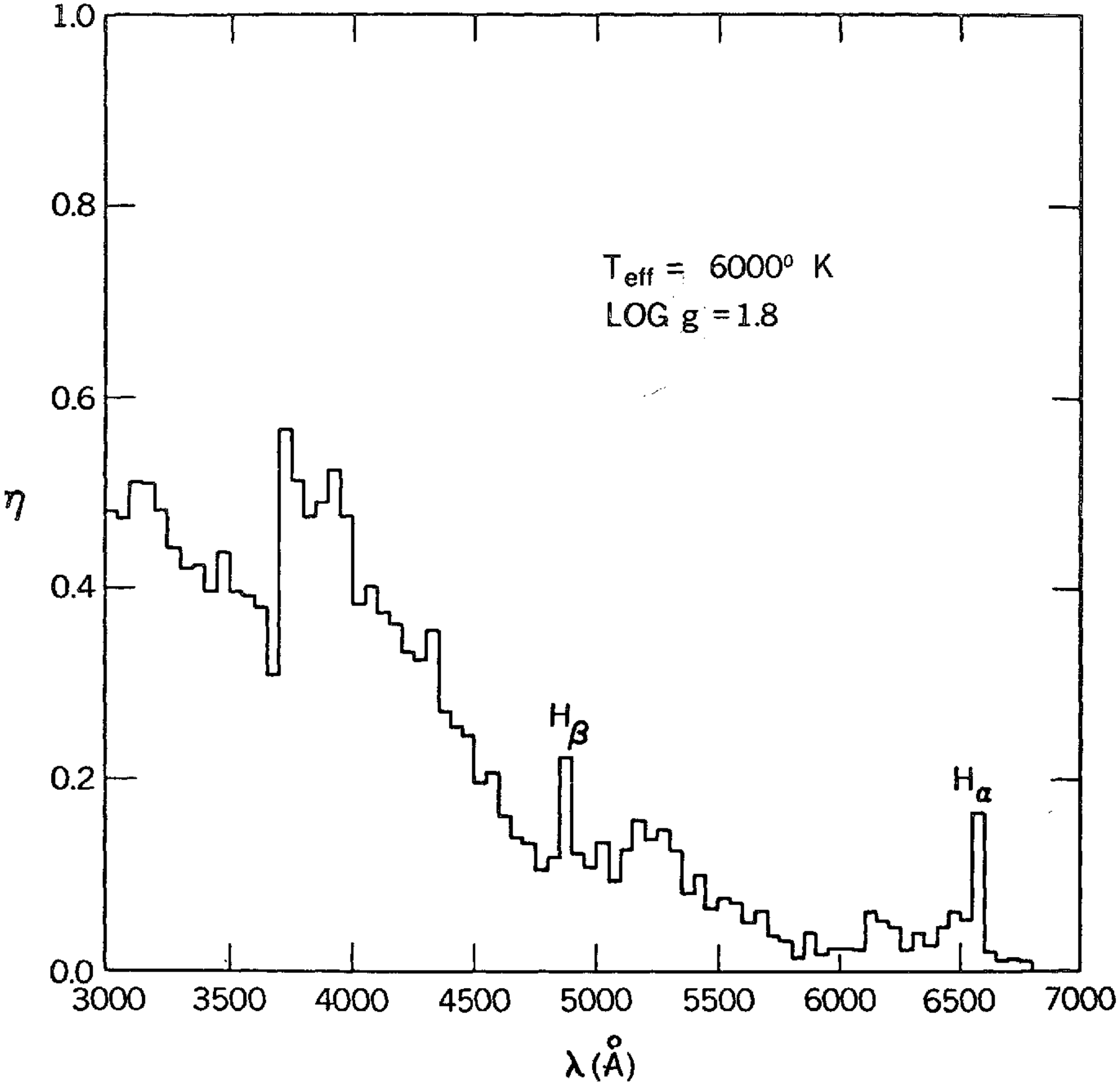

Figure IV-1. Line blocking factors, η, vs. λ for a model with T_{eff} = 6000°K and log g = 1.8.

C-2

Figure IV-2. Spectral energy distribution for a model with T_{eff} = 6000°K and log g = 1.8. --- no line blocking; —— with line blocking. Note linear scale of ordinate.

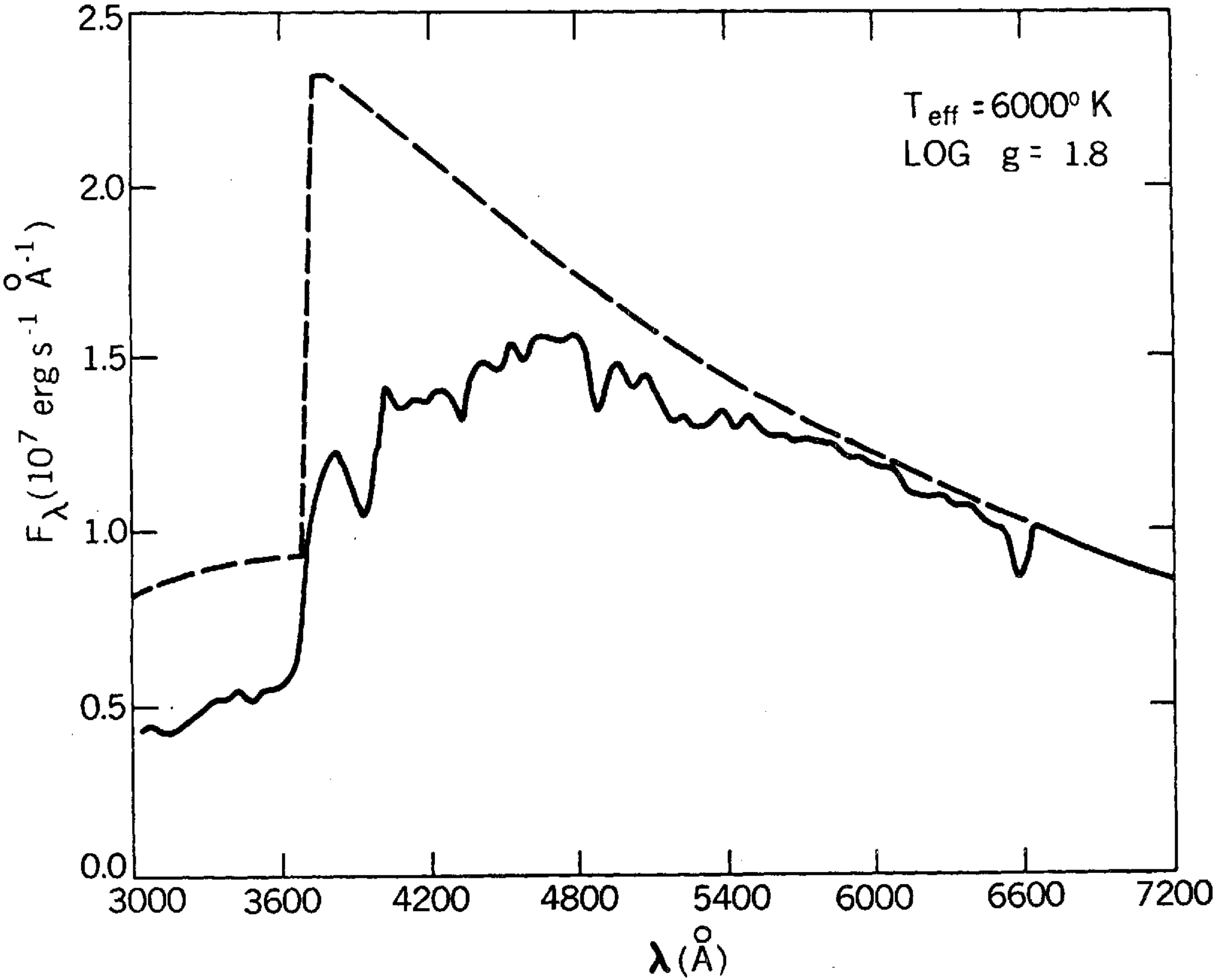
T_eff = 6000° K
LOG g = 1.8
F_λ (10^7 erg s^-1 Å^-1)
2.5
2.0
1.5
1.0
0.5
0.0
3000
3600
4200
4800
5400
6000
6600
7200
λ (Å)

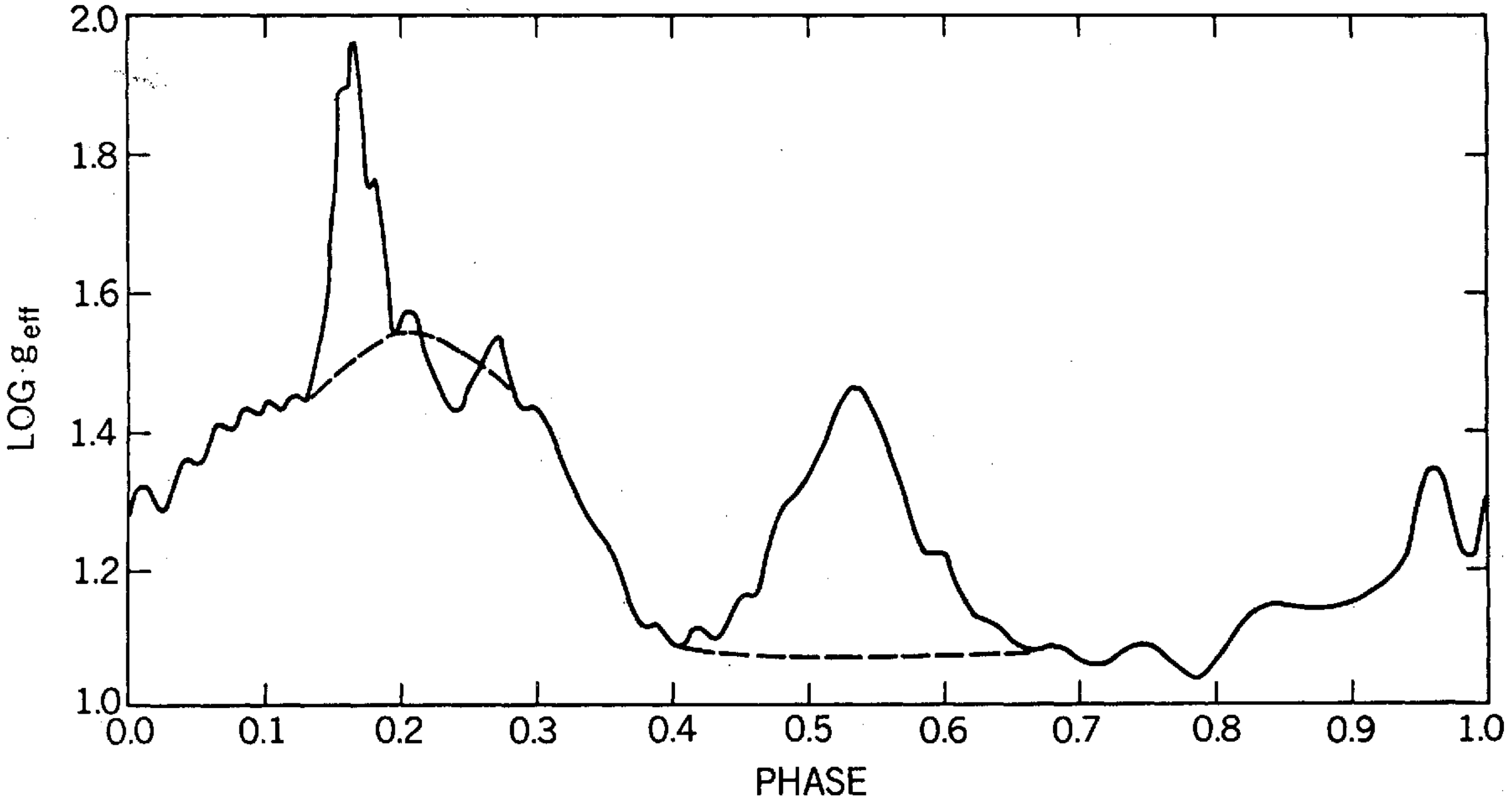

Figure IV-3. log g_{eff} vs. phase. See text for explanation of dashed line.

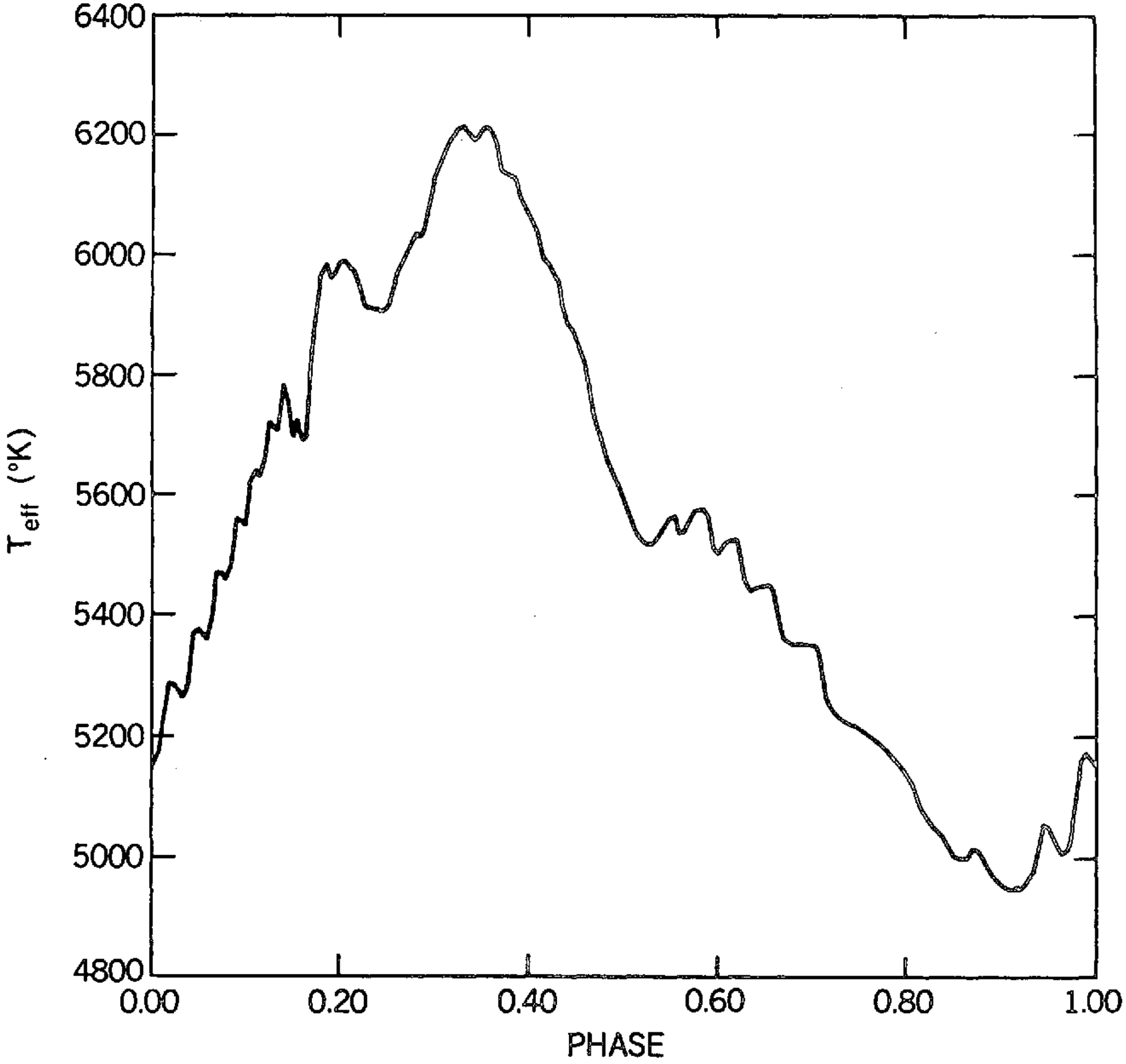

Figure IV-4. log T_{eff} vs. phase. Note decrease in T_{eff} at same phase as increase in g_{eff} near $\Phi = 0.15$

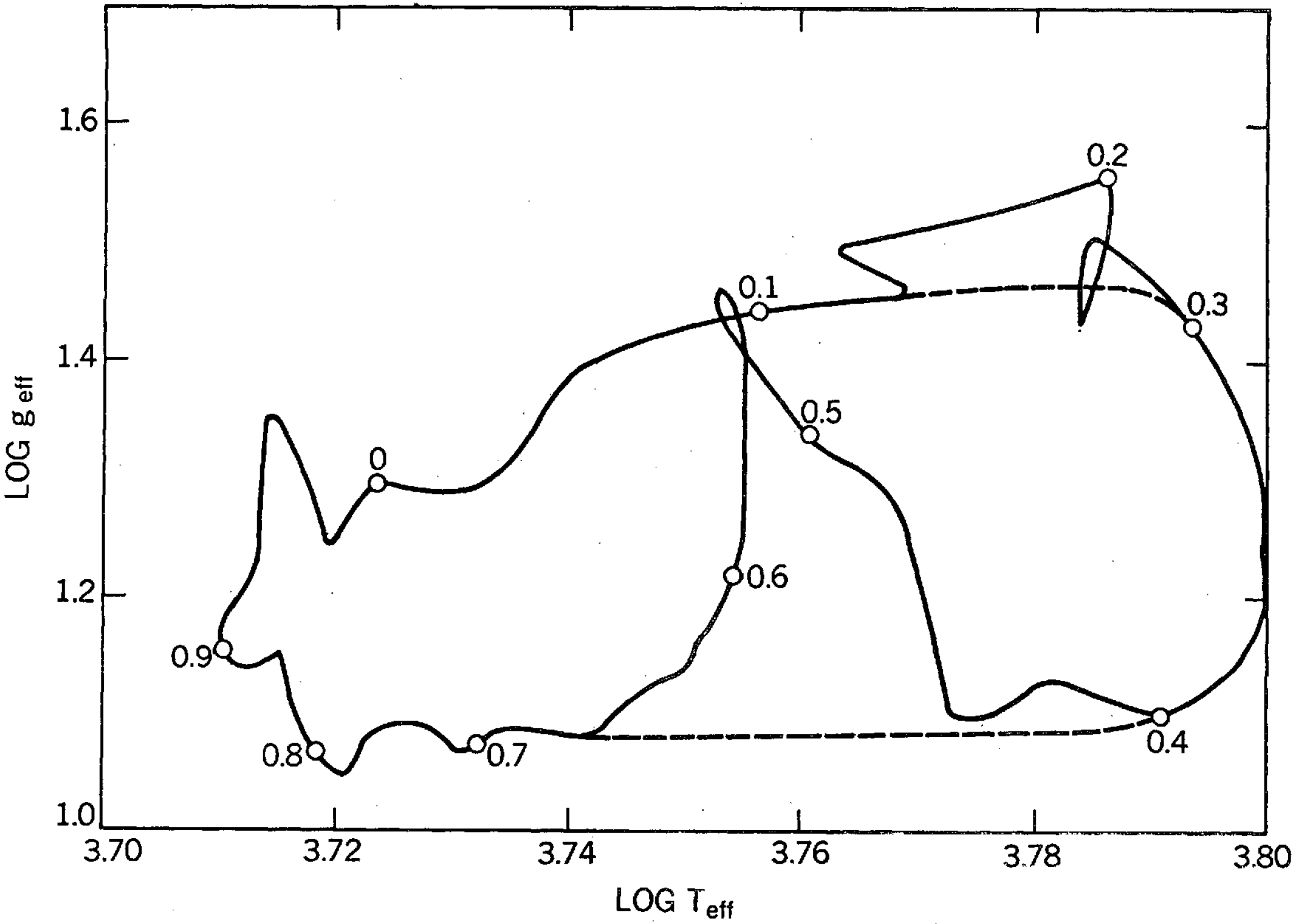

Figure IV-5. log g_{eff} vs. log T_{eff}. Dashed lines show the curve following dashed line in Figure IV-3.

Figure IV-6. P-V diagram constructed using T_{eff} and g_{eff}. The dashed lines in Figure IV-3 has been followed in constructing this curve. The numbers indicate phase.

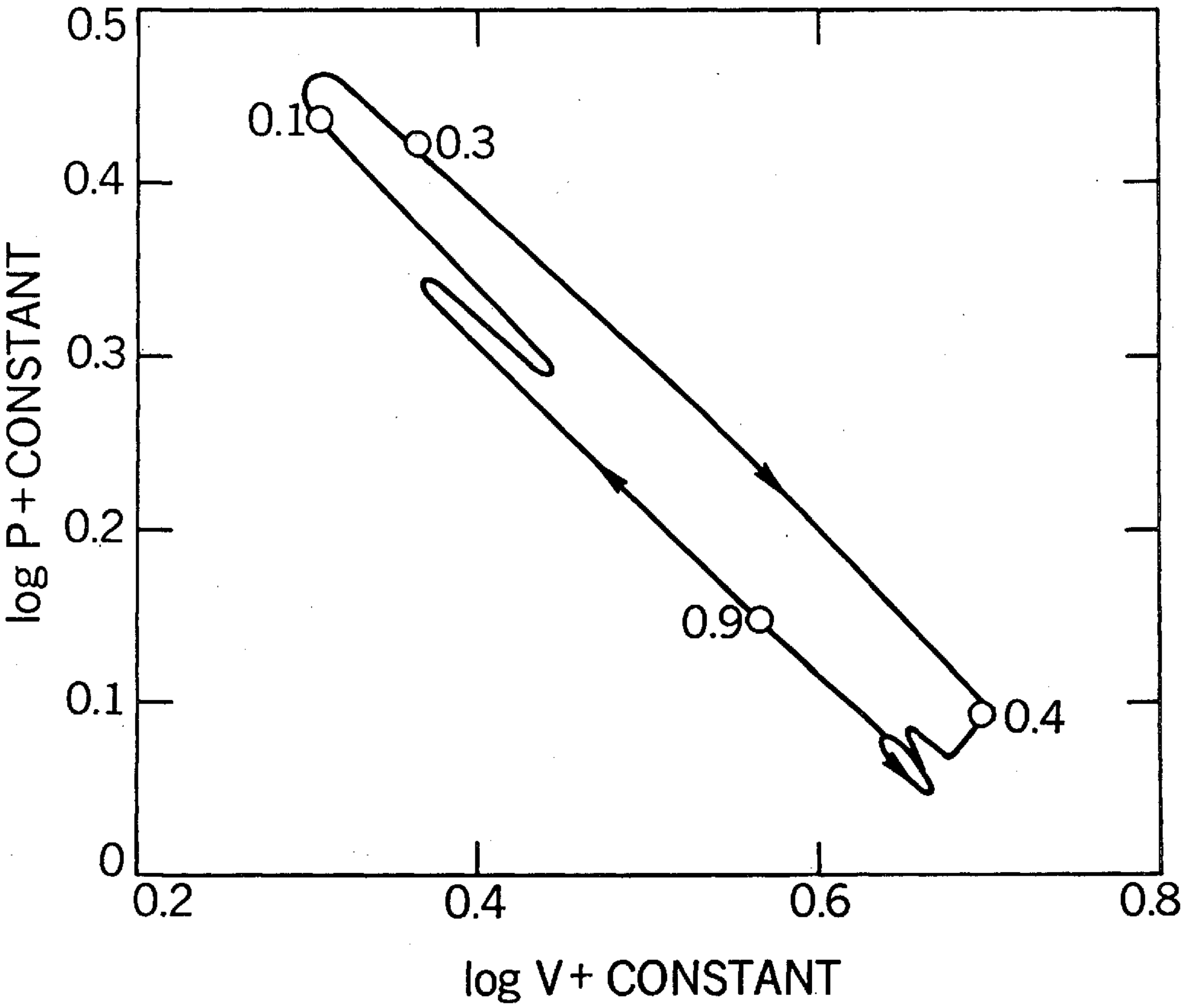
0.5
0.4
0.3
0.2
0.1
0
log P + CONSTANT
0.2
0.4
0.6
0.8
log V + CONSTANT
0.1
0.3
0.9
0.4

Figure IV-7. Absolute visual magnitude, M_V vs. Φ

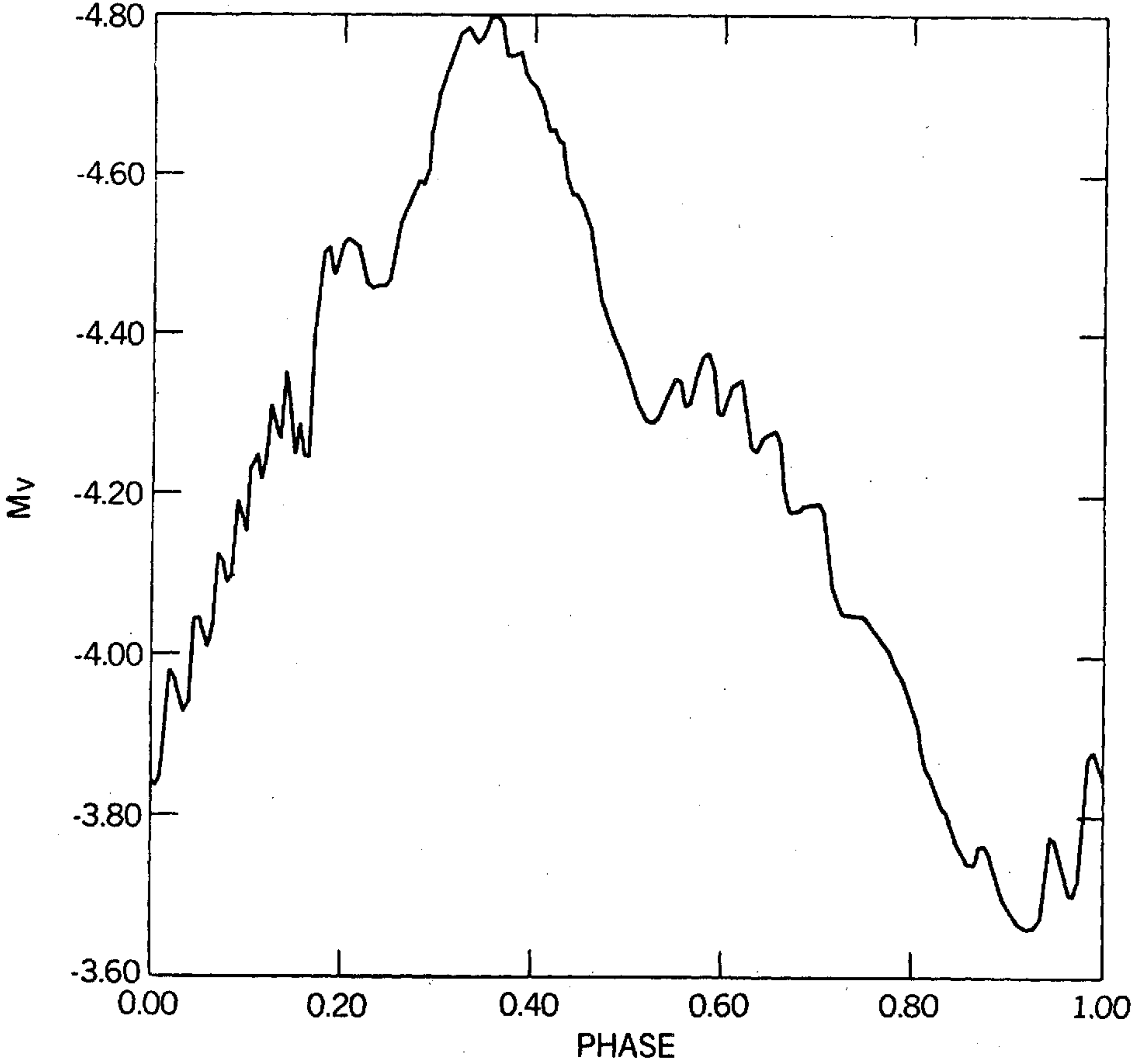
-4.80
-4.60
-4.40
-4.20
-4.00
-3.80
-3.60
M_V
0.00
0.20
0.40
0.60
0.80
1.00
PHASE

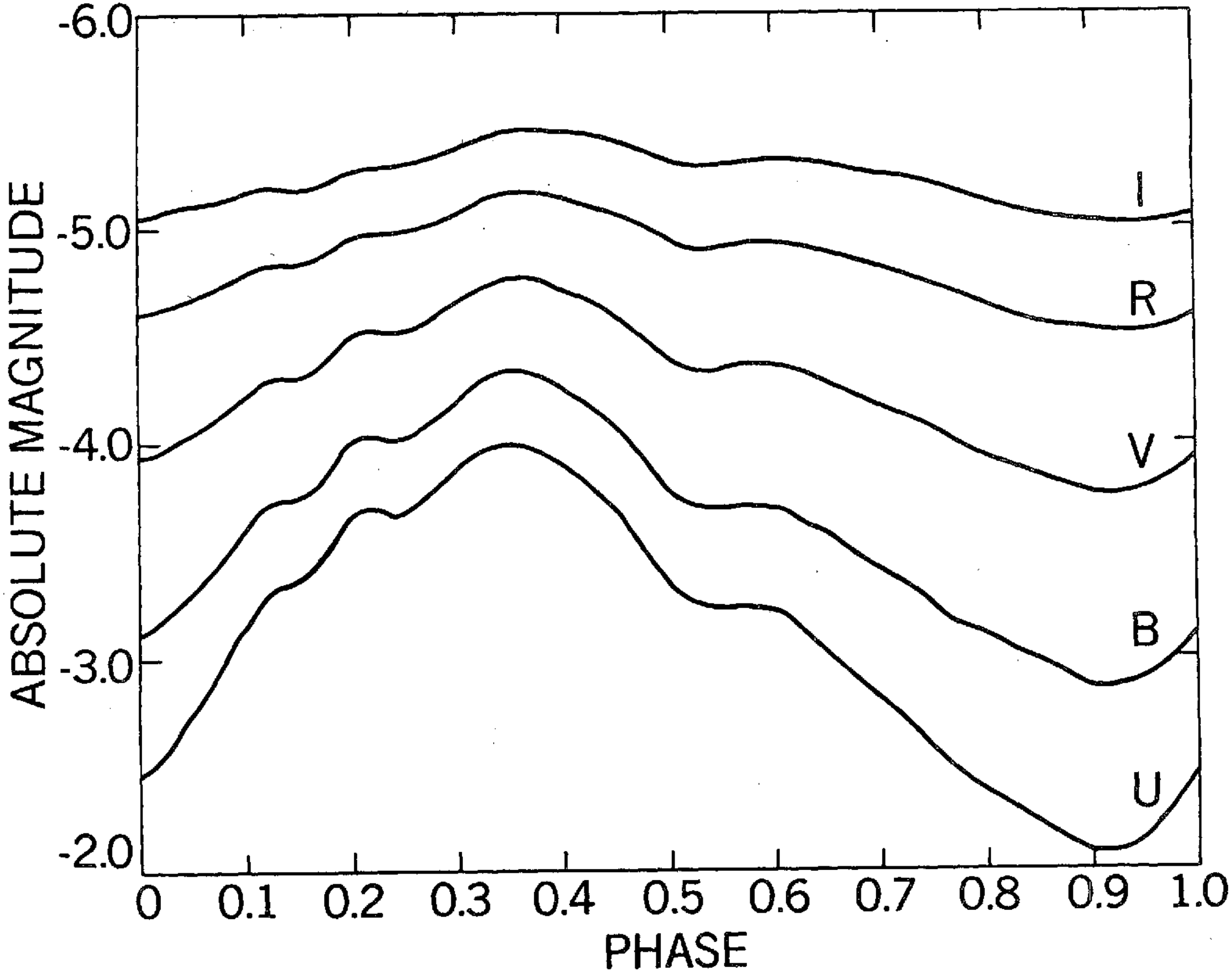

Figure IV-8. Smoothed light curves in U, B, V, R, and I

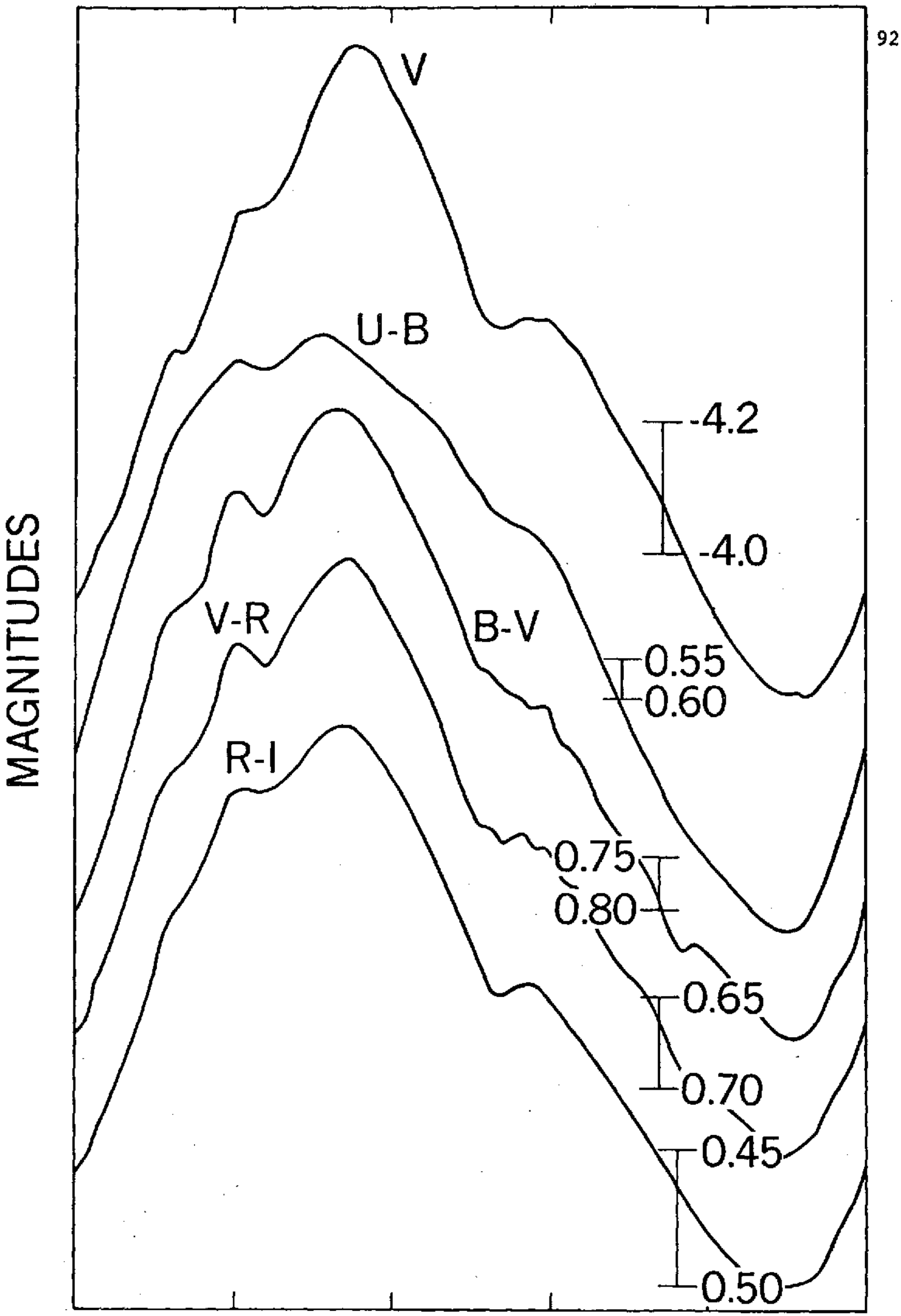

Figure IV-9. Adopted light and color curves for full amplitude model

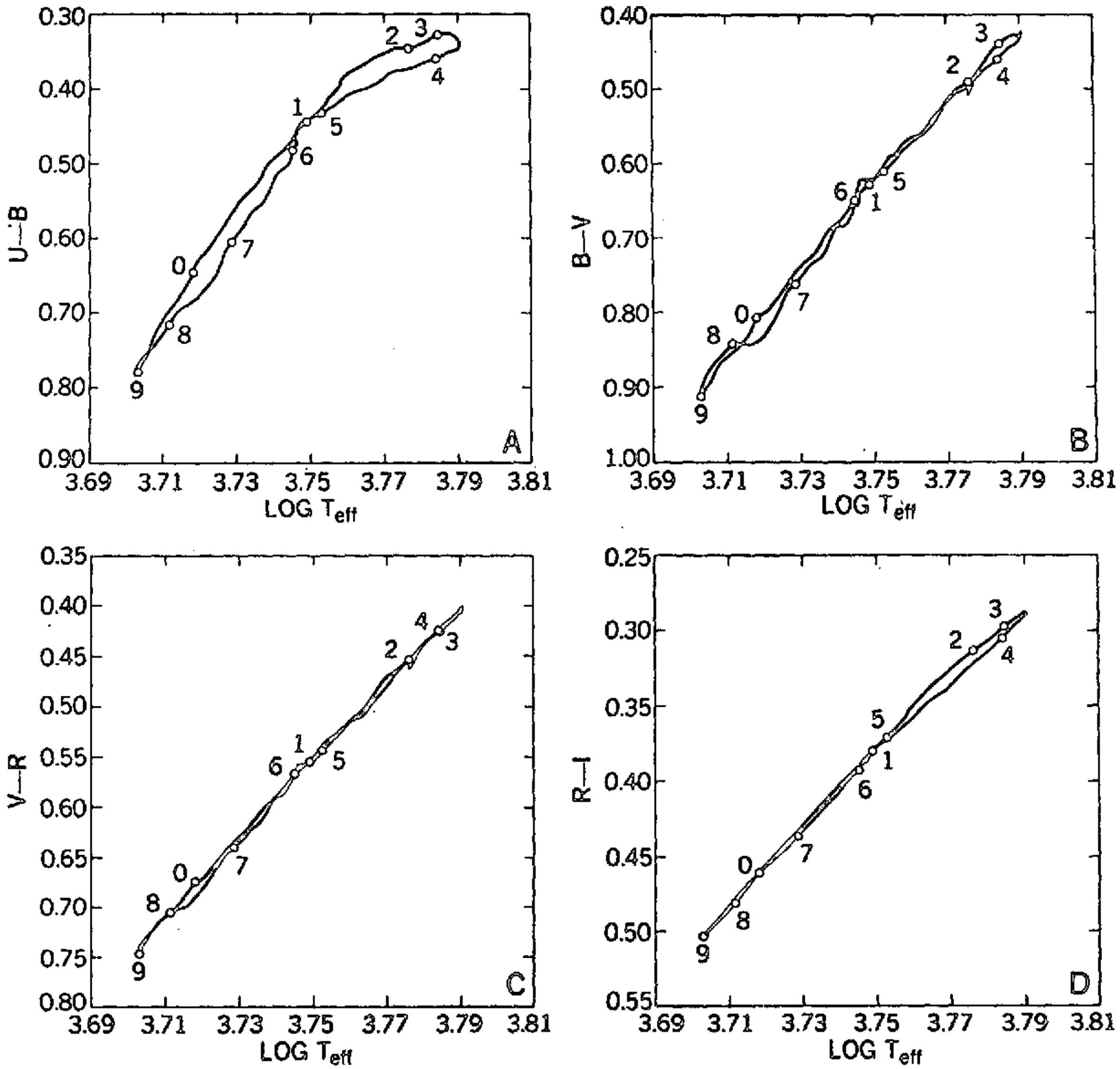

Figure IV-10. (U-B), (B-V), (V-R), and (R-I) vs. log T_{eff}. Numbers indicate phase.

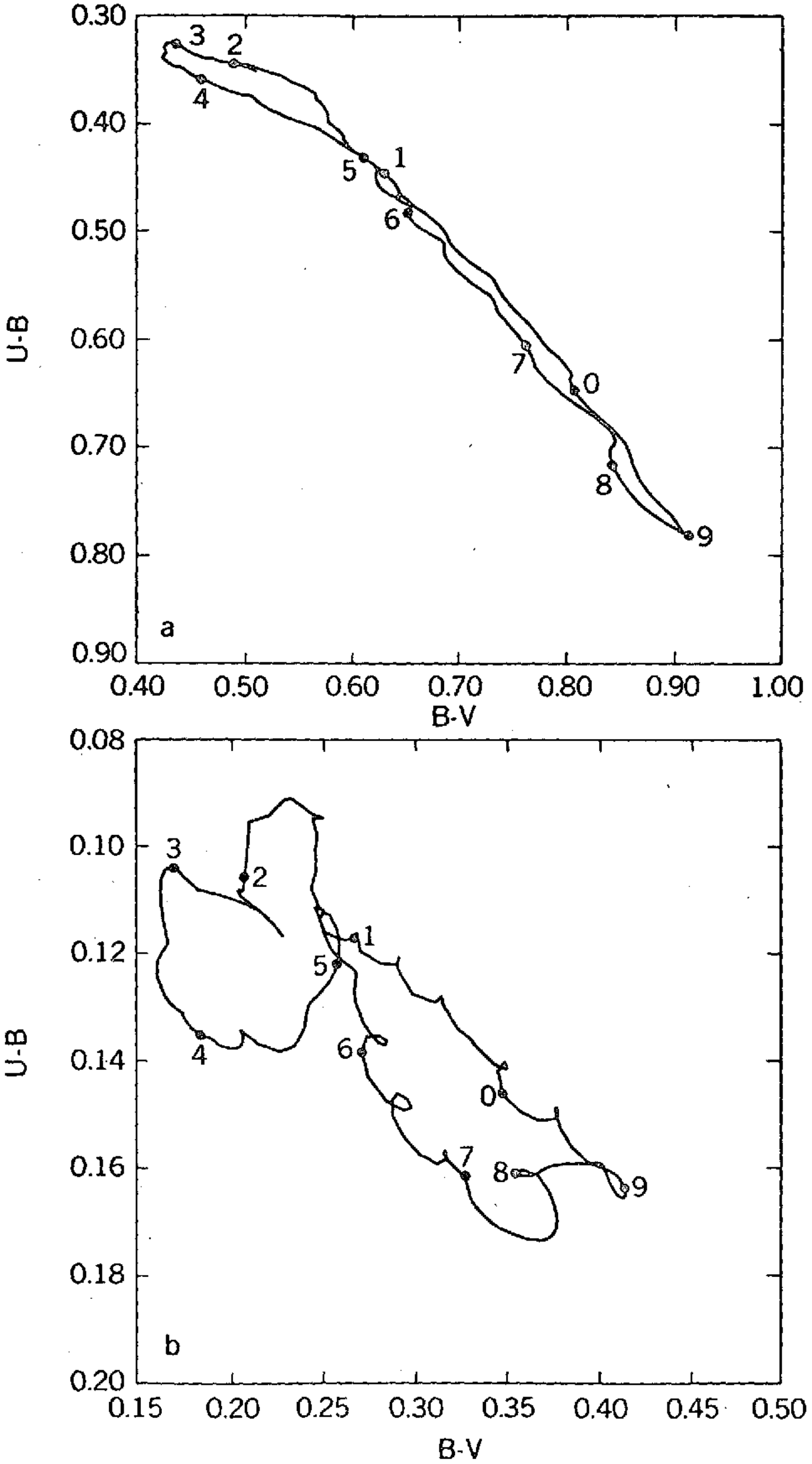

Figure IV-11. a) (U-B) vs. (B-V) including line blocking factors
b) (U-B) vs. (B-V) without line blocking factors
Numbers indicate phase

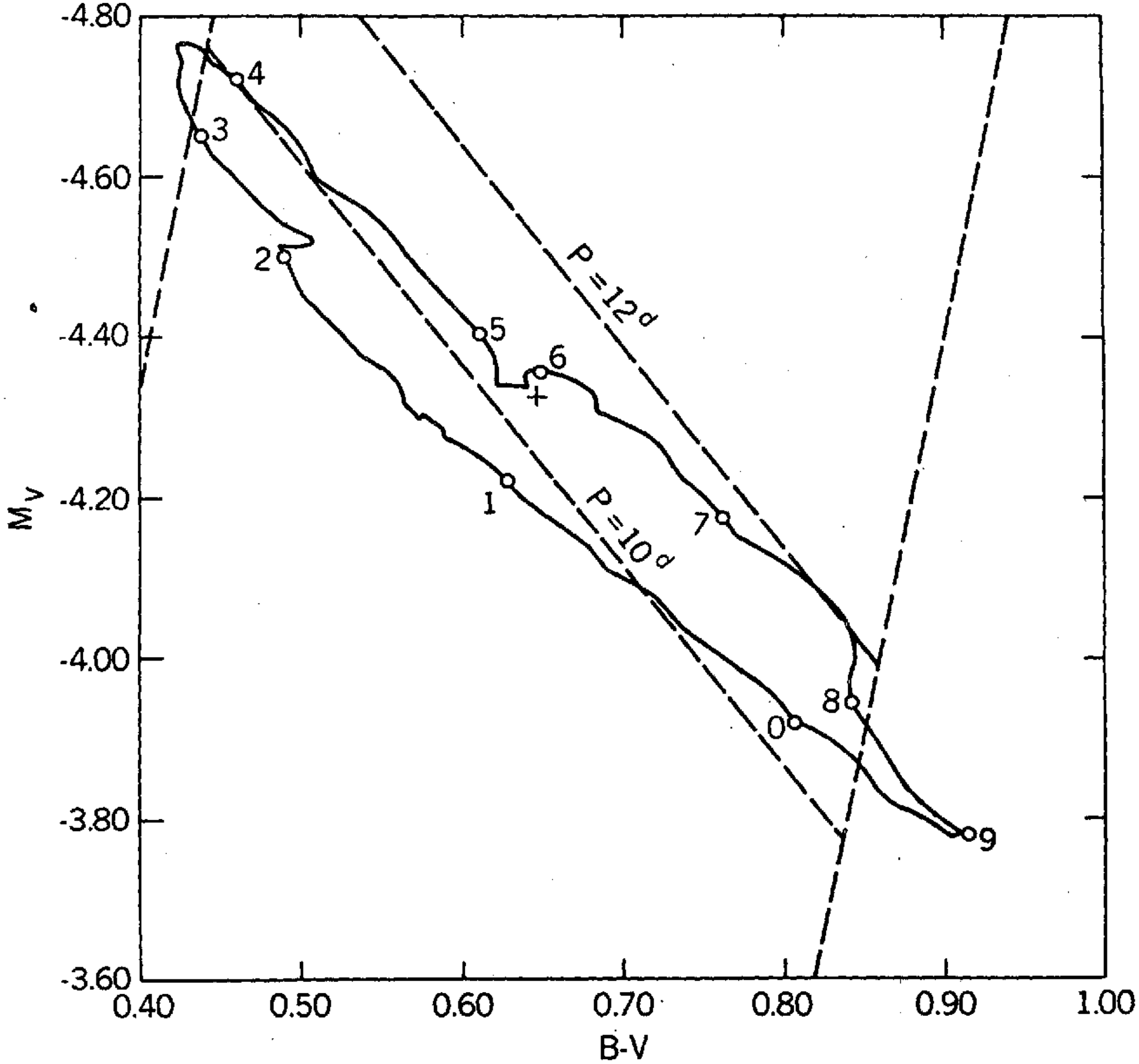

Figure IV-12. Curve traced by the model in the H-R diagram. Dashed lines indicate the Sandage and Tammann instability strip and two lines of constant period. Numbers indicate phase.

CHAPTER V

LINE SPECTRUM

A. Method.

1. Basic approach.

In the preceding chapter it was shown that the broad band colors computed from the hydrodynamic model atmospheres agree with observations of Cepheids. Ideally, one would also like to show that the models reproduce the observed line spectrum. There are several reasons why a detailed comparison was not made. The primary reason is the large amount of computer time required to perform a synthetic spectrum analysis. In addition, the models do not include line blanketing, non-LTE effects, or non-gray radiative transfer, effects that are expected to be more important in the line-forming region than in the photosphere (Bohm-Vitense 1972; Osmer 1972). Since the number of variables that must be changed to investigate the range of observed phenomena is large, a somewhat heuristic approach was adopted. A single line, the λ4494.57Å line of FeI (excitation potential 2.2eV), was chosen to give a reasonable variation of the number of absorbers with depth in the atmosphere. The equivalent oscillator strength, f, was treated as a free parameter. By varying f it was possible to study the effect of the moving atmosphere on lines of different strengths.

2. Computational procedure*

The method for computing line profiles in a moving atmosphere follows a suggestion made by Chandrasekhar (1945). The line

---

*The material in this section is from Karp (1973).

absorption is described by a Voigt profile, $H(a,u)$, where a is the damping parameter and $u = (\lambda-\lambda_0)/\Delta\lambda_D$. When there are velocities in the atmosphere, u must be modified to account for the motions of the gas. This can be done by letting

$$u' = u + \mu v\lambda/c\Delta\lambda_D$$

where μv is the local velocity of the gas projected onto the line of sight, and using $H(a,u')$ to compute the line opacity. The specific intensity can be computed from

$$I_\nu(0,\mu) = \int_0^\infty B_\nu(t_\nu)\exp(-t_\nu/\mu)\ dt_\nu/\mu \ ,$$

and then the flux from

$$F_\nu(0) = 2\int_0^1 I_\nu(0,\ \mu)\mu d\mu$$

Other methods commonly used, such as the Feautrier method or the quadrature integration of Milne's second equation (Kourganoff 1952), cannot be used since the opacity is a function of μ.

B. Microturbulence.

1. Velocity gradient mechanism*

Before considering the detailed line shapes, the equivalent widths of the lines, W, were used to investigate microturbulence in Cepheids. Struve (1932) introduced microturbulence to explain the anomalously large Doppler broadening velocities he found in supergiants. This was explained by Struve and Elvey (1934) as being due to either "a turbulence of small eddies" or to "several shells which expand with different velocities." The concept of microturbulence as a turbulence of small eddies has been attacked by Worrall and Wilson (1972). They claim that the concept of microturbulence is valid only in terms of

---

*The material in this section has been adapted from Karp (1973).

the reversing layer treatment of line formation and attribute the large Doppler broadening velocities to inadequacies in the theory of line formation, particularly the LTE assumption. It has also been suggested by Evans and Schroeder (1972) and Andersen (1973) that systematic errors in the measured equivalent oscillator strengths are responsible for microturbulence. Since neither of the above suggestions has yet been shown to be responsible for the observed microturbulence, there is still a great deal of interest in small scale turbulence. Hearn (1974) has recently shown that the flux of energy required to maintain microturbulence is at least 100 times greater than the acoustic flux generated by convection in the sun. In supergiants the problem is not as bad but the acoustic energy is still a factor of 10 too small to maintain the observed microturbulence even though the acoustic flux is much higher (de Loore 1970).

It has been found that microturbulence varies with height in the atmosphere of supergiants (Wright 1946; Huang and Struve 1960) and with phase in Cepheids (van Paradijs 1972). Differential motions have been reported in the atmospheres of supergiants of many spectral types (Abt 1957; Rosendahl and Wegner 1970; Aydin 1972) and, in particular, in Cepheids (van Hoof and Deurinck 1952; Sanford 1956; Dawe 1969). Van Paradijs has noted that the microturbulence in Cepheids is a maximum near the phase of most rapid contraction. Dawe (1969) and van Hoof and Deurinck (1952) have shown that the velocity gradient is appreciable at this phase. Sanford (1956) has shown that line widths increase just before maximum light in T Mon and SV Vul, a phase at which he observes a large velocity difference between weak and strong lines. The effect of a velocity gradient on the curve of growth has been investigated by Abhyankar (1964 a,b), Kubiowski and Ciurla (1965), Ciurla (1966) and Arakelyan (1969). Although they showed that a velocity gradient raises the flat part of the curve of growth mimicing microturbulence, no attempt was made to compare computed and observed velocity differences. Before investigating the velocity gradient mechanism using the hydrodynamic models, a preliminary study was made.

2. Test of the velocity gradient mechanism.

To make the test case as realistic as possible, a model atmosphere with T_{eff} = 6300°K and log g=1.8 from Parsons (1969) and the FeI line discussed above were used. A wide range of effects was studied by computing curves of growth for log a = -1, -2, -3 and for microturbulent velocities ξ=0 and 5 km sec^{-1} by varying the number of absorbers in the line of sight. These curves are shown in Figures V-1 to V-3. The curves for ξ=0 and ξ=5 km sec^{-1} do not come together at large η/η_0 because the ordinate is $-\log W/\lambda$ instead of $-\log W/\Delta\lambda_D$. Underhill (1947) has shown that a velocity of expansion (or contraction) constant in τ cannot change the equivalent width, W, of a line. Such a velocity field will produce asymmetric profiles, however, due to the integration over the surface. As a check, several profiles were computed with $v(\tau)$ = 20 and 40 km s^{-1}. In no case was the change in W greater than 1 per cent. This change is due to errors in the angle and frequency integration and can be used as a rough estimate of the numerical errors in all these calculations.

For these preliminary calculations, an arbitrary choice of $v(\tau)$ was made, $v(\tau) = -\alpha \log \tau$. This is convenient because it allows a correlation of mean optical depth of formation of a line and its observed radial velocity and is nearly linear with geometric height in the line forming region. An arbitrary constant may be added to $v(\tau)$ without changing W, but it will change the shape of the profile.

The results for $\xi=0$ and 5 km s^{-1} and $\alpha=5$ and 10 km s^{-1} are shown in Figures V-1 to V-3. With $\alpha = 10$ km s^{-1}, the curve of growth ($C_{\alpha 10}$) is nearly identical to the normal curve of growth with $\xi=5$ km s^{-1} ($C_{\xi 5}$) until the damping portion is reached. In all cases $C_{\alpha 10}$ has a wider plateau than $C_{\xi 5}$. An observer would interpret this as being due to a lower value of the damping parameter, a. The decrease in a at phases when ξ is large has been observed by Rodgers and Bell (1964, 1968). This change is a is easily understood. The vertical shift between the damping parts of $C_{\xi 0}$ and $C_{\xi 5}$ is proportional to the ratio of the Doppler widths. Since $C_{\alpha 5}$ and $C_{\alpha 10}$ have the same Doppler width as $C_{\xi 0}$, the three curves must join in the strong line asymptotic limit. The only way this can happen is for $C_{\alpha 10}$ to be below $C_{\xi 5}$ as the lines get strong.

Dawe (1969) has plotted observed velocity versus mean optical depth of formation for weak lines in ℓ Car. Reading from Dawe's Figure 3, the weakest lines which are formed near $\tau = 0.3$ have a velocity of about 18 km s^{-1} while those formed near $\tau = 0.1$ have a velocity of 22 km s^{-1}. Rodgers and Bell (1968) have observed ℓ Car and find that $\xi = 7.5$ km s^{-1} at this phase. If the above results can be extended to this case, $\alpha = 15$ km s^{-1} should be used to correspond to the observed microturbulence which gives $v(0.1) - v(0.3) = 7.2$ km s^{-1}. Correcting for the integration over the surface by the factor $p = v_{puls}/v_{rad} = 1.375$ (Parsons 1971) gives a predicted velocity difference of 5.2 km s^{-1} which, considering the uncertainties involved, is in excellent agreement with the 4 km s^{-1} velocity difference observed by Dawe.

The radial velocities observed from the minima of the computed profiles are given in Table V-1. An exact comparison is not meaningful since the observed velocities and shapes of the lines are more sensitive to the velocity distribution than is the shape of the curve of growth.

3. Microturbulence in the hydrodynamic models.

The hydrodynamic Cepheid atmospheres make it possible to study the velocity gradient mechanism using more realistic velocities than used in the preceding section. The microturbulence was determined for each of 20 models at equal phase intervals, $\Delta\Phi \doteq 0.05$, by performing a differential curve of growth analysis relative to STB. Figure V-4 shows the curves of growth for STB computed by varying log gf for the selected FeI line. After computing similar curves for the 20 hydrodynamic models, the curves were shifted horizontally until their linear parts coincided. The remaining vertical shift is

$$\left[\mathrm{DBV}\right] = \log \frac{\sqrt{v_{\Phi}^{2} + \xi^{2}}}{v_{\mathrm{STB}}} ,$$

where DBV stands for the Doppler broadening velocity, v_{Φ} and v_{STB} are kinetic velocities of Fe atoms in the hydrodynamic and stable models, respectively, and ξ is the unknown microturbulent velocity. If it is assumed that the kinetic temperatures of the two models are in the ratio of their effective temperatures, ξ/v_{STB} can be found. The kinetic velocity in STB was found from $\left[\mathrm{DBV}\right]$ measured in Figure V-4. In Table V-2, which summarizes the results, $\Delta\log W = \mathrm{DBV}$, R_D is the ratio of the Doppler broadening velocities, $v_{\Phi}/v_{\mathrm{STB}}$ is the ratio of the kinetic velocities, and ξ is the microturbulent velocity, and

ΔV is discussed below. All velocities are in km s^{-1}.

It is clear that the velocity gradients are not responsible for all the microturbulence observed in Cepheids. Typical microturbulent velocities in Cepheids are 5 to 10 km s^{-1} (Rodgers and Bell 1964, 1968; Schmidt 1971b; van Paradijs 1972). The latter value is supersonic. They also find that ξ varies with phase with an amplitude of 2 to 5 km s^{-1}. The microturbulence in RDT only has an amplitude of 1 km s^{-1}. Thus, the velocity gradient mechanism cannot explain the variable microturbulence unless more accurate models show that the effect has been underestimated here. However, since ξ rarely exceeds the sound speed by more than 1 or 2 km s^{-1} in Cepheids, the velocity gradient may be responsible for the supersonic part of the microturbulence.

Since it appears that two phenomena contribute to the observed microturbulence, an attempt was made to see how the classical microturbulence, ξ_{cl}, and the microturbulence caused by the velocity gradients, ξ_{gr}, combine to produce the total observed microturbulence, ξ_t. A test case was computed using the model at $\Phi = 0$ including $\xi_{cl} = 2$ km s^{-1} in addition to $\xi_{gr} = 1.4$ km s^{-1}. It was found that $\xi_t = 3.1$ km s^{-1} indicating the Doppler broadening velocity is consistent with

$$\mathrm{DBV} = \sqrt{\frac{2\,kT}{m} + (\xi_{cl} + \xi_{gr})^2} \;.$$

Since the total microturbulence is not the square root of the sum of the squares but is more likely $\xi_t = \xi_{cl} + \xi_{gr}$, even a relatively small ξ_{gr} can make ξ_t appear to be supersonic.

Schmidt (1974) has attempted to correlate the observed microturbulence with the observed velocity difference between weak and strong lines and concludes that there is no apparent correlation. Even when the velocity distribution in the atmosphere is known, as it is in the models, specifying the correct velocity difference, Δ V, for such a correlation is difficult. Since the velocity gradient is not montonic, it is not clear how an average Δ V characteristic of the atmosphere can be found. Figure V-5 shows ξ versus Δ V where Δ V was defined as the maximum minus the minimum velocity on the interval $0.01 < \tau < 1$. The correlation is weak and there is a good deal of scatter, making it unlikely that the correlation could be found observationally. The line shown, a least squares fit to the data, is given by

$$\xi = 0.79 + 0.21 \Delta V .$$

The line does not pass through the origin due to the problem defining Δ V mentioned above.

From this analysis, it appears that microturbulence in Cepheids is still a mystery. The velocity gradient mechanism is not significant in producing the observed microturbulence and may not be large enough to explain the observed variation of the microturbulence with phase. Further work is needed.

C. Line profiles.

1. Asymmetries.

Having computed hydrodynamic model atmospheres makes it possible to compare theoretical and observed line shapes. There are two mechanisms which contribute to the asymmetry of the line profiles.

One of these is a geometric distortion first studied by Chandrasekhar (1945). The observed flux profile is a weighted sum of intensity profiles from different parts of the stellar disk. As illustrated in Figure V-6, each intensity profile is Doppler-shifted by an amount, μv_p, where $\mu = \cos\theta$ and v_p = pulsation velocity of the atmosphere. One such set of intensity profiles is shown in Figure V-7 and illustrates an important computational point. Enough angle points must be included in the angle quadrature to insure sufficient overlap of the intensity profiles. If too few points are used, spurious bumps appear on the flux profile. Expressing the total width of the intensity profile in velocity units, v_D, gives a condition on the maximum angle separation, $\Delta\mu = v_D/v$. Sharper lines and higher velocities require more angle points.

Even a constant velocity in the atmosphere will produce asymmetric line profiles. According to van Hoof and Deurinck (1952) a line will appear symmetric unless

$$\frac{\lambda_0 v}{c} \gtrsim 2.5\,(\Delta\lambda)_N$$

where λ_0 is the rest wavelength of the line; v, the velocity in the atmosphere; and $(\Delta\lambda)_N$, the half width of the undisturbed line. Thus, weak lines will appear more asymmetric than strong lines. Figure V-8 illustrates this point. The weak line, (a), is very asymmetric while the strong line, (b), appears undistorted even though both lines were computed with a constant atmospheric velocity of 20 km s^{-1}. The dashed line in (a) is the bisector of the weak line and is characteristic of lines distorted by this geometric effect.

The second mechanism distorting the line profile is most noticeable in strong lines. Bell and Rodgers(1964) and Kraft (1967) have suggested that the asymmetry of these strong lines is due to velocity gradients in the atmosphere, i.e., different parts of the line are formed in layers of gas moving with different velocities. Figure V-9 illustrates the velocity gradient asymmetry. Not only is this line too strong to show a noticeable geometric distortion, but its bisector has a shape very different from that in Figure V-8(a). The profile in Figure V-9 can be compared to the 4508Å line of FeII in β Dor observed by Bell and Rodgers (1964).

The geometric distortion is expected to be most important at phases of maximum velocity while the distortion of strong lines should be greatest at phases of maximum velocity gradient. In view of the difficulty of determining the velocity gradient from the velocity difference between weak and strong lines, it appears the asymmetry of strong lines is a better indicator of the velocity gradient in the atmosphere.

2. Cheshire cat lines.

Another interesting phenomenon is the occurrence of "Cheshire Cat" (Carroll 1865) lines. This phrase was used by Underhill (see Kraft 1967, pg. 240) to describe the extra component of strong lines often observed in Cepheids. These extra components seem to have no antecedents, but suddenly appear at phases when strong shocks are expected in the atmosphere.

Grenfell and Wallerstein (1969) have attempted to explain the splitting of the H_α line in SV Vul in the following way. The red component of H_α is due to gas falling inward at 70 km s^{-1}, which appears to move a distance of half a stellar radius. The violet component, which has a velocity 40 km s^{-1} more negative than the metal lines, is associated with the pulsation of the atmosphere. When these two layers of gas collide, emission lines of H and He should be observed but are not. Wallerstein (1972) suggests that the inward moving material originates in a circumstellar shell. Skalafuris (1974) suggests a different mechanism based on the work of Whitney (1956), but also asserts that the splitting is due to velocity differences.

Kraft (1967) has stated that the velocity difference between the two components may be as large as 30 to 40 km s^{-1} for the low excitation metal lines while Grenfell and Wallerstein (1969) and Wallerstein (1972) report velocity differences of up to 100 km s^{-1} in the H_α lines of SV Vul and T Mon. Since the atmosphere of RDT never has velocities greater than 30 km s^{-1} or velocity differences greater than 15 km s^{-1}, the occurrence of the "Cheshire Cat" line shown in Figure V-10 indicates a different origin for the secondary component. The deeper component has a velocity of 19 km s^{-1} while the shallower has -3 km s^{-1}, a difference of 22 km s^{-1}. Examining the model shows the maximum velocity difference is 3 km s^{-1} and the mean velocity is 10 km s^{-1}. The splitting of the line is obviously not caused by differential motions.

Further inspection of the model revealed that there was a temperature inversion of about 300°K near $\tau = 3 \times 10^{-3}$, the region in which the line core is formed. To verify that the temperature inversion is responsible for the line doubling, the same line was computed with all velocities set to zero. The result is shown in Figure V-11. The central reversal is characteristic of a line core formed in a region in which the source function increases outward. While a more detailed, non-LTE calculation would probably not show as large a central reversal since the source function in the line core could be smaller than the Planck function, the line doubling could still occur for the strongest lines. In fact, Thomas suggested that a temperature inversion was responsible for the "Cheshire Cat" lines (see Kraft 1967, pg. 239). The asymmetry of the line core can be caused by purely geometric effects as illustrated in Figure V-12. This profile was computed with a constant velocity of expansion of 10 km s^{-1}. This profile is nearly identical to that in Figure V-10 except for the direction of the asymmetry caused by the different signs of the velocities used in the two cases.

It is now possible to explain why the "Cheshire Cat" lines in H_α and CaII K are displaced more from the primary component than those of the metal lines. Since the temperature inversions in RDT occur only above $\tau = 0.01$, only the part of the line formed above this point in the atmosphere can show the central reversal. A large part of H_α is formed in this region, and, therefore, the velocity difference between the two components will be greater than that of the metal lines.

Although the models are inadequate for computing profiles of strong lines, H_α profiles were computed for a qualitative comparison with observations. No attempt was made to accurately reproduce the observed line shapes. In fact, the H_α lines shown in Figure V-13 were calculated using a Voigt profile instead of the more accurate Stark broadening. The lines have flat bottoms because the models do not extend to small enough optical depths and because of the LTE source function used. Qualitatively, though, the agreement with the

H_α profiles published by Grenfell and Wallerstein (1969), Wallerstein (1972), Rodgers and Bell (1968), and Schmidt (1970) is excellent. While some of the irregularities in the profiles are associated with temperature fluctuations caused by zoning effects, several of the profiles indicate the presence of temperature inversions. In particular, the profile at $\Phi = 0.55$ shows the effect of the shock wave that produces the second bump on the light and velocity curves.

One of the problems associated with "Cheshire Cat" lines is the threshold effect (Skalafuris 1974). In Cepheids the line splitting occurs only for the strongest lines, while in W Vir and RR Lyr stars the line doubling often occurs in weaker lines. If the splitting is caused by temperature inversions, two phenomena contribute to the threshold effect. First, as a pressure wave moves outward, it encounters a decreasing density. Conservation of mass requires that the wave must accelerate. Thus, the strongest shocks occur highest in the atmosphere. The energy dissipation at the shock front produces a temperature rise. Second, as shown in Chapter II, the time it takes an element of gas to return to radiative equilibrium following a perturbation increases as the optical depth decreases. In the region where the weak lines are formed, the gas requires only a few seconds to return to equilibrium, while higher in the atmosphere where the cores of the strong lines are formed, the time it takes the gas to return to equilibrium can be several thousand seconds (Whitney 1967). In this time the shock will have travelled about half a pressure scale height and crossed several zones in the model producing a reasonably thick layer with an elevated temperature. The splitting of weak lines in population II variables is, then, indicative of shocks in their photospheres.

The temperature structure of the shock front will be modified by the use of an artificial viscosity pressure, though. Instead of having a temperature discontinuity at the shock front, the temperature rise will be spread out over 3 or 4 zones. However, ignoring the effects of radiation from the heated gas at the shock front, the total temperature rise across the shock should be the same whether or not artificial viscosity is used (Richtmeyer and Morton 1967). If radiation effects are included, the error in the temperature rise depends on the ratio of two characteristic times. If the time it takes the gas to return to thermal equilibrium, t_R, is shorter than the time it takes the shock to move a distance equal to its thickness, t_s, then using artificial viscosity will lead to an underestimate of the temperature rise. If, on the other hand, $t_R > t_s$, the temperature rise across the shock front will be independent of the artificial viscosity. In the region of interest in RDT $t_R \sim 5000$ sec, and the thickness of the shock is 3 or 4 zones, $\Delta X = 5 \times 10^9$ cm. If the shock moves at roughly the sound speed of 10 km s^{-1}, then $t_R \approx t_s$. The temperature inversions in RDT are, therefore, underestimates. This error is unimportant, though, since the assumptions made in computing the atmospheric structure are not completely valid in the region where the shocks occur.

Care must be taken when measuring velocities of strong lines. The practice of treating each component of the line as a distinct layer of gas produces erroneous velocity curves. Neither component represents the motion of the atmosphere. Even if the splitting is not observed and the line core appears to be symmetric, there may be incipient splitting that has been masked by macroturbulence, microturbulence, or instrumental broadening. Velocities of strong lines should, therefore, be measured at some point in the wings of the line. This point will be discussed further in the next section in which the velocity curves are discussed.

D. Velocity curves.

1. Ratio of pulsational to radial velocity.

In order to interpret radial velocities obtained from measurements of spectral lines, the center to limb variations of the specific intensity must be taken into account. In effect, the center to limb variations reduce to a determination of p, the ratio of the pulsation velocity of the atmosphere, v_p, to the measured radial velocity of the line, v_r. The value of p differs from 1 because the observed flux profile is a weighted sum of intensity profiles with different line of sight velocities. (See Figure V-6).

The early attempts at calculating p (Shapley and Nicholson 1919; Carroll 1928; Getting 1935; van Hoof and Deurinck 1952) all made the assumption, either implicitly or explicitly, that the Doppler shift of the line was less than the line's Doppler width. This assumption is not always valid in Cepheids since the lines are typically 5 to 10 km s^{-1} wide while the pulsation amplitude is of the order of 20 to 30 km s^{-1}. In effect, the assumption reduces to the statement that the minimum of the flux profile is simply the weighted average of the minima of the intensity profiles from $\mu = 1$ to $\mu = 0$. In the case shown in Figure V-7, it is clear that intensity profiles from $\mu < 0.4$ have little effect on the location of the flux minimum. If the limb darkening law is given by

$$\frac{I(\mu)}{I(1)} = (1-\beta) + \beta\mu \qquad \text{(V-1)}$$

this assumption leads to

$$p = \frac{6 - 2\beta}{4 - \beta} \qquad \text{(V-2)}$$

Since equation (V-2) gives $\frac{24}{16} \leq p \leq \frac{24}{18}$ for $0 \leq \beta \leq 1$, several investigations have concluded that the calibration of p has only a small effect on the computed velocities. Since the basic assumption used to calculate equation (V-2) is not valid for Cepheids, Parsons (1972) recalibrated p and showed that p is a function of γ, the ratio of the velocity of the atmosphere, v_p, to the observed width of the line including instrumental broadening $v_{\frac{1}{2}}$. Since RDT differs from the models used by Parsons, a similar calculation was performed.

Three models were selected for the study, STB, $\Phi = 0.2$, and $\Phi = 0.7$, corresponding to mean, minimum, and maximum radius, respectively. For each model, p was computed for a set of velocities and values of log gf. The effect of instrumental broadening was included by convolving each profile with a Gaussian slit function 0.04Å wide, while rotation and macroturbulence were included by convolving the profiles with the rotation broadening function given by Huang and Struve (1960) with v sin i = 10 km s^{-1}. Although Kraft (1966) has concluded that Cepheids probably do not rotate, Abt (1958) has shown that this rotation cannot be distinguished from a macroturbulence of 7 km s^{-1}, a value characteristic of Cepheids. The bisector of each profile was constructed and used to determine the velocity at the minimum, half intensity, and 1/e points of the profile. A total of 864 values of p was determined having an average of $p = 1.31 \pm 0.03$. The value of p was found to be insensitive to the model, changing by only 0.02 between the models at minimum and maximum radius. If only those cases with line widths of 7 km s^{-1} are considered, the average $p = 1.30 \pm 0.02$. Since most Cepheids have line widths of this order, a constant value, $p = 1.30$, was adopted. The error in p introduces only a 2% error in the velocity.

Although a constant value of p was adopted, Figure V-14 shows some interesting correlations. The abscissae are $\gamma = v/v_{\frac{1}{2}}$ and the ordinates p. In all four graphs, the dashed lines are given by $p = 1.37 - 0.03\gamma$ taken from Parsons (1972). Figures (a) and (b) show $p(\gamma)$ for a weak and strong line, respectively, measured at the minimum of the profile while (c) and (d) represent the same lines measured at the half intensity points. In both cases, the strong line has a weaker dependence on γ than the weak line. In addition, when the velocity is measured at the half intensity point, p is nearly independent of γ. The near constancy of p when the velocities are measured at the half intensity point combined with the problem of incipient splitting of the cores of the strong lines indicates that the half intensity point should be used to determine velocities. In particular, the practice of using the line core when it is symmetric and the wings when the core is distorted will produce spurious scatter in the velocity curves.

2. Comparison of hydrodynamic and line profile velocity curves.

If the line core cannot be used to find the velocity of the upper atmosphere, the problem of detecting velocity gradients becomes more difficult. Figure V-15 shows how a velocity characteristic of the line core can be found. The dashed lines are extensions of the wings from points near the line core. The velocity determined from the point of intersection of the extrapolated wings agrees with the velocity of the upper layers of the model with an accuracy of about 10%. In the example shown with $p = 1.30$, the predicted value is 14.5 km s^{-1}, while the model gives 13 km s^{-1} for the region in which the line core is formed.

The easiest way to compare the velocities of the models with the velocities determined from the profiles is to compare velocity curves. Figure V-16 shows the velocity curves for a weak, intermediate, and strong line represented by a dashed, solid, and dot-dashed line, respectively. To make the comparison as representative as possible these velocities were measured at the minimum of the unconvolved profiles. The arrows indicate phases at which the strong line has a split core. Only the deeper component was measured leading to the deviations from the other velocity curves. The open circles show the velocity of H_α determined by the extrapolation of the line wings discussed above. A comparison with Figure III-7 indicates that measurements of the line profiles underestimate the velocity differences between the optically thin and optically thick layers. This result is not surprising since the line profiles represent averages over a range of continuum optical depths. Note, however, that the phase shift between H_α and the metal lines near $\Phi = 0.5$ is nearly the same as the phase shift between $\tau = 10^{-3}$ and $\tau = 0.1$ at the same phase. In addition, the feature on the velocity curve near $\Phi = 0.2$ can be seen only for the strongest lines in agreement with Figure III-7.

3. Center of mass velocity.

One of the problems facing an observer studying Cepheids is the determination of the center of mass velocity of the star, v_0. This value is needed both for kinematic studies (Kraft and Schmidt 1963; Wielen 1974) and for determining the radius of the star using the Wesselink (1946) method. Oke, Giver, and Searle (1962) have estimated that an error of 1 km s^{-1} in v_0 results in an error of 10% in the derived radius.

The center of mass velocity is normally defined by finding v_0 such that

$$\int_0^P (v-v_0)dt=0 \ . \qquad \text{(V-3)}$$

Due to changes in the opacity scale during the pulsation, the velocity curves do not follow a given element of gas. There is no guarantee, therefore, that a strict application of Equation (V-3) will give an accurate value of v_0.

In order to check the importance of this effect, velocity curves for a number of cases were constructed, and Equation (V-3) was used to find v_0. Table V-3 summarizes the results. In this table, MIN, ½, 1/e refer to the part of the profile used to find the velocity; N, G, R, B refer to the unconvolved profile, convolved with a Gaussian slit 0.04Å wide, convolved with a rotation broadening function corresponding to v sin i = 10 km s^{-1}, and convolved with both broadening functions, respectively. The weakest lines were completely washed out by the rotation broadening function and these cases are omitted from the table. The velocity curves determined from the minima of the strong lines have also been omitted due to splitting of the line core. It can be seen that v_0 can be found to an accuracy of better than ± 0.4 km s^{-1} by using Equation (V-3). While this error will introduce a 4% error in the radius determination, it is rare that observations can be made to this accuracy.

Inspection of these velocity curves reveals only small differences among them. The adopted curve, Figure V-17, represents a typical velocity curve. The line used is moderately strong, varying from an equivalent width W = 88 mÅ to W = 153 mÅ. A macroturbulence of 7 km s^{-1} has been assumed and the resultant profile was convolved with a Gaussian slit corresponding to 2 Å / mm. In view of the discussion earlier in this chapter, the velocity was measured at the half intensity point on the profile. This velocity curve has been adopted as representative of the observed velocity curves of the metal lines and will be the only one used in the next chapter.

Table V-1

Radial velocity in km s^{-1} observed from computed profiles

log a	-1	-1	-2	-2	-3	-3
α(km s^{-1})	5	10	5	10	5	10
log η/η_0						
-1.000	2.9	5.4	3.3	5.4	2.1	5.4
0.204	5.4	6.6	5.4	9.3	4.2	9.3
1.408	6.7	13.3	6.6	14.7	6.6	14.7
2.612	10.8	14.7	9.3	14.7	6.6	14.7

Table V-2

Microturbulent velocities in hydrodynamic model

Φ	Δ log W	R_D	v_Φ/v_{STB}	ξ/v_{STB}	ξ	Δ V
.00	.12	1.32	0.97	0.88	1.39	3.6
.05	.10	1.26	0.99	0.77	1.22	1.6
.10	.06	1.15	1.01	0.56	0.89	1.2
.15	.20	1.58	1.02	1.22	1.93	5.8
.20	.16	1.45	1.05	1.03	1.63	4.7
.25	.08	1.20	1.05	0.62	0.98	0.8
.30	.14	1.38	1.05	0.92	1.46	2.1
.35	.14	1.38	1.06	0.92	1.46	2.0
.40	.10	1.26	1.05	0.73	1.16	1.0
.45	.12	1.32	1.04	0.84	1.33	2.4
.50	.18	1.51	1.02	1.12	1.77	3.8
.55	.08	1.20	1.01	0.66	1.04	1.6
.60	.20	1.58	1.01	1.22	1.93	3.7
.65	.08	1.20	0.99	0.67	1.06	1.6
.70	.04	1.10	0.98	0.48	0.76	0.7
.75	.06	1.15	0.97	0.59	0.93	1.0
.80	.08	1.20	0.97	0.69	1.09	1.4
.85	.08	1.20	0.96	0.69	1.09	2.3
.90	.06	1.15	0.96	0.60	0.95	0.4
.95	.08	1.20	0.96	0.69	1.09	2.3

Table V-3

Error in center of mass velocity (km $\sec^{-1}$)

	MIN				½				1/e			
log gf	N	C	R	B	N	C	R	B	N	C	R	B
-4	0.2	0.4	—	—	0.4	0.4	—	—	0.2	0.2	—	—
-3	0.0	0.3	—	—	0.4	0.3	—	—	0.4	0.3	—	—
-2	0.1	0.1	0.0	0.0	0.1	0.1	0.1	-0.2	0.1	0.0	0.0	0.0
-1	0.4	0.0	-0.2	-0.2	-0.2	-0.2	-0.2	-0.2	-0.3	-0.2	-0.2	-0.2
0	—	—	—	—	0.1	0.1	0.1	0.1	0.1	0.1	0.1	0.1
1	—	—	—	—	0.1	0.1	0.1	0.1	0.1	0.0	0.0	0.0

Figure V-1. Curves of growth for log a = -1. — . —— .——, $\xi = 0$ ($C_{\xi 0}$); ————————, $\xi = 5$ km s^{-1} ($C_{\xi 5}$); ○————————○, $\alpha = 5$ km s^{-1} ($C_{\alpha 5}$); ●————————●, $\alpha = 10$ km s^{-1} ($C_{\alpha 10}$). ξ is the microturbulent velocity and α is the velocity gradient parameter.

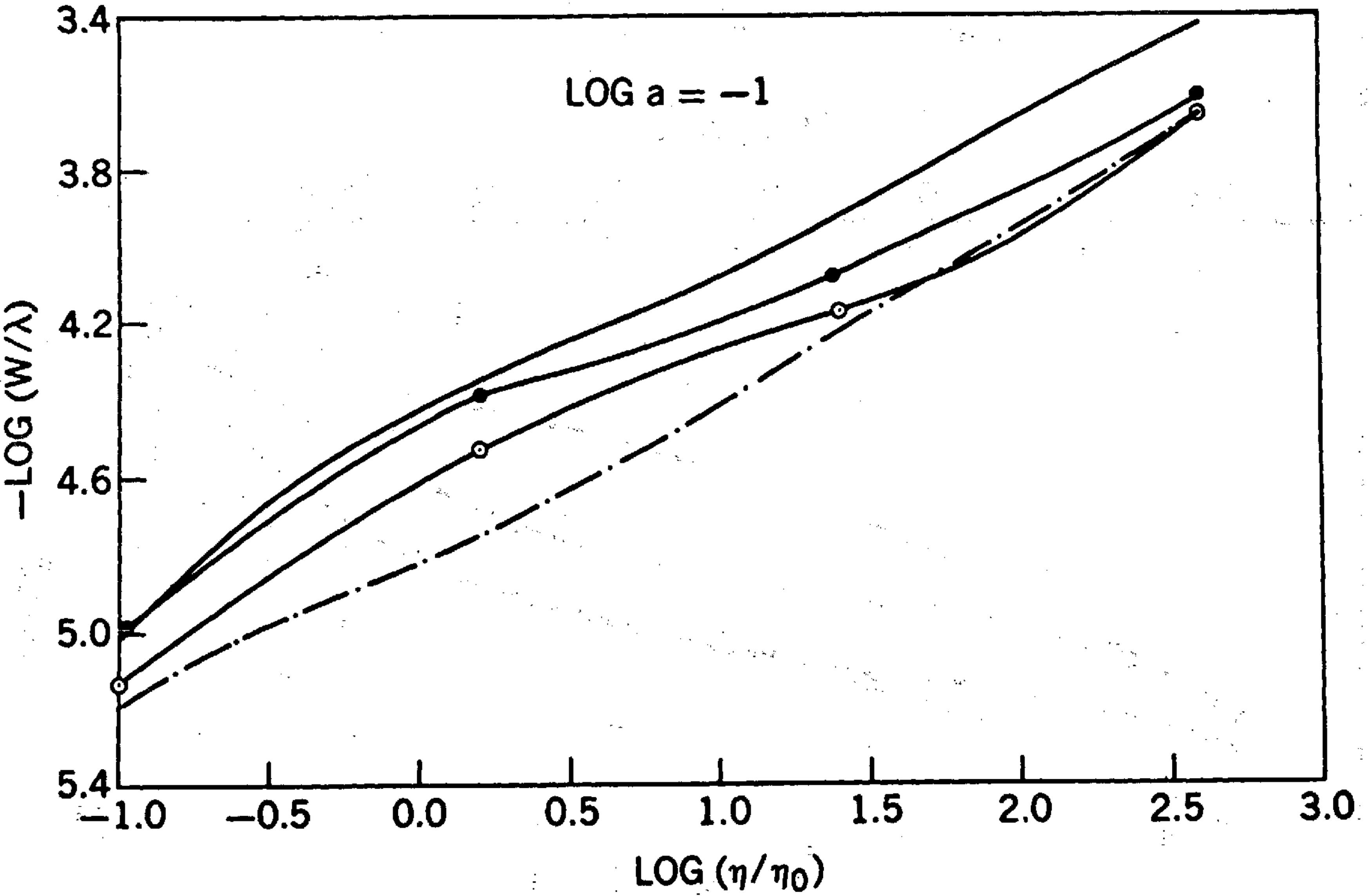
LOG a = −1
3.4
3.8
4.2
4.6
5.0
5.4
−LOG (W/λ)
−1.0
−0.5
0.0
0.5
1.0
1.5
2.0
2.5
3.0
LOG (η/η0)

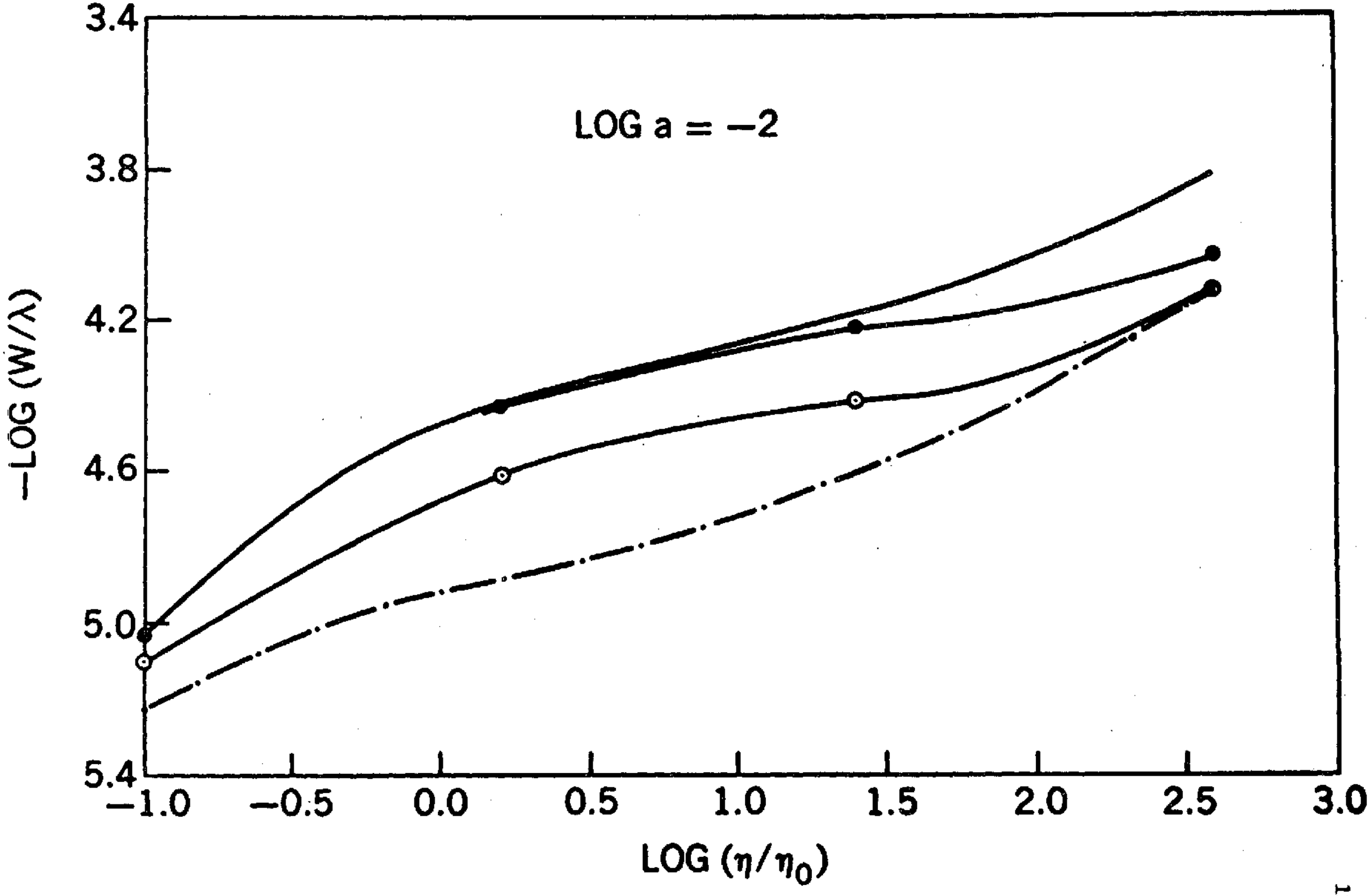

Figure V-2. Curves of growth for log a = -2. Notation is the same as in Figure 1.

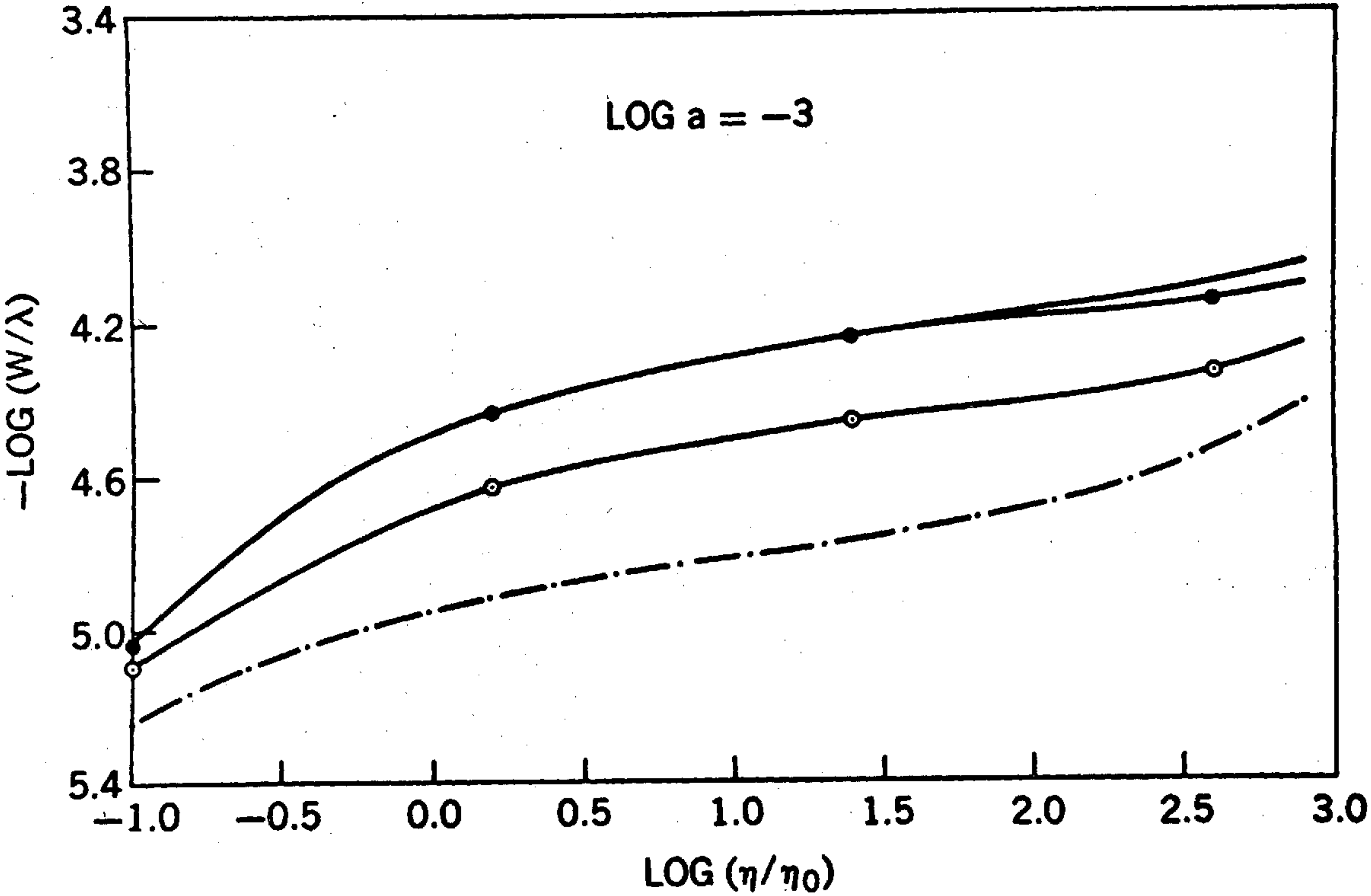

Figure V-3. Curves of growth for log a = -3. Notation is the same as in Figure 1.

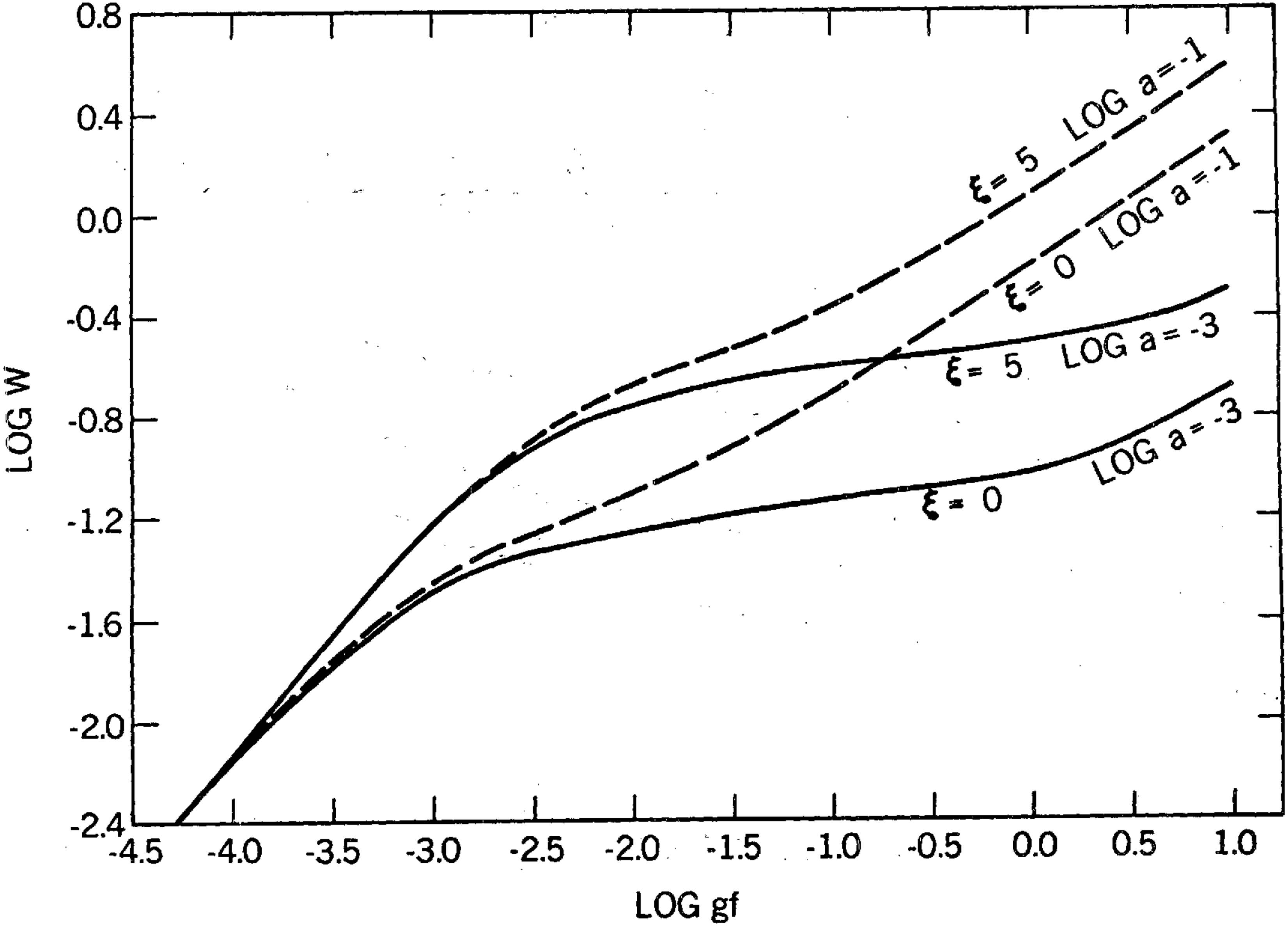

Figure V-4. Curves of growth computed using the equilibrium model

Figure V-5. Microturbulent velocity, ξ, vs. a measure of the velocity gradient, ΔV. The least squares line is shown.

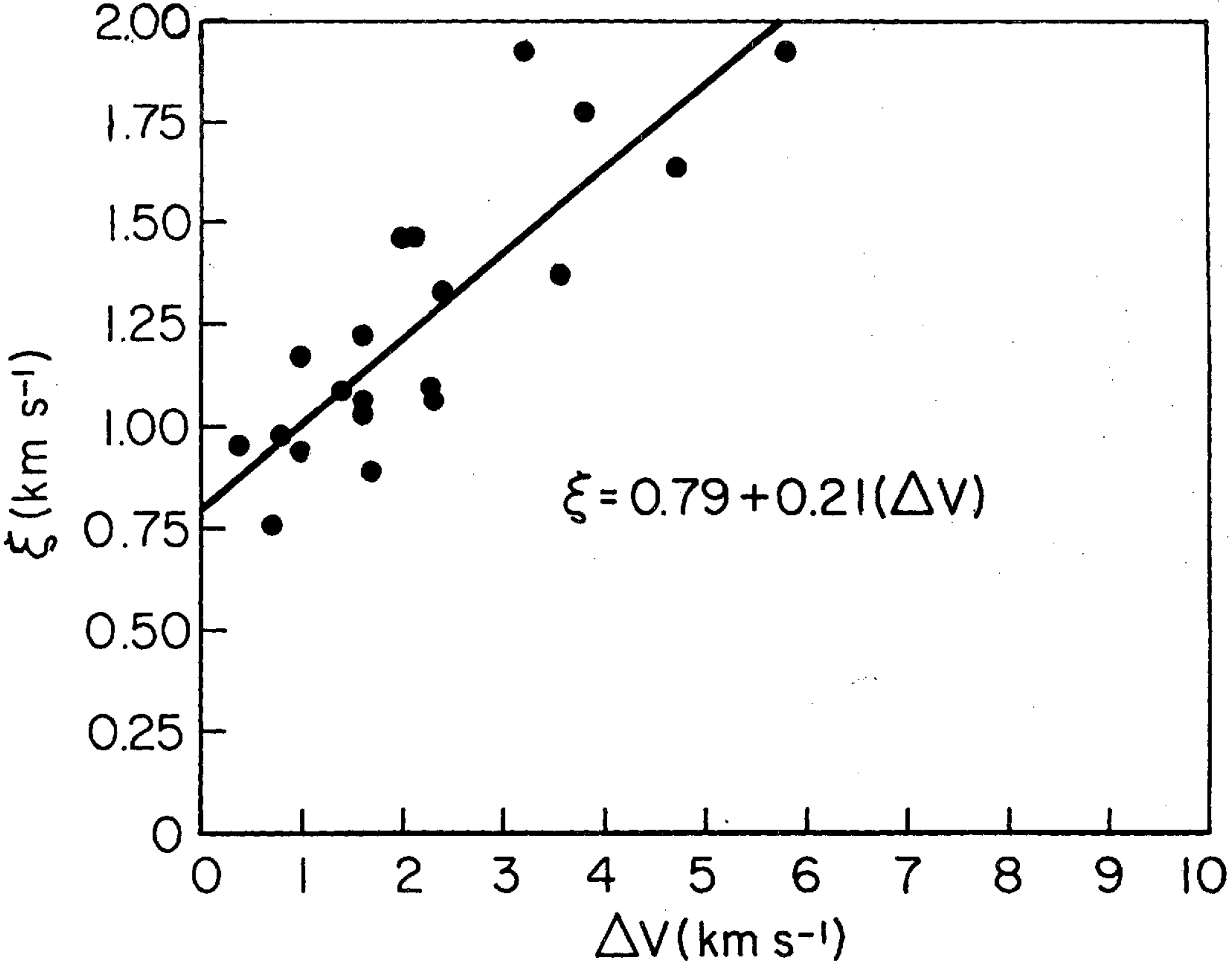
2.00
1.75
1.50
1.25
1.00
0.75
0.50
0.25
0
0
1
2
3
4
5
6
7
8
9
10
ξ (km s^{-1})
ΔV (km s^{-1})
$\xi = 0.79 + 0.21(\Delta V)$

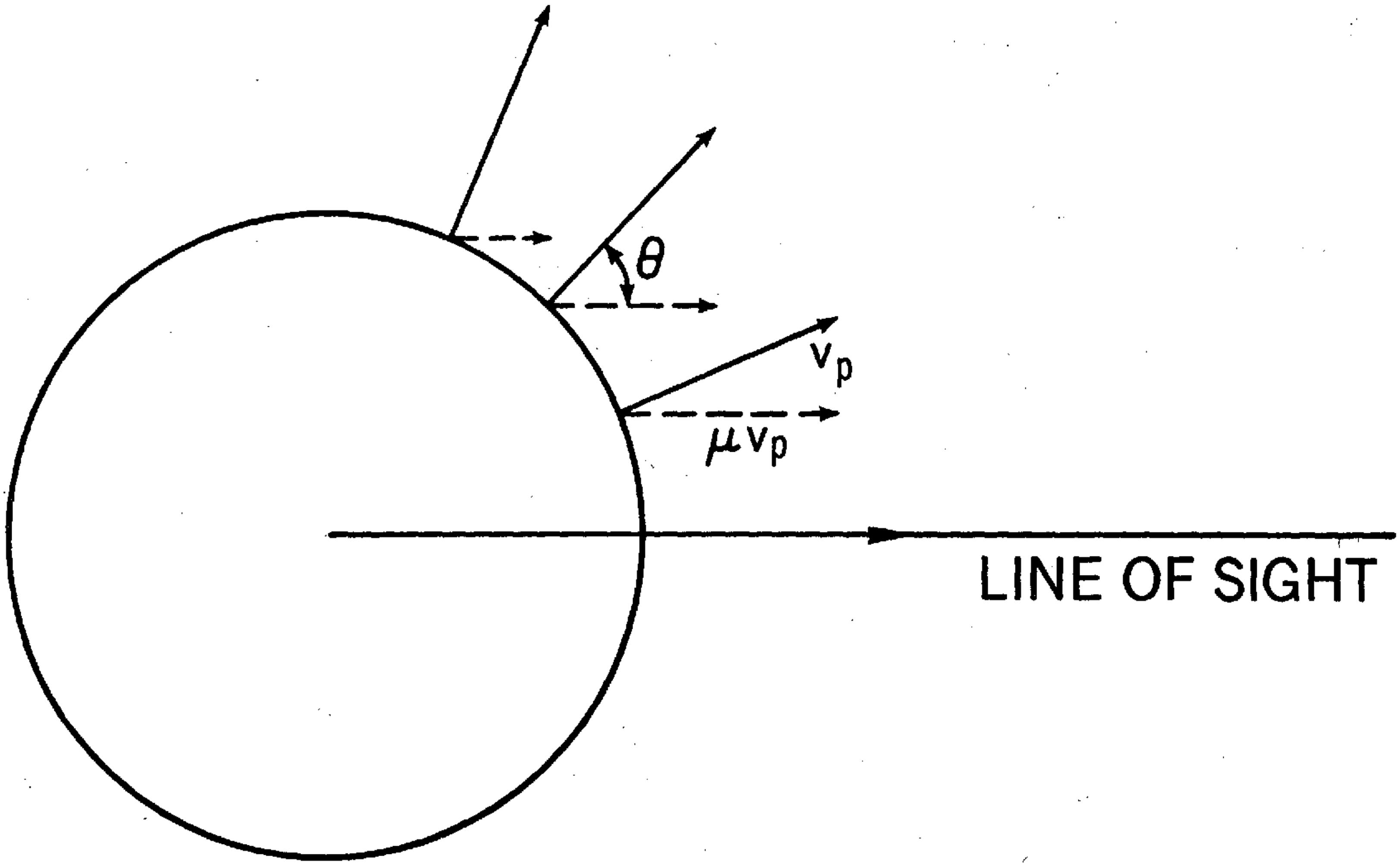

Figure V-6. Schematic illustrating effect of angle integration on a line profile in an expanding atmosphere.

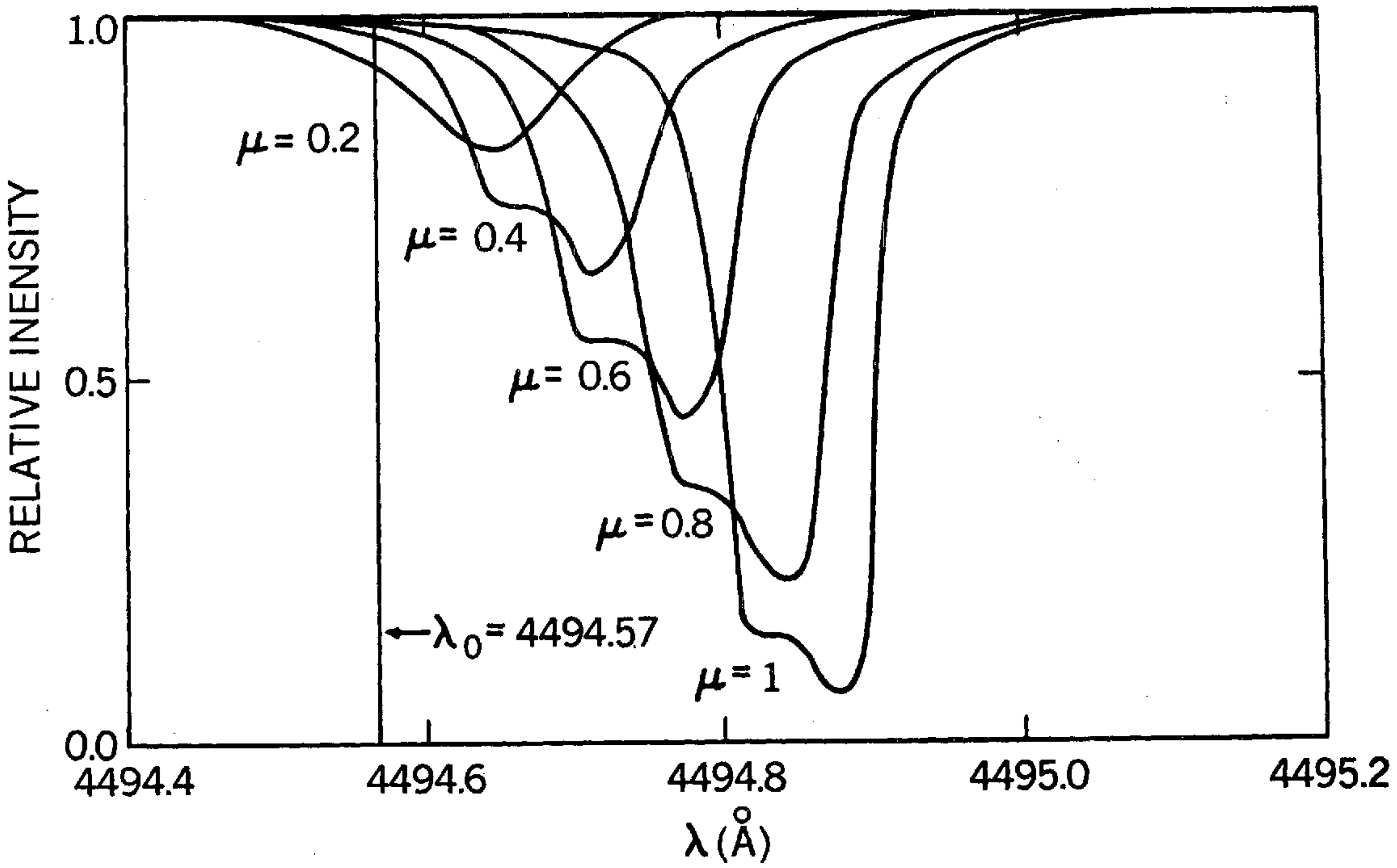

Figure V-7. Intensity profiles of lines in an expanding atmosphere. The curves are labelled with the corresponding value of $\mu = \cos\theta$.

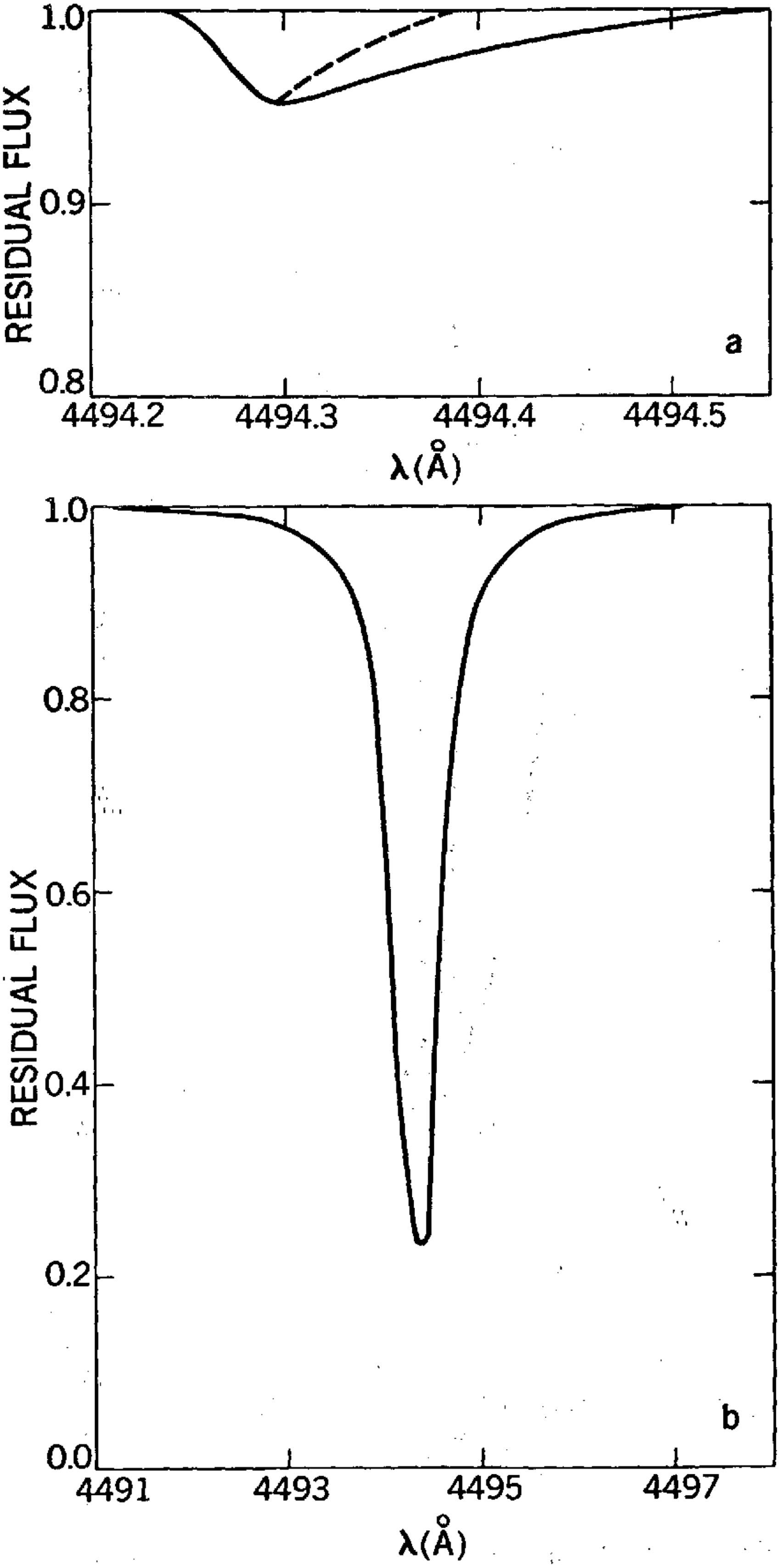

Figure V-8. a) Profile of a weak line in a moving atmosphere without velocity gradient. The dashed line is the bisector.

b) Same as (a) for a strong line.

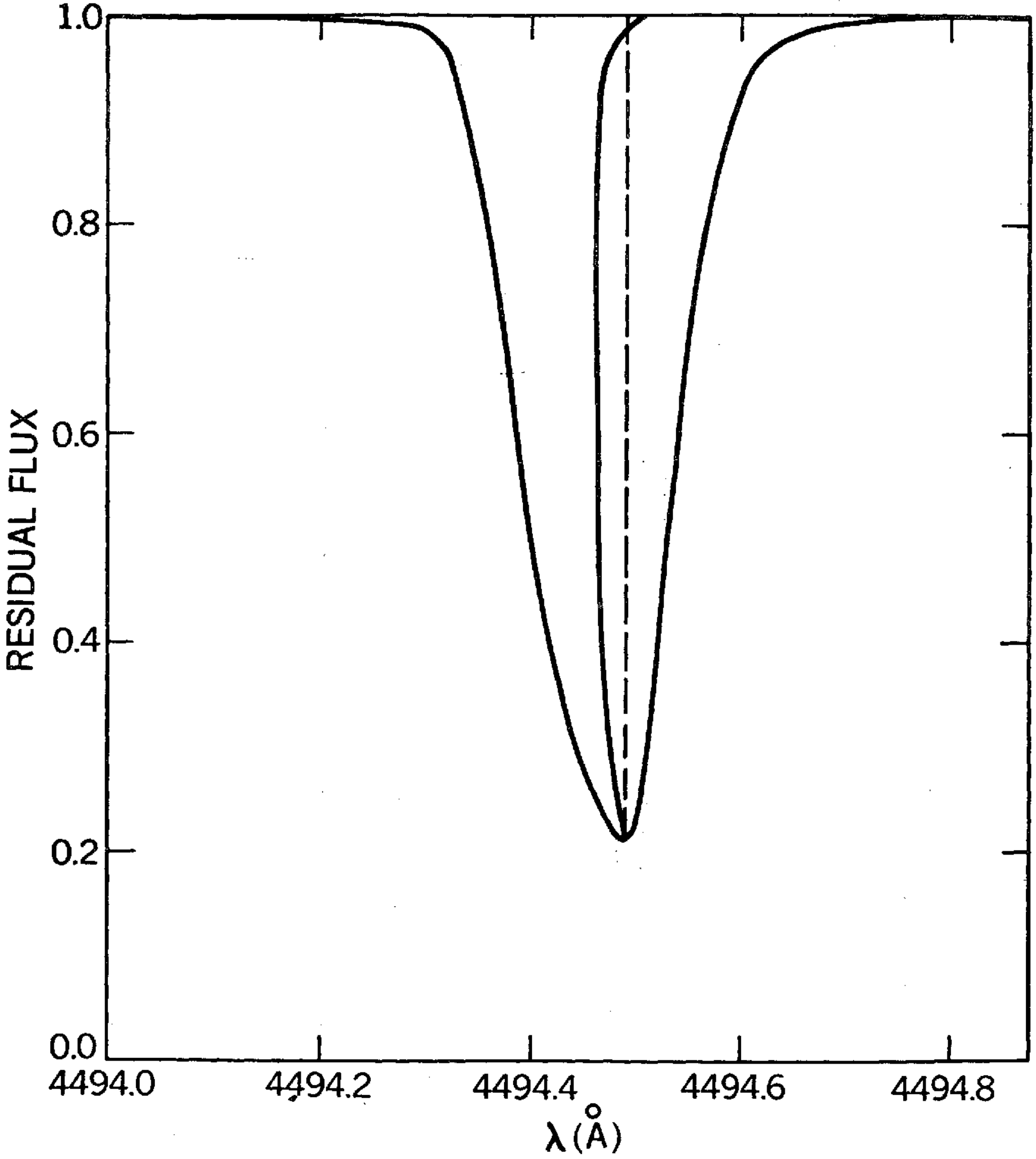

Figure V-9. Profile of a strong line in an atmosphere with a velocity gradient. The dashed line is a straight line drawn vertically from the minimum of the profile. The bisector of the profile is also shown.

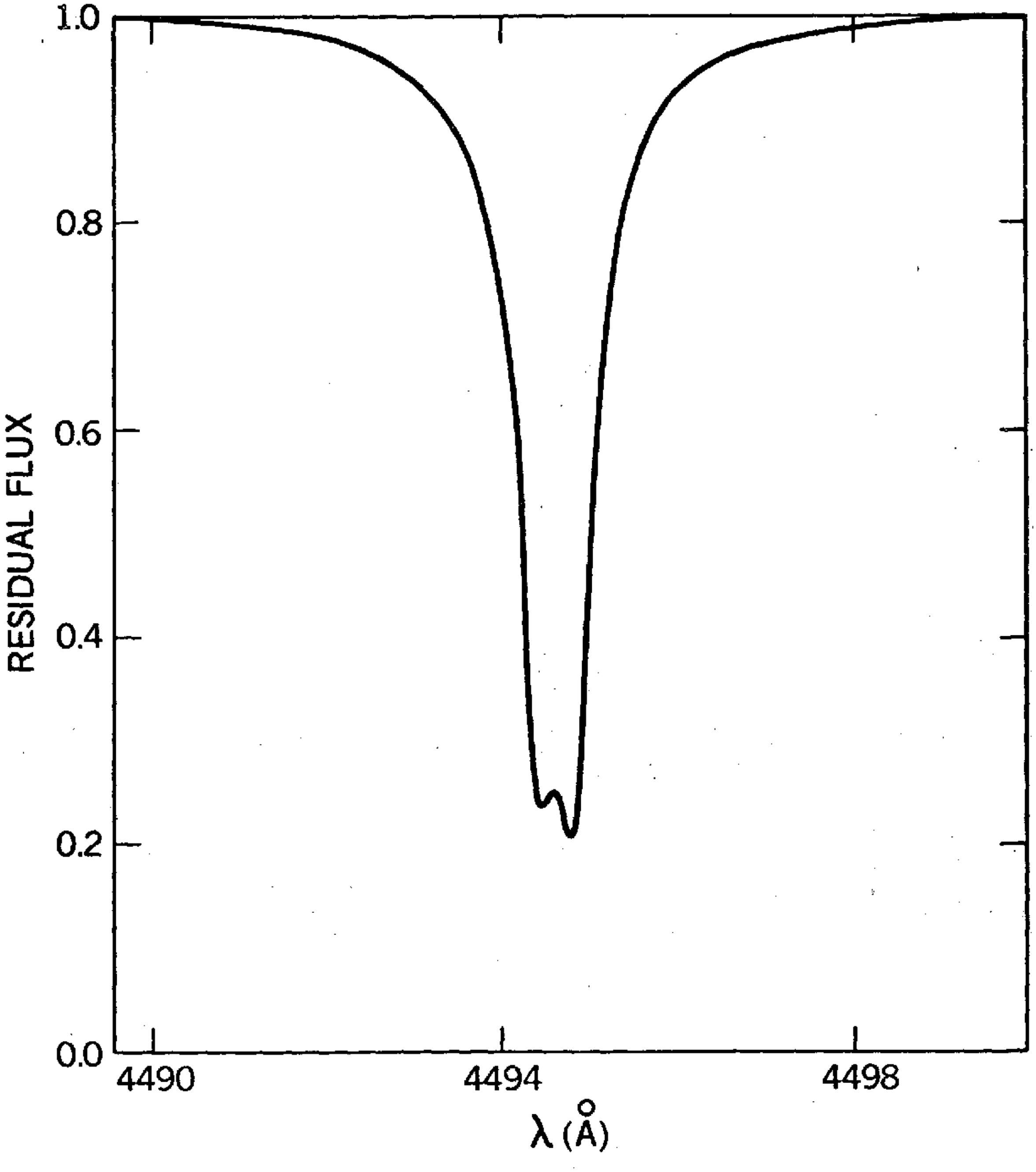

Figure V-10. Line profile showing a "Cheshire Cat" line.

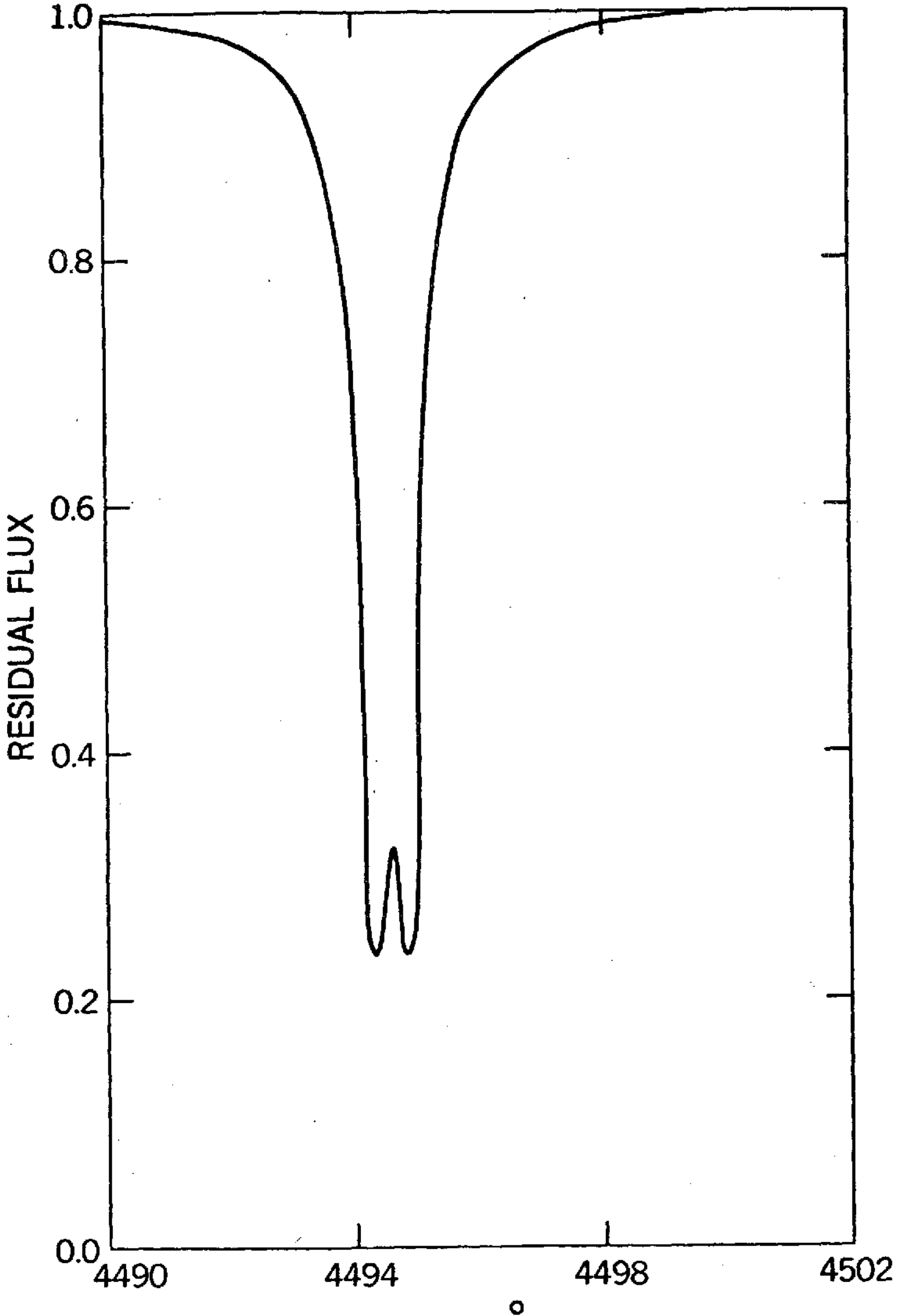

Figure V-11. Same case as Figure V-10 but with all velocities set to zero.

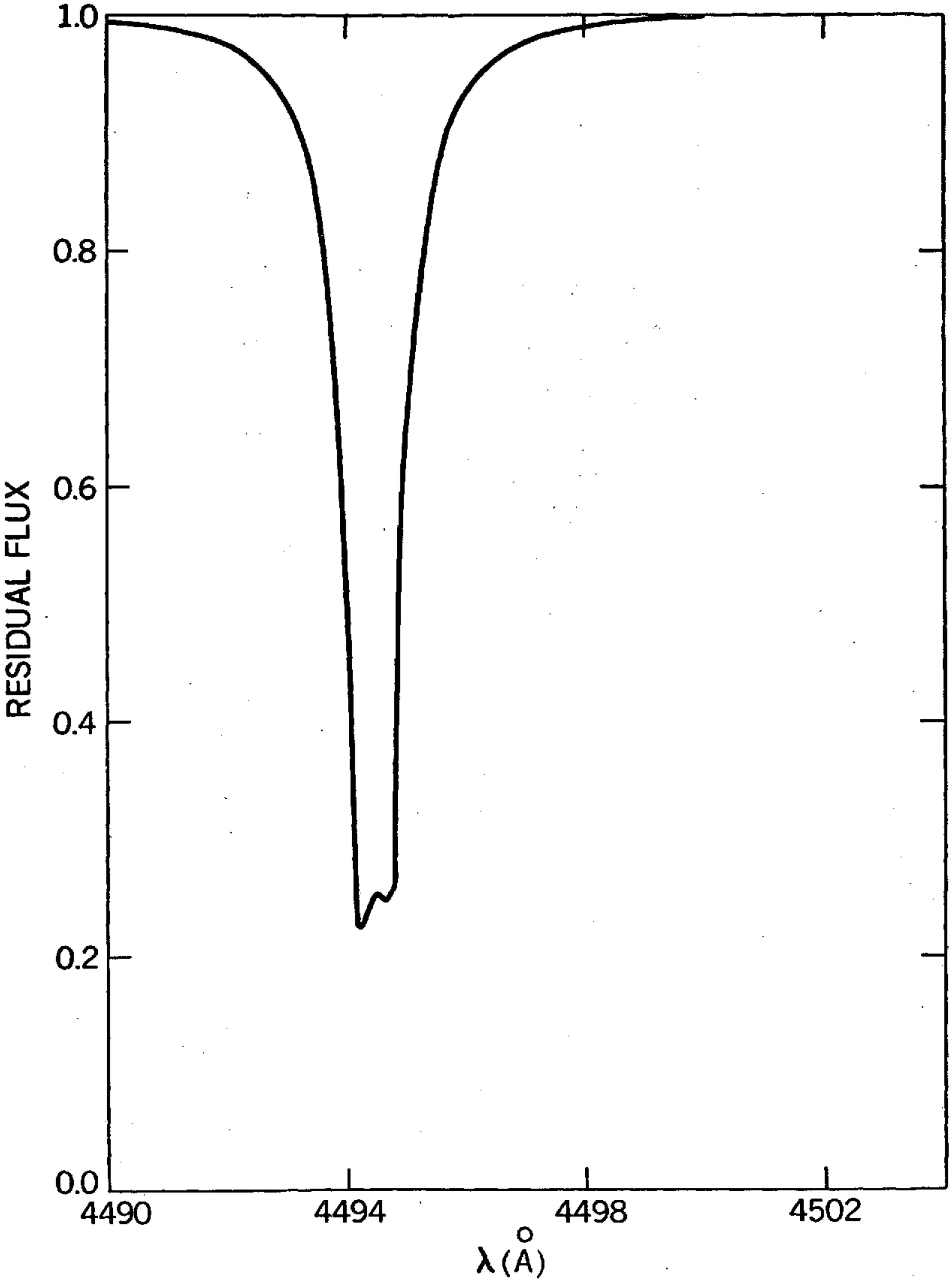

Figure V-12. Same case as Figure V-10 but with a constant velocity in the atmosphere.

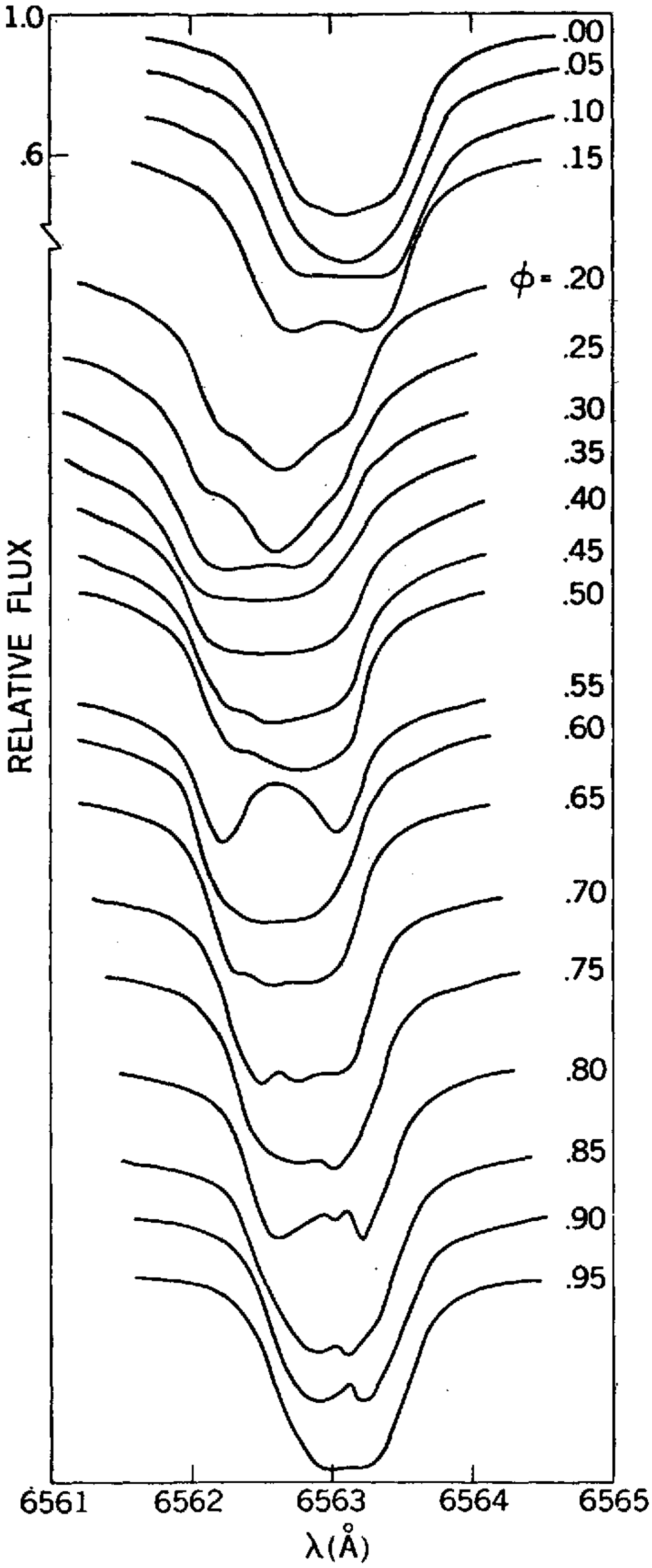

Figure V-13. H_α profiles computed using the hydrodynamic models. The profiles have been shifted vertically by an arbitrary amount. The phase at which each profile was computed is shown at the right.

Figure V-14. Ratio of pulsation to observed radial velocity, p, vs. ratio of pulsation velocity to half width of line, γ. Dashed line is Parsons' (1972) relation.

a) Weak line measured at minimum of profile
b) Strong line measured at minimum of profile
c) Weak line measured at half intensity point
d) Strong line measured at half intensity point

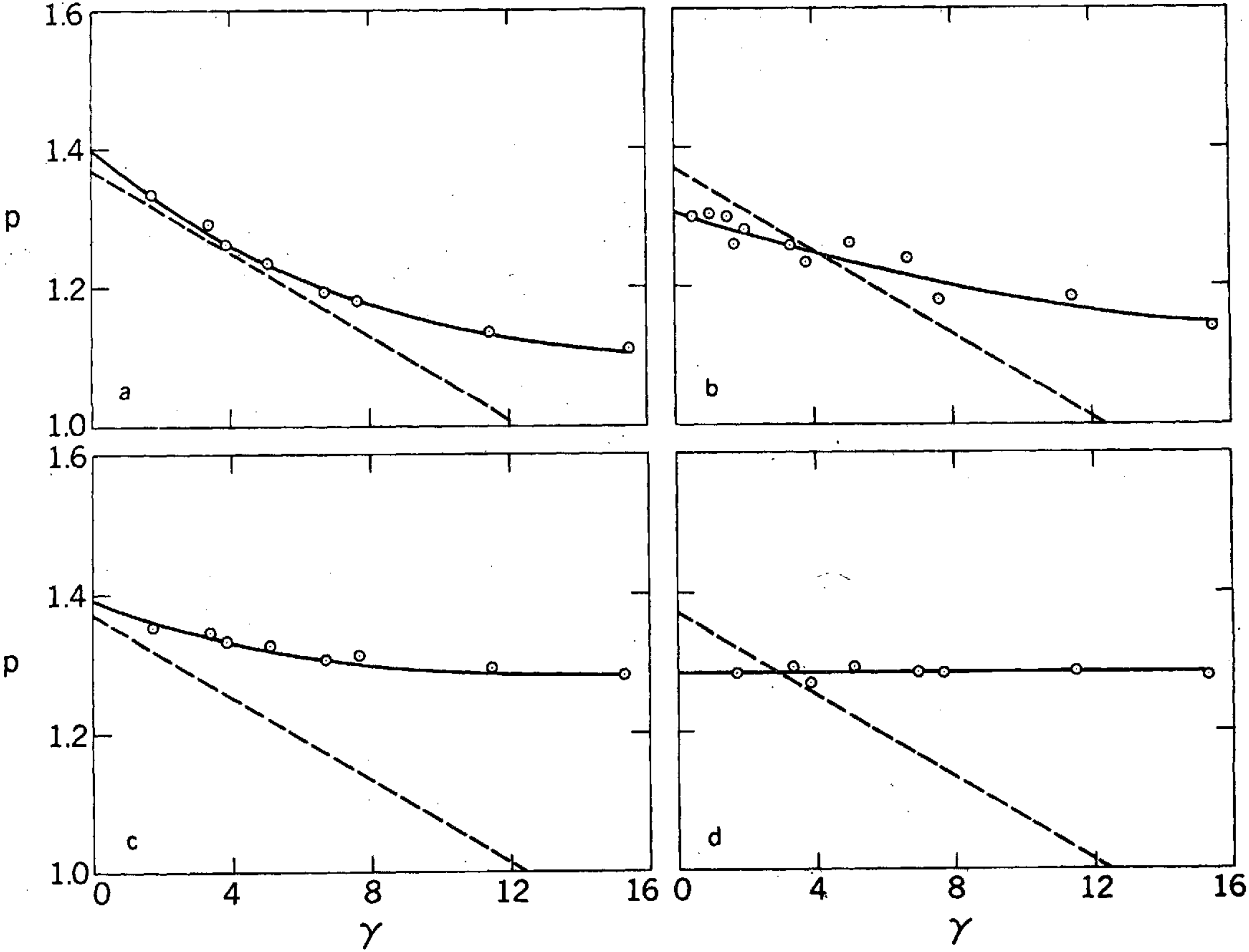
1.6
1.4
1.2
1.0
p
a
b
c
d
0
4
8
12
16
γ

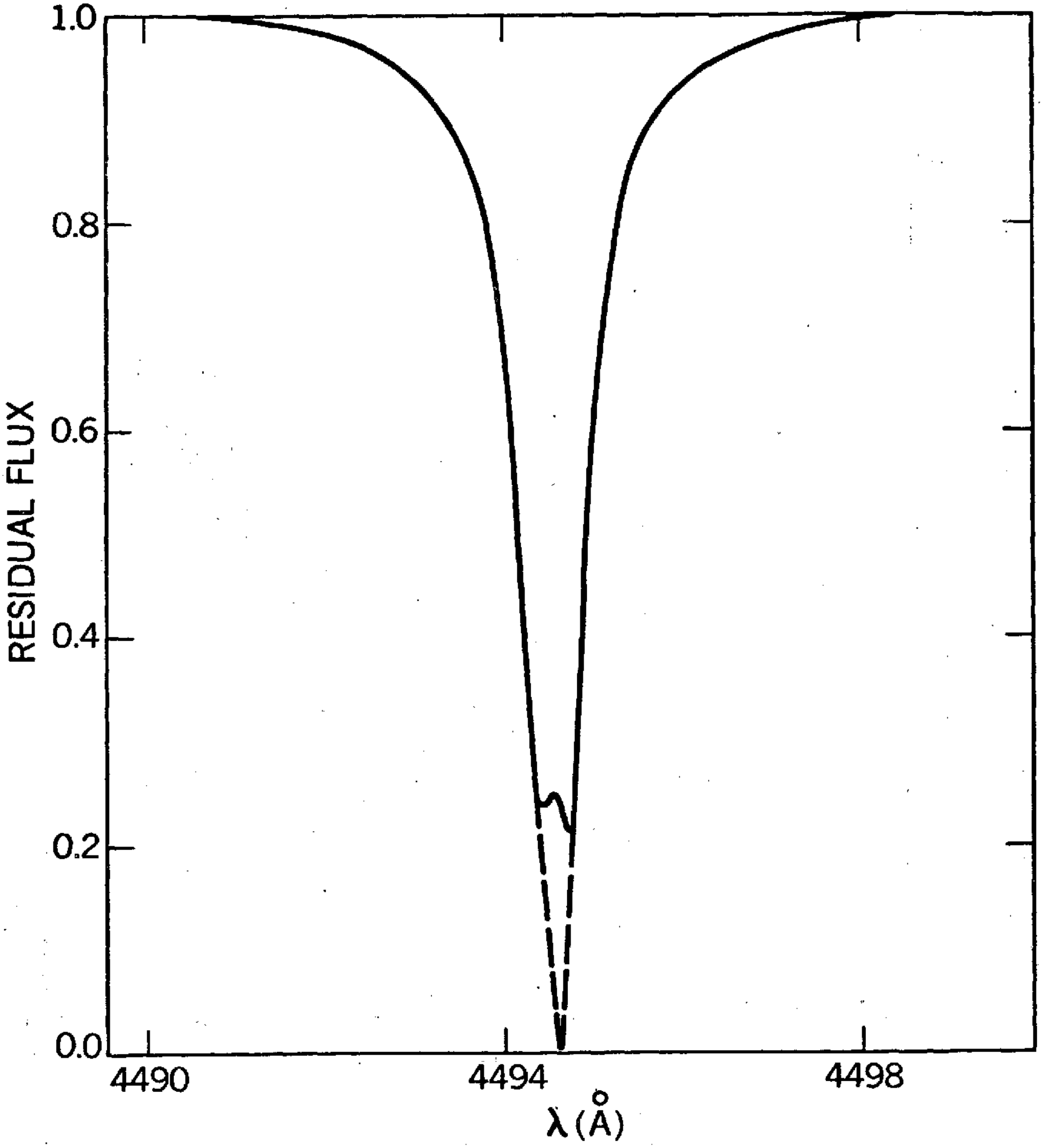

Figure V-15. Method for computing velocity characteristic of line core when core is split. Velocity is measured from intersection of dashed lines.

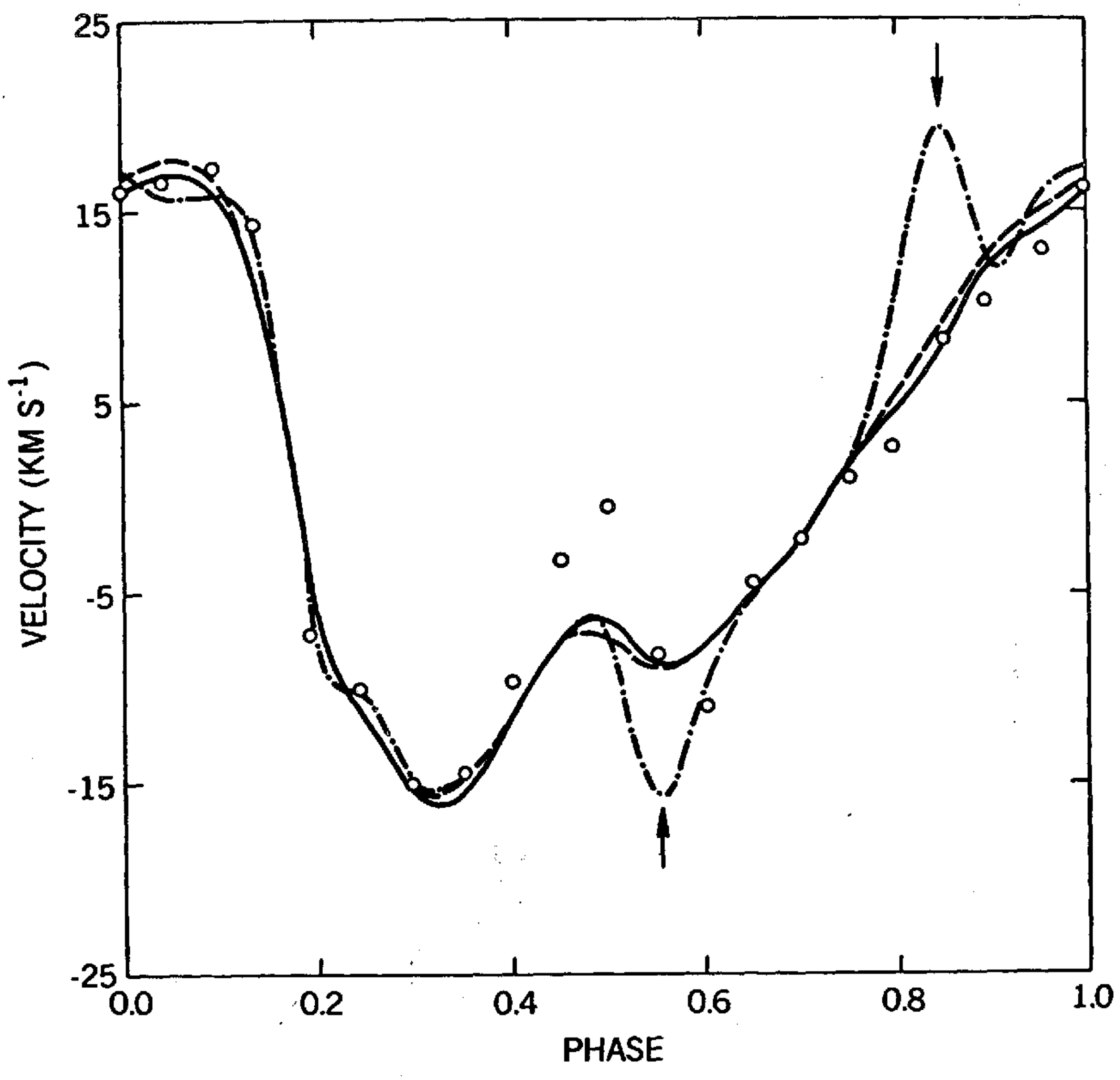

Figure V-16. Velocity curves. —— intermediate strength line, --- weak line, —— . —— strong line, o H_α determined using method described in text.

Figure V-17. Adopted velocity curve measured from line profiles

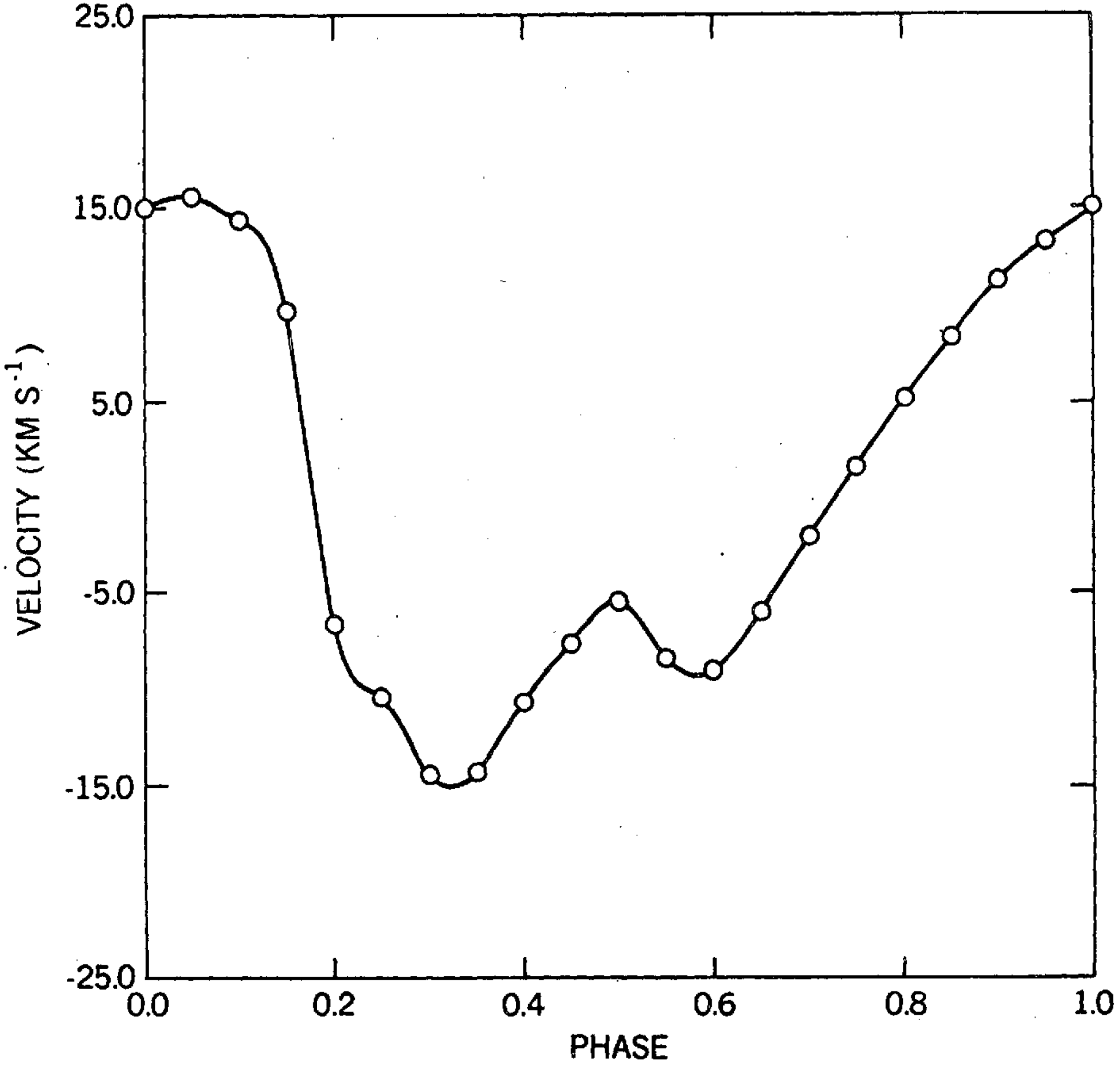
25.0
15.0
5.0
-5.0
-15.0
-25.0
VELOCITY (KM S^{-1})
0.0
0.2
0.4
0.6
0.8
1.0
PHASE

CHAPTER VI

DETERMINATION OF CEPHEID RADII

A. Radius determination methods.

1. Bolometric radius.

There are two ways to find the radius of a Cepheid from observed quantities. The first method involves solving

$$L = 4\pi R^2 \sigma T_{eff}^4 . \qquad \text{(VI-1)}$$

for the radius. The radius found in this way will be referred to as the bolometric radius. The mean luminosity of the star is found from the period-luminosity law while, in the simplest application, the temperature is calculated from the color. There are obvious drawbacks. A change of the zero point of the period-luminosity law of $0\overset{m}{.}1$ changes log R by 0.02, about 4%. In addition, the solution is very sensitive to errors in T_{eff}, which, if broad band colors are used to define T_{eff}, depends on the assumed reddening. Whitney (1955) attempted to improve this approach by using model atmospheres to determine the flux of the star and finding $\log R_*/R_\odot$ from

$$M_\odot - M_* = 2.5 \log \left\{ \frac{\int F^s_{\nu_*} S^i_\nu d\nu}{\int F_{\nu_\odot} S^i_\nu d\nu} \right\} + 5 \log (R_*/R_\odot) \qquad \text{(VI-2)}$$

where S^i_ν is the sensitivity function of the filter used to find M_*. Oke (1961 a, b) made a further improvement by making absolute flux measurements in 50 Å bands. He then compared these fluxes to those computed from model atmospheres to find T_{eff}. While both of these approaches remove some of the errors inherent in the color-T_{eff}

calibration, they require knowledge of the line blocking. An error of only 50°K in T_{eff} results in an 0.01 change in log R. In addition to these systematic errors, the gravity variations, which can be as large as a factor of 10 (Parsons 1971 a, b; see also Chapter IV) will produce an error that varies during the pulsation cycle.

2. Baade and Wesselink radii.

One way to find the radius that avoids these problems is the Wesselink (1946) method. Based on an idea of Baade (1926), the method uses both the light and velocity curves to find the radius. Baade proposed using the change in brightness to give the ratio of the radii from

$$M_1 - M_2 = 5 \log R_2/R_1 + 10 \log T_2/T_1 , \qquad \text{(VI-3)}$$

and the velocity curve to give

$$R_2 - R_1 = \int_{t_1}^{t_2} v \, dt.$$

Baade's method requires knowledge of the color temperature law. It was not surprising when Bottlinger's (1928) attempt to find the radius of ζ Gem failed since he assumed the star radiated like a black body. Becker (1940) improved the situation by assuming only that a single valued color-T_{eff} law existed and obtained radii for a number of Cepheids.

Wesselink (1946) removed the problem of the color-T_{eff} law when he suggested choosing two phases at which the star has the same color. If it is assumed that equal color implies equal temperature, the last term on the right of equation (VI-3) vanishes, and there is no need to know even the form of the color-T_{eff} relation. The Wesselink method also has the advantage that it is independent of both the zero point of the period-luminosity law and the interstellar reddening.

There are two other assumptions inherent in the Wesselink method. First, the mass depth of the line forming region is assumed constant with phase so that the observed velocity curve follows a given element of gas. Second, it is assumed that the ratio of the radii of the line forming and continuum forming regions is constant with phase. These assumptions will be examined below.

There are, of course, problems with the method. Accurate velocity curves are required and any change in p, the ratio of pulsational to observed radial velocity, produces a systematic error in the radius. In addition, loops in the (U-B) - (B-V) diagram indicate that equal color does not necessarily imply equal temperature. It is also known that the opacity scale changes during the cycle so that different elements of gas are observed at different phases. Velocity gradients measured in Cepheid atmospheres by Sanford (1956) and Dawe (1969), among others, indicate that the ratio of radii of the photosphere and reversing layer changes during the pulsation cycle but the size of this change is not known. Fernie and Hube (1967) have also shown that small errors in reducing the light and velocity curves to the same epoch produce large errors in the derived radius. In spite of these difficulties excellent results have been obtained.

B. Calculated radius of the hydrodynamic model.

1. Wesselink radius.

Most papers reporting Cepheid observations include a section computing the radius by Wesselink's method. In accordance with this tradition, the results of the previous chapters can be treated as observations and the radius of RDT calculated using Wesselink's method. The light and color curves of Chapter IV and the velocity curve of Chapter V have been adopted as if they were observations of a star. As pointed out previously, zoning effects limit the accuracy of the light and color curves to about $0^{m}.02$ which translates into an 6% random error in the radius. The integral of the adopted velocity curve indicates an error of 0.2 km s^{-1} in the center of mass velocity of the star. Combined with a random error of 2% from changes in p, the minimum error expected is 10%, 8% random and 2% systematic. Since Fernie (1968) was dealing with less accurate velocity data than that used here, his adopted error of 10% appears to be an underestimate.

Figure VI-1 shows the radius curve derived from the adopted velocity curve (dashed line) and the radius of $\tau = 1$ taken directly from the models (solid line). The amplitude of the radius curve determined from the lines is about 7% larger than the variation of the photospheric radius. This error will result in an overestimate of the radius amplitude but should have only a small effect on the computed value of the mean radius. It appears, therefore, that errors introduced into the mean radius by changes of the opacity scale with phase and by velocity gradients in the atmosphere are small.

Figure VI-2 shows the results of the Wesselink calculation performed by taking pairs of points with equal (B-V), (V-R), and (R-I). The solid line was taken directly from the models. The error bar shows that the expected error of a single measurement is comparable to the total radius variation. Therefore, all that can be derived from these values is the mean radius. STB has a radius of 71.7 $R_\odot$ while the Wesselink calculations give 58.5 ± 4.0, 73.5 ± 8.7, and 67.3 ± 5.2 for (B-V), (V-R), and (R-I), respectively, where the quoted errors are the standard deviations computed from several radius determinations. The agreement is satisfactory except for the (B-V) curve which is most sensitive to changes in g_{eff}. It thus appears that the Wesselink method can be used to find the mean radius of a Cepheid with an accuracy of about 10% only if very high accuracy observations are available.

2. Baade radius.

At the time Wesselink published his modification of Baade's method, the color-T_{eff} relation was not known accurately. Since then the relation has been calibrated for several different color systems. In Chapter IV, it was shown that the color-T_{eff} relations derived for RDT agree with those derived from observations. Figure VI-3 shows the values of R/R_0, where R_0 is the radius at $\Phi = 0$, derived using Baade's method. The notation is the same as in Figure VI-2. Using Baade's method introduces an additional error. A change of $0\overset{m}{.}02$ in the color results in an error of 2% in the radius. Baade's method does not depend on the zero point of the color-T_{eff} law or that of the reddening law. Only the slopes of these relations enter the calculations.

The agreement with the model is quite good except near maximum light ($\Phi = 0.35$). The radii derived from (R-I) are more accurate than those of (B-V) and (V-R), especially near minimum light. Combined with Figure VI-1, mean radii in solar units of 77.2 ± 7.8 from (B-V), 79.6 ± 4.7 from (V-R), and 73.6 ± 5.5 from (R-I) are derived.

If the points near maximum light are removed, these values become 71.0 ± 5.5 (B-V), 74.2 ± 3.8 (V-R), and 73.6 ± 2.8 (R-I). Again the agreement is satisfactory, and there appears to be no need to select only phases of equal color unless the reddening is not known.

3. Bolometric radius.

One further set of radius determination was made, this time using Equation VI-1. Temperatures were computed from the color-T_{eff} relations derived in Chapter IV. The bolometric magnitude of the sun, $M_{BOL} = 4.72$, and the solar effective temperature, $T_{eff} = 5800°K$, were taken from Allen (1963). In this case an error of 0.01 in the zero point of the color-T_{eff} relation introduces a systematic error of 5% into the radius determination. A random error of 8% and a systematic error of 7% can, therefore, be expected. The mean radius derived is 69 ± 2 $R_\odot$ regardless of which color was used. The agreement is again satisfactory, and this method can be used for stars that do not have accurately measured velocity curves. The radius determinations are summarized in Table VI-1.

C. Method of Wooley and Savage.

Some comments are in order on the modification of the Wesselink method proposed by Wooley and Savage (1971) and Wooley and Carter (1973). Their main point is that the color depends on g_{eff} as well as T_{eff}. Thus, it is necessary to include the luminosity of the star in the calculation, which means both the mass and radius can then be found. They also use a velocity function instead of the observed velocities which are often too poorly determined to be useful. Figure VI-4 compares the adopted velocity curve of RDT (solid line) with the velocity function of Wooley and Carter (1973) scaled to a semi-amplitude of 15 km s^{-1} (dashed line). There is a reasonably good agreement between the two curves except near the second bump.

Wooley and Savage make two unnecessary assumptions, however. First, they make the assumption that $\Delta R/R$ is small enough that $\ln(1 + \Delta R/R) = \Delta R/R$. Fernie and Hube (1967) have shown that this assumption leads to an underestimate of the radius of 5 to 10%. In particular, the radius of RDT would be underestimated by 11%. Second, they assume that the accelerations of the atmosphere are always small compared to $g = G\,M/R^2$ when in fact they are often much larger than g (Parsons 1971; see also Chapter IV). These two underestimates are partially cancelled by using $p = 24/17 = 1.41$, instead of the smaller value suggested by Parsons (1972) and in Chapter V.

As shown in this chapter, though, the gravity variations have only a small effect on the derived mean radius, especially if (R-I) is used. Even the change of the opacity scale with phase produces only small errors in the mean radius if sufficiently weak lines are used to define the velocity curve. With the best observations it should be possible to achieve an accuracy of 10% with any of the methods discussed above. In practice, however, the errors may be closer to 15 or 20% due to additional errors introduced by the lower accuracy of the observed velocities.

Table VI-1

Radius determinations of hydrodynamic model in solar units

$R_{STB} = 71.7$

	B-V	V-R	R-I	expected error	
Method	R ± s.d.	R ± s.d.	R ± s.d.	random	systematic
Wesselink (1946)	58.5 ± 4.0	73.5 ± 8.7	67.3 ± 5.2	8%	2%
Baade (1926) all points	77.2 ± 7.8	79.6 ± 4.7	73.6 ± 5.5	10%	2%
some points*	71.0 ± 5.5	74.2 ± 3.8	73.6 ± 2.8	10%	2%
$L = 4\pi R^2 \sigma T^4$	69.4 ± 2.0	69.5 ± 2.2	69.2 ± 1.6	8%	7%

*excluding points near maximum light

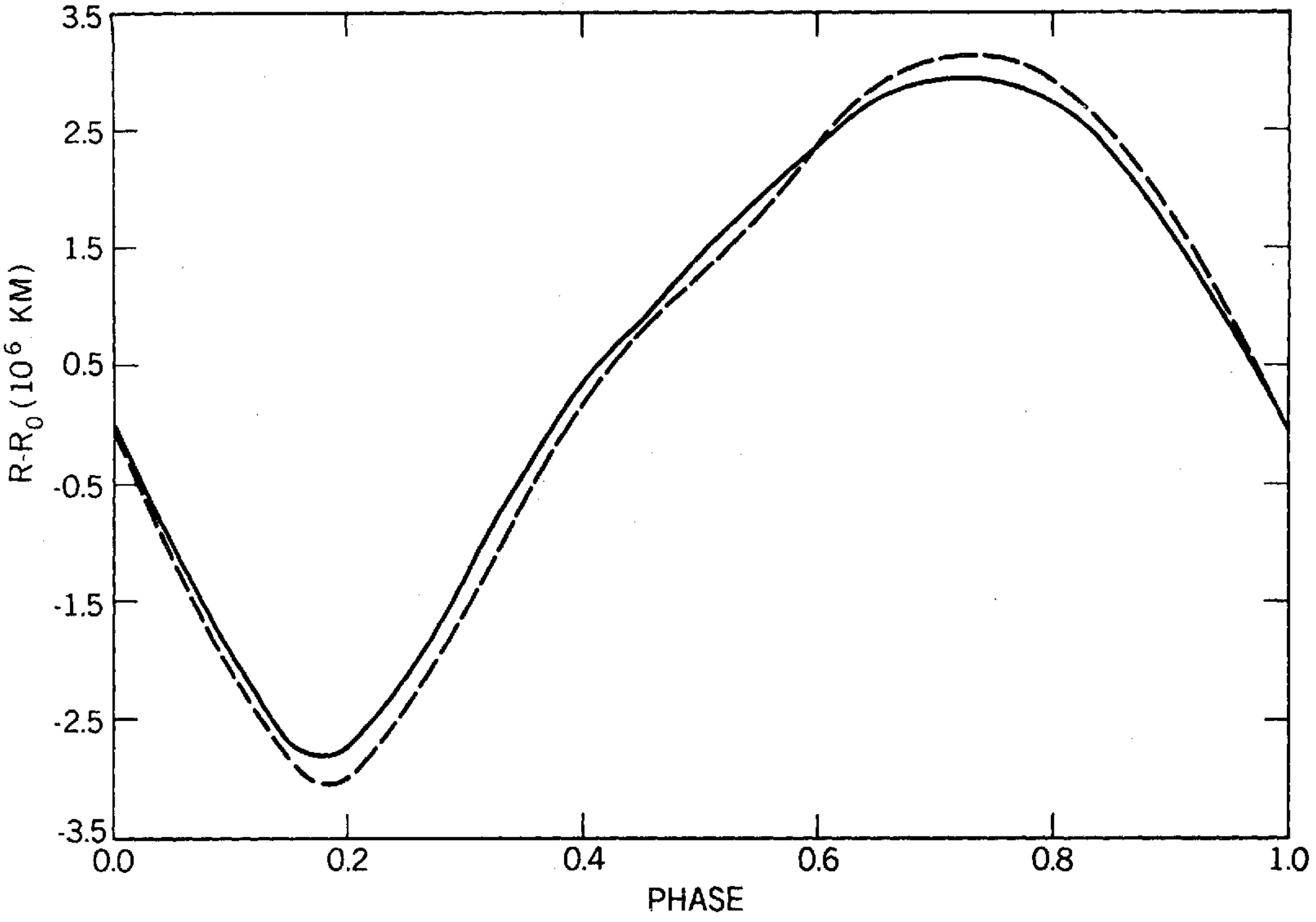

Figure VI-1. Change of radius, $R-R_0$, vs. phase —— from models, --- from adopted velocity curve.

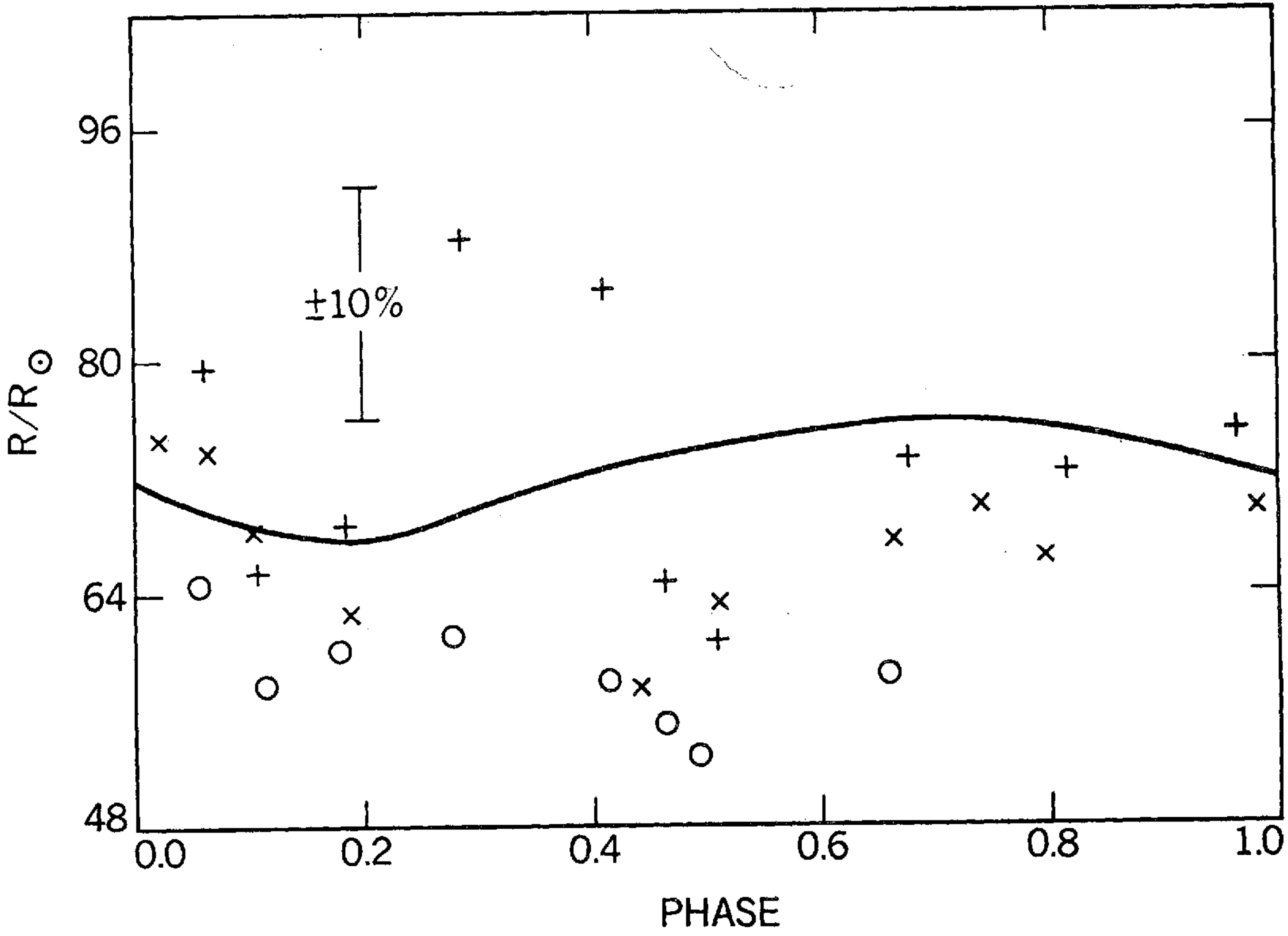

Figure VI-2. Wesselink radius R/R$_\odot$, vs. phase. Solid line from models; 0 from (B-V), + from (V-R), x from (R-I).

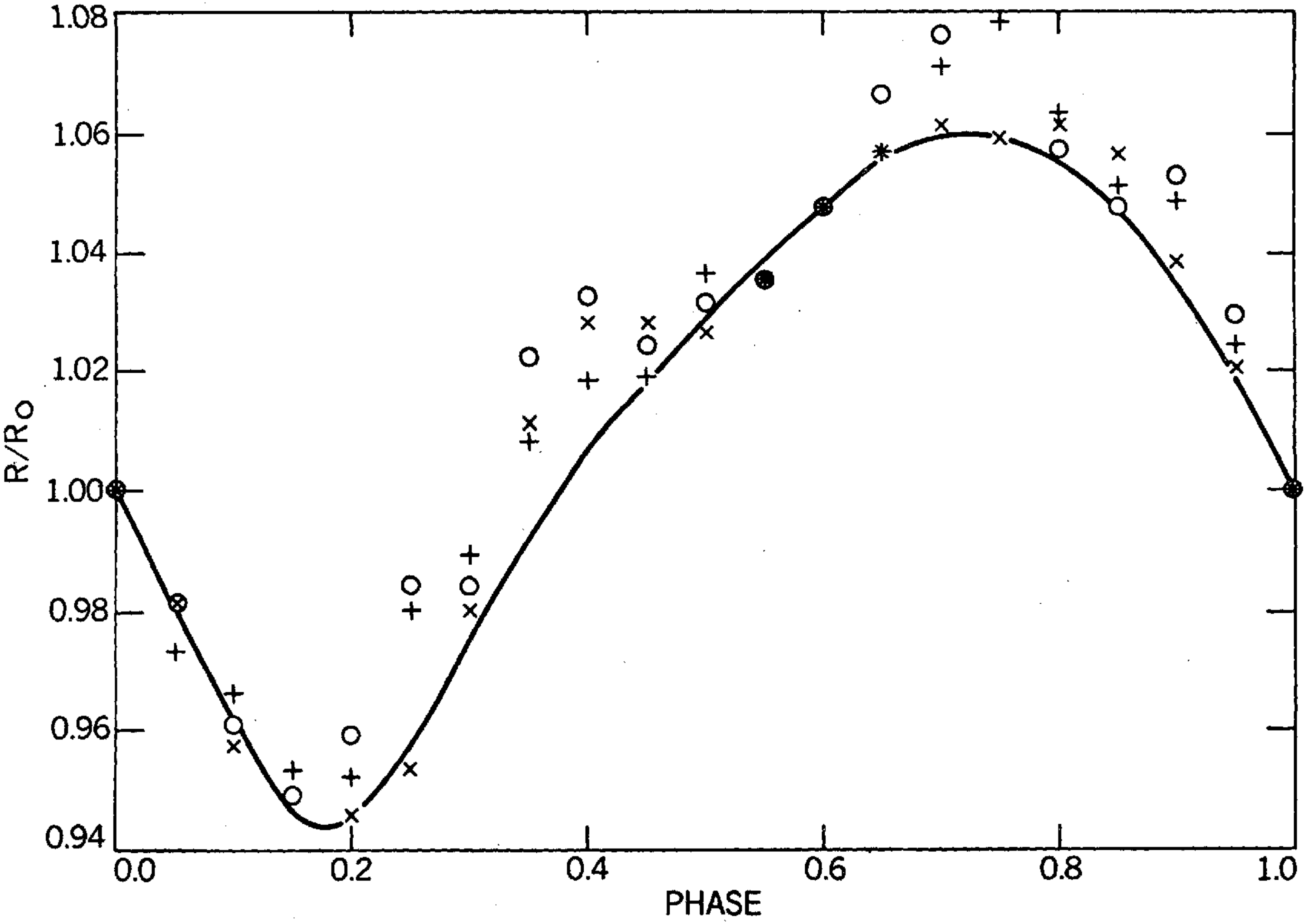

Figure VI-3. Baade radius vs. phase. Notation same as in Figure VI-2.

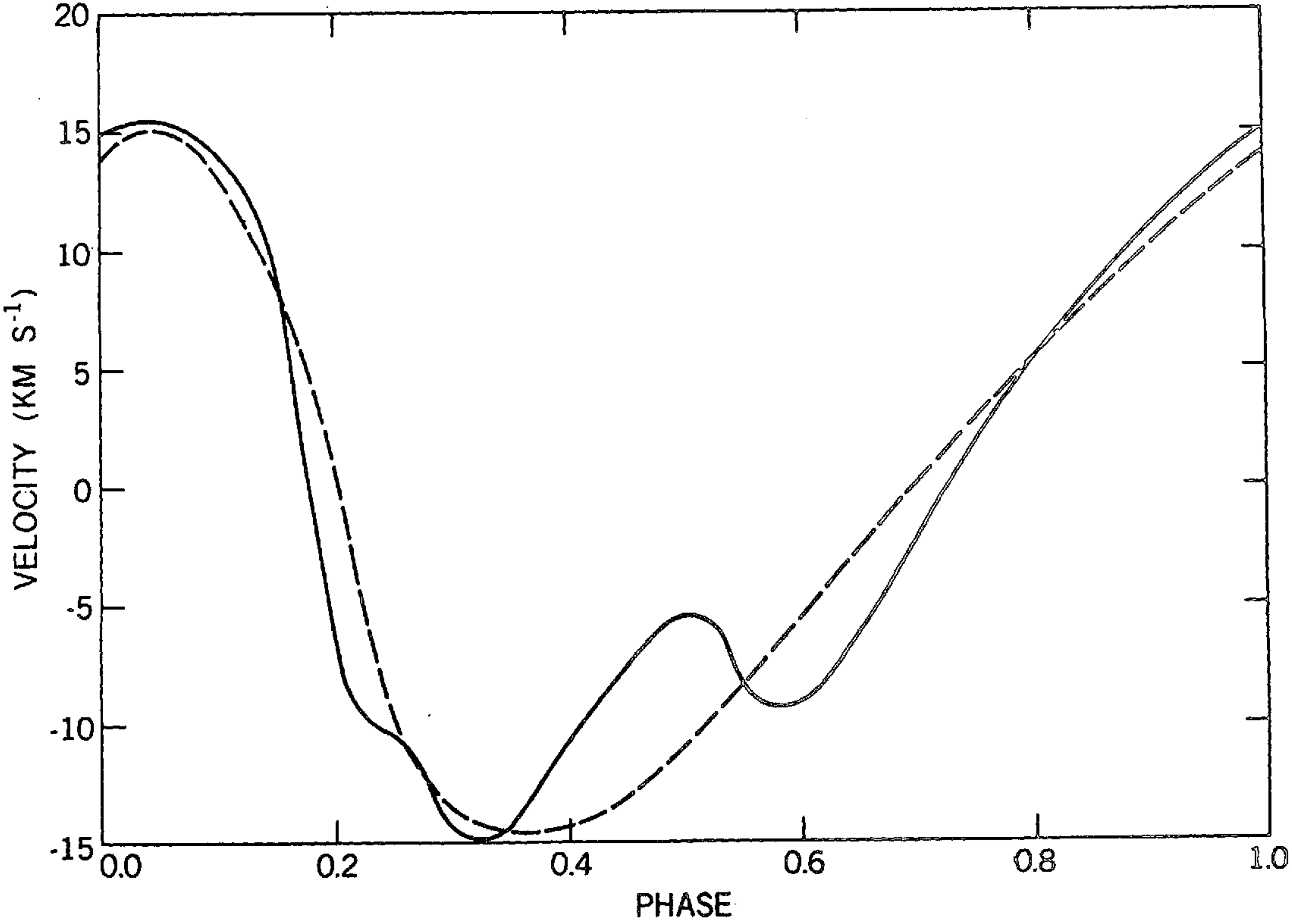

Figure VI-4. Adopted velocity curve (——) compared to velocity function of Woolley and Carter (1973) normalized to a semi-amplitude of 15 km s^{-1} (---).

CHAPTER VII

SUMMARY, CONCLUSIONS, AND FUTURE WORK

A. Summary and Conclusions.

Hydrodynamic models of the atmosphere of a 12^d Cepheid have been computed including the effects of radiative transfer in the optically thin zones. A new method of including radiative transfer in a standard Henyey type hydrodynamic code has been developed. The differences between using the diffusion approximation and the solution of the transfer equation have been shown to be negligible except above $\tau = 10^{-2}$ where temperature inversions occur only in the radiative transfer case. A study of the envelope of the full amplitude model indicates that the phase lag between maximum light and minimum radius increases continuously between the HeII and H ionization zones. The asymmetry of the light curve appears to originate in the H ionization region.

The Hertzsprung sequence has been examined and a mechanism presented to explain the occurrence of two bumps on Cepheid light curves. The bump occurring on the falling branch of the light curves of 7^d to 10^d Cepheids and on the rising branch of 10^d to 15^d Cepheids is caused by the Christy mechanism, i.e., a pressure wave which propagates into the star, reflects from the stellar core, and appears on the next pulsation cycle. The other bump which appears on the falling branch of 10^d to 15^d Cepheids is due to an atmospheric oscillation. This bump occurs when the natural pulsation mode of the atmosphere, which has a shorter period than the envelope, has a large enough amplitude to generate a shock wave by compressing the hydrogen ionization region. When this shock reaches the surface it appears as a bump on the falling branch of the light curve. Since two mechanisms produce bumps on Cepheid light curves, masses derived from the phase of the bump may be unreliable. While it has been shown that this mechanism is consistent with the Herzsprung sequence, more models must be computed to fully study this atmospheric oscillation mechanism.

The hydrodynamic models were then used to compute UBVRI colors by treating the model at each time step as a snapshot of the atmospheric structure. A P-V diagram of the atmosphere constructed from the effective temperature and gravity at each phase indicates the destabilizing influence of the hydrogen ionization region. These effective temperatures and gravities were then used to compute line blocking coefficients which were applied to the monochromatic fluxes to give the colors of the models, including the effects of spectral lines. The color curves were smoothed to minimize the zoning effects, and it was shown that they reproduce the observed variation of light amplitude and phase of light maximum with effective wavelength. The color-T_{eff} relations were computed and were shown to agree with those derived independently. It was then shown that the loops in the (U-B)-(B-V) diagram are most likely caused by a nonthermal dependence of the continuous opacity. Mean colors of the model were computed using three averaging schemes, and it was found that the intensity means of the magnitudes, $\langle B\rangle_I - \langle V\rangle_I$, best represent the colors of the equilibrium model. The location of the equilibrium model in the H-R diagram indicates that the zero point of the Sandage and Tammann period-luminosity relation is too high by $0\overset{m}{.}2$.

Line profiles were then computed using the moving atmospheres from the hydrodynamic models. It was shown that, although the velocity gradients in the atmosphere are not responsible for the observed microturbulence or variation of microturbulence, they can be used to explain the occurrence of supersonic microturbulence. The total observed microturbulence was shown to be consistent with the linear sum of the classical microturbulence and that caused by the velocity gradients.

The splitting of the cores of strong lines was shown to be due to shock induced temperature inversions in the Cepheid atmosphere. This mechanism explains why the splitting is observed only in strong lines in classical Cepheids and why the splitting in H_α and CaII H and K is greater than in the strong metal lines. The splitting of the line core makes velocity measurements from the minimum of the profile unreliable, but a method for determining the velocity of the upper atmosphere was presented. The center to limb variations of the profiles were then studied, and it was shown that the commonly used ratio of the pulsation to observed radial velocity, $p = 24/17$, is too high. It was found that velocities obtained from the lines underestimate the velocity gradients present in the model atmospheres. It was also shown that the integral of the velocity over phase can be used to find the velocity of the center of mass of the star to the accuracy of observations in spite of changes in the continuous opacity scale during the pulsation.

The adopted light, color, and velocity curves were then used to study various methods for determining the mean radius of a Cepheid. The Wesselink method was found to give radii accurate to about 10% if errors in the observed velocity curves are minimized. Baade's method also produces accurate radius determinations if the currently accepted color-T_{eff} relations are used. It was also shown that the bolometric radius found from $L = 4\pi R^2 \sigma T^4$ is reasonably accurate and can be used for stars for which the velocity curve is not accurately known. However, the bolometric radius is susceptible to systematic errors introduced by errors in the reddening, the zero point and slope of the color-T_{eff} law, and the zero point of the period-luminosity relation. The Wesselink method is independent of these systematic errors, and Baade's method is affected only by errors in the slope of the color-T_{eff} relation. All these errors can be reduced by using R-I instead of B-V.

B. Future work.

There are several modifications to the models that would improve the agreement with observations, i.e., nongray radiative transfer, proper treatment of line blanketing, convective energy transport. The most important of these changes is the inclusion of convection. While it is true that convection can carry only a small part of the flux due to the low densities of Cepheid envelopes, the destablizing influence of the hydrogen ionization region is sensitive to changes in the temperature gradient. The atmospheric pulsation modes are also dependent on the temperature structure of the hydrogen ionization region. Since it takes a convective element about 0.1 period to move one pressure scale height, a theory of time dependent convection is needed.

Some of the assumptions made in calculating the models need to be investigated. One of the most common of these assumptions is that the lower boundary of the model can be kept fixed. Both the velocity and kinetic energy asymptotically approach zero in deep envelope models, but, as shown in Figure VII-1, a 3-D plot of momentum vs. mass point and phase, the momentum does not. The atmosphere has very little momentum due to the low density, but the momentum is being arbitrarily forced to zero at the base of the envelope by the zero velocity boundary condition. While it is not clear that this constraint is significant, a model should be computed with a free lower boundary to see if this assumption affects the observables.

Another interesting problem is the inhomogeneity of Cepheids. Examination of a catalog of light curves indicates that light curves of Cepheids with nearly the same period show striking differences. For example, ζ Gem with a period of $10^{d}.15$ has a low amplitude, nearly sinusoidal light curve, while β Dor with a period of $9^{d}.84$ has a large amplitude, asymmetric light curve with two distinct bumps. Our understanding of these differences is limited by the common practice of computing a model and finding a Cepheid with a similar light curve. More would be learned about these differences if a grid of models were computed to fit a single star as is done for stellar atmospheres. Such a grid could also be used to study the origin of the bumps on the light curves.

The hydrodynamic model atmospheres can also be improved by including more optically thin zones extending to smaller optical depth. Ideally these models should extend to a Rosseland mean optical depth of 10^{-6} to allow the strongest lines and the possible formation of a chromosphere to be studied. This extension of the model will probably require that the plane parallel assumption be dropped.

The line profile calculations can also be improved by including non-LTE effects, especially if "Cheshire Cat" lines are to be studied. The ratio of pulsation to radial velocity, p, should be studied further since its variation with line width and line strength is not understood. In particular, the variation of p with pulsation velocity should be included when constructing velocity curves as demonstrated by Duquesne and Schatzman (1955). Until the variation of p is understood errors in the radii determined by the Wesselink or Baade methods cannot be reduced much below 10% and the period-radius relation cannot be used to detect stars pulsating in overtone modes.

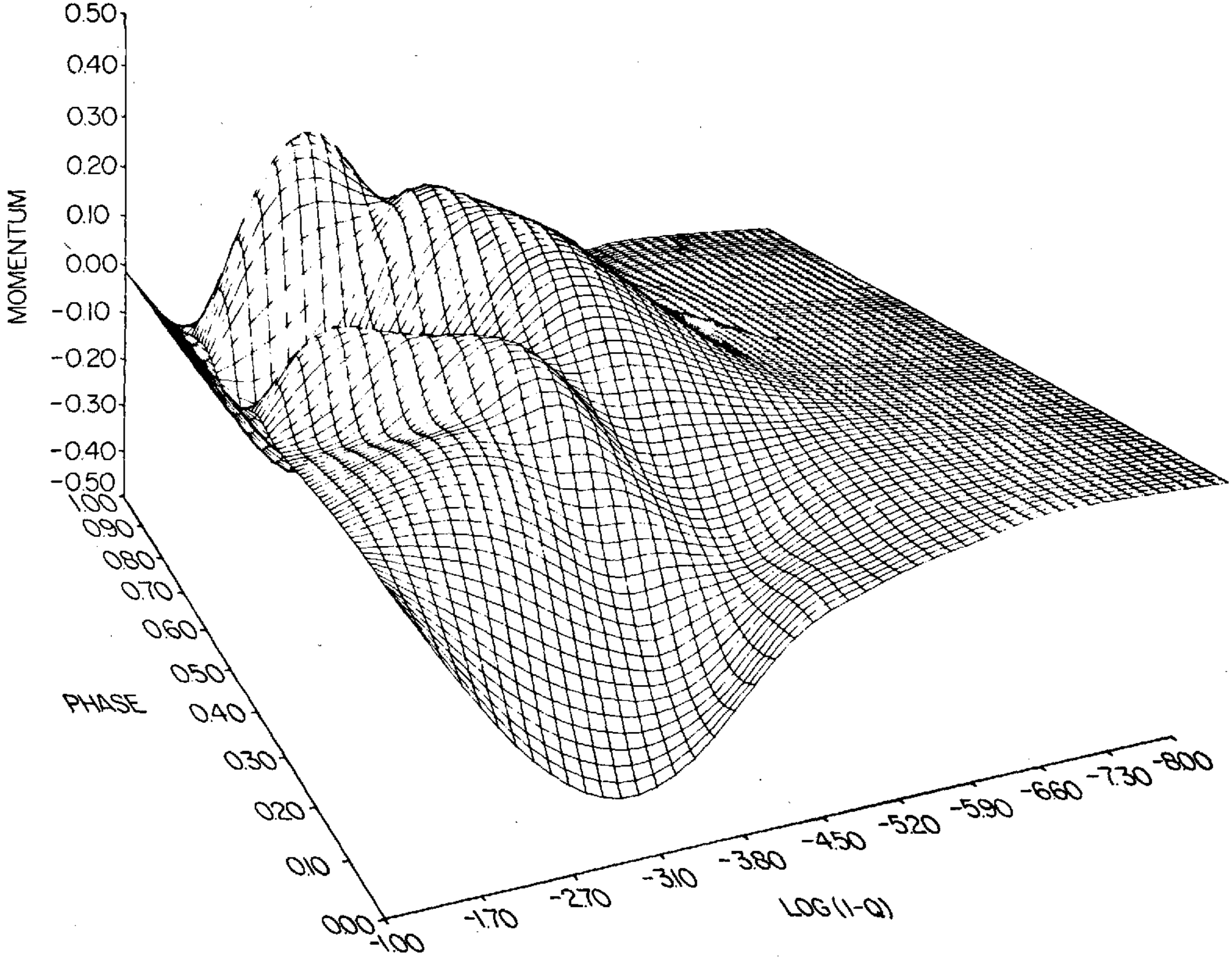

Figure VII -1. Momentum vs. mass point and phase.

APPENDIX A

COEFFICIENTS OF THE INCREMENTS--DIFFUSION APPROXIMATION

The nonvanishing coefficients of the increments as derived by G. S. Kutter and W. M. Sparks used in the diffusion approximation calculations are listed. These coefficients are denoted by the symbol DET followed by two numbers. The first of these refers to the differential equation (II-1 to II-5). The second number runs from 0 to 10, where 0 refers to the inhomogeneous term, and 1 to 10 identify the coefficients of δv_{i-1}, δB_{i-1}, δR_{i-1}, $\delta W_{i-1/2}$, $\delta Z_{i-1/2}$, δv_i, δB_i, δR_i, $\delta W_{i+1/2}$, $\delta Z_{i+1/2}$, respectively. For instance, the conservation of mass equation (II-1) has the form

$$\mathrm{DET13} \cdot \delta R_{i-1} + \mathrm{DET14} \cdot \delta W_{i-1/2} + \mathrm{DET18} \cdot \delta R_i = \mathrm{DET10}.$$

$i = 2$:

The coefficients are identical to those listed below for $i = 3, \ldots, N$ except for

$$\mathrm{DET13} = \mathrm{DET32} = 0.$$

$i = 3, \ldots, N$:

$$\mathrm{DET13} = \mathrm{CON1}_{i-1/2}\, r_{i-1}^3,$$

$$\mathrm{DET14} = V_{i-1/2}$$

$$\mathrm{DET18} = -\mathrm{CON1}_{i-1/2}\, r_i^3,$$

$$\mathrm{DET10} = -V_{i-1/2} + \frac{1}{3}\,\mathrm{CON1}_{i-1/2}\,(r_i^3 - r_{i-1}^3),$$

$$\mathrm{CON1}_{i-1/2} = -4\pi[M_0(Q_i - Q_{i-1})]^{-1};$$

$$\mathrm{DET24} = (1 - \theta)Y2_i^n \left[\frac{2q_{i-1/2}^{n+1/2}\, V_{i-1/2}}{V_{i-1/2}^n(W_{i-1/2} - W_{i-1/2}^n)}\right]$$

$$+ \theta Y2_i \left[P_{i-1/2} \frac{\partial \Pi}{\partial W}\bigg|_{Z_{i-1/2}} - q_{i-1/2}^{n+1/2} \left(1 - \frac{2}{W_{i-1/2} - W_{i-1/2}^n}\right)\right],$$

$$\mathrm{DET25} = \theta Y2_i\, P_{i-1/2} \frac{\partial \Pi}{\partial Z}\bigg|_{W_{i-1/2}} ,$$

$$\mathrm{DET26} = 1/\Delta t^{n+1/2} ,$$

$$\mathrm{DET28} = -2\theta\left[Y2_i(P_{i+1/2} + q_{i+1/2}^{n+1/2} - P_{i-1/2}^{n+1/2} + \frac{Gm_i}{r_i^2}\right] ,$$

$$\mathrm{DET29} = -(1-\theta)\; Y2_i \left[\frac{2q_{i+1/2}^{n+1/2}\, V_{i+1/2}}{V_{i+1/2}^n\;(W_{i+1/2} - W_{i+1/2}^n)}\right]$$

$$-\theta Y2_i \left[P_{i+1/2} \frac{\partial \Pi}{\partial W}\bigg|_{Z_{i+1/2}} + q_{i+1/2}^{n+1/2} \left(1 - \frac{2}{W_{i+1/2} - W_{i+1/2}^n}\right)\right],$$

$$\mathrm{DET210} = -\theta Y2_i\, P_{i+1/2} \frac{\partial \Pi}{\partial Z}\bigg|_{W_{i+1/2}} ,$$

$$\mathrm{DET20} = -\frac{u_i - u_i^n}{\Delta t^{n+1/2}} + (1 - \theta)\left[F_i^n + Y2_i^n \left(q_{i+1/2}^{n+1/2} \frac{V_{i+1/2}}{V_{i+1/2}^n}\right.\right.$$

$$\left.\left.-q_{i-1/2}^{n+1/2} \frac{V_{i-1/2}}{V_{i-1/2}^n}\right)\right] + \theta\left[F_i + Y2_i \left(q_{i+1/2}^{n+1/2} - q_{i-1/2}^{n+1/2}\right)\right] ,$$

$$Y2_i = 4\pi\, r_i^2\, [M_o Q_i(S_{i+1/2} - S_{i-1/2})]^{-1};$$

$$\mathrm{DET32} = \theta L_\Theta\, [M_o Q_{i-1/2}\, (S_i - S_{i-1})]^{-1} ,$$

$$\mathrm{DET34} = \frac{1}{\Delta t^{n+1/2}} \left\| \frac{\partial E}{\partial W}\Big|_{Z_{i-1/2}} + (1-\theta)\, P^{n}_{i-1/2}\, V^{n}_{i-1/2} + \theta V_{i-1/2} \left\{ P_{i-1/2} \left[1 + (W_{i-1/2} - W^{n}_{i-1/2}) \left(1 + \frac{\partial \Pi}{\partial W}\Big|_{Z_{i-1/2}} \right) \right] + 3q^{n+1/2}_{i-1/2} \right\} \right\| ,$$

$$\mathrm{DET35} = \frac{1}{\Delta t^{n+1/2}} \left[\frac{\partial E}{\partial Z}\Big|_{W_{i-1/2}} + \theta P_{i-1/2} V_{i-1/2} (W_{i-1/2} - W^{n}_{i-1/2} \quad \frac{\partial \Pi}{\partial Z}\Big|_{W_{i-1/2}} \right.$$

$$\mathrm{DET37} = -\,\mathrm{DET32} ,$$

$$\mathrm{DET30} = (1-\theta)\, G^{n}_{i-1/2} + \theta G_{i-1/2} - \frac{1}{\Delta t^{n+1/2}} \left[E_{i-1/2} - E^{n}_{i-1/2} + q^{n+1/2}_{i-1/2}\; V_{i-1/2}\; (W_{i-1/2} - W^{n}_{i-1/2}) \right] ;$$

$$G_{i-1/2} = \frac{L_{\Theta}}{M_{o} Q_{i-1/2}} \; \frac{B_i - B_{i-1}}{S_i - S_{i-1}} - P_{i-1/2}\, V_{i-1/2} \; \frac{W_{i-1/2} - W^{n}_{i-1/2}}{\Delta t^{n+1/2}} ;$$

$$\mathrm{DET44} = -\frac{1}{2}\; Y4_i \; \frac{\partial \kappa}{\partial W}_{Z_{i-1/2}} \; (Z_{i+1/2} - Z_{i-1/2}) ,$$

$$\mathrm{DET45} = Y4_i \left[2 - \frac{1}{2}\; \frac{\partial \kappa}{\partial Z}\Big|_{W_{i-1/2}} (Z_{i+1/2} - Z_{i-1/2}) - 1 \right] ,$$

$$\mathrm{DET47} = -1$$

$$\mathrm{DET48} = 4Y4_i (Z_{i+1/2} - Z_{i-1/2}) ,$$

$$\mathrm{DET49} = \frac{1}{2}\; Y4_i \; \frac{\partial \kappa}{\partial W}\Big|_{Z_{i+1/2}} (Z_{i+1/2} - Z_{i-1/2}) ,$$

$$\mathrm{DET410} = Y4_i \left[2 - \frac{1}{2}\; \frac{\partial \kappa}{\partial Z}\Big|_{W_{i+1/2}} (Z_{i+1/2} - Z_{i-1/2}) + 1 \right]$$

$$\mathrm{DET40} = B_i - Y4_i \; (Z_{i+1/2} - Z_{i-1/2}),$$

$$Y4_i = \frac{256\,\sigma\pi^2}{3L_\Theta \; M_o \; Q_i(S_{i+1/2} - S_{i-1/2}} \quad \frac{r_i^4 T_i^4}{\kappa_i} \quad ;$$

$$\mathrm{DET56} = -\theta / r_i \quad ,$$

$$\mathrm{DET58} = \frac{1}{\Delta t^{n+1/2}} \; + \theta \, \frac{u_i}{r_i} \quad ,$$

$$\mathrm{DET50} = - \frac{R_i - R_i^n}{\Delta t^{n+1/2}} + (1 - \theta) \, \frac{u_i^n}{r_i^n} \; + \; \frac{\theta u_i}{r_i} \quad .$$

$i = N + 1$:

The coefficients of equations 1, 3 and 5 are identical to those listed above for $i = 1, \ldots, N$ as are DET24, DET25, and DET26 except for the definition of $Y2_{N+1}$ given below.

$$\mathrm{DET28} = 2\theta \left[Y2_{N+1} \; (P_{N+1/2} - P_o + q_{N+1/2}^{n+1/2} \;) - \frac{GM_o}{r_{N+1}^2} \right] \quad ,$$

$$\mathrm{DET29} = \mathrm{DET210} = 0$$

$$\mathrm{DET20} = - \frac{u_{N+1} - u_{N+1}^n}{\Delta t^{n+1/2}} \; + \; (1 - \theta) \left(F_{N+1} - Y2_{N+1}^n \; q_{N+1/2}^{n+1/2} \; \frac{V_{i+1/2}}{V_{i+1/2}^n} \right)$$

$$+ \; \theta \left(F_{N+1} - Y2_{N+1} \; q_{N+1/2}^{n+1/2} \right) ,$$

$$Y2_{N+1} = 4\pi \; r_{N+1}^2 \; [M_o (Q_{N+1} - Q_{N+1/2})]^{-1} \quad ,$$

$$P_o = P_{N+1/2} \quad \alpha$$

$$\alpha \; = (m_{N-1/2} - m_{N+1/2}) / (m_{N-3/2} - m_{N-1/2});$$

$$\mathrm{DET44} = -Y4_{N+1} \quad YYY4_{N+1} \; \frac{\partial \kappa}{\partial W} \Bigg|_{Z_{N+1/2}} \quad ,$$

$$DET45 = -Y4_{N+1}\ \left(YYY4_{N+1}\ \frac{\partial\kappa}{\partial Z}\Big|_{W_{N+1/2}} - 4\right) \quad ,$$

$$DET47 = -1$$

$$DET48 = 2Y4_{N+1}\ \left(\frac{3}{4}\ YYY4_{N+1} + 1\right) \quad ,$$

$$DET49 = DET410 = 0$$

$$DET40 = B_{N+1} - Y4_{N+1}$$

$$Y4_{N+1} = \frac{16\pi\sigma}{3L_{\odot}}\ \frac{r^{2}_{N+1}\ T^{4}_{N+1/2}}{YY4_{N+1} + 2/3} \quad ,$$

$$YY4_{N+1} = -\frac{M_{o}}{4\pi}\ (Q_{N+1} - Q_{N+1/2})\ \frac{\kappa_{N+1/2}}{2(r^{3}_{N+1}\ r_{N})^{1/2}} \quad ,$$

$$YYY4_{N+1} = \frac{YY4_{N+1}}{YY4_{N+1} + 2/3}$$

APPENDIX B

COEFFICIENTS OF THE INCREMENTS— RADIATIVE TRANSFER

The coefficients of the increments that are changed to include radiative transfer effects are listed. The notation is defined in Appendix A.

$i = 2, \ldots, N$:

$$\mathrm{DET40} = B_i - B_{R_i} \quad ,$$

$$\mathrm{DET44} = F1_i(\mathrm{DET44})_D \quad ,$$

$$\mathrm{DET45} = F1_i(\mathrm{DET45})_D \quad ,$$

$$\mathrm{DET48} = 0 \quad ,$$

$$\mathrm{DET49} = F2_i(\mathrm{DET49})_D \quad ,$$

$$\mathrm{DET410} = F2_i(\mathrm{DET410})_D \quad ,$$

$$B_{R_i} = 16\pi^2\, r_{\mathrm{eff}}^2 \int_{-1}^{1} I\, \mu d\mu \quad ,$$

$$r_{\mathrm{eff}} = \begin{cases} r_i & \text{if } \tau_i \geqslant 10 \quad , \\ r_a & \text{if } \tau_i < 10 \quad , \end{cases}$$

r_a = radius of deepest zone with $\tau < 10$,

$$F1_i = \begin{cases} 1 & \text{if } \tau_i \geqslant 10 \quad , \\ 1-e^{-\Delta\tau_i} & \text{if } \tau_i < 10 \quad , \end{cases}$$

$$F2_i = \begin{cases} 1 & \text{if } \tau_i \geqslant 10 \quad , \\ 1-e^{-\Delta\tau_{i+1}} & \text{if } \tau_i < 10 \quad , \end{cases}$$

$$\Delta\tau_i = \frac{1}{2}(\tau_i - \tau_{i+2}).$$

$i = N + 1$:

$$DET40 = B_{N+1} - B_{R_{N+1}} \quad ,$$

$$DET44 = F2_{N+1}(DET44)_D \quad ,$$

$$DET45 = F2_{N+1}(DET45)_D \quad ,$$

$$DET48 = 0 \quad ,$$

$$F2_{N+1} = 1 - e^{-\tau_N} \quad .$$

A subscript D denotes the quantity was computed using the formula in Appendix A.

APPENDIX C

ELECTRON PRESSURE ITERATION PROCEDURE

The electron pressure P_e is important for determining the emergent spectrum since it affects the ionization balance through the Saha equation. P_e, though, also depends on the number of free electrons, $P_e = N_e\,kT$. Therefore, an iterative procedure must be used to find P_e from the known temperature and density. The iteration used here can be written as

$$P_e^{(k)} = \frac{\alpha_1 + \alpha_2}{[\alpha_2/P_e^{(k-1)}] - 1} \quad ,$$

where k counts the number of iterations,

$$P_e^{(0)} = \frac{1}{2} P_N = \frac{1}{2} \frac{\rho kT}{\mu m_H} \quad ,$$

$$\alpha_1 = P_N \sum_{i=1}^{N} \gamma_i Y_i / X_i \quad ,$$

$$\alpha_2 = P_N \sum_{i=1}^{N} \gamma_i (Y_i^2 - X_i Z_i)/X_i^2 \quad ,$$

$$\gamma_i = \text{number fraction of element } i \quad ,$$

$$X_i = 1 + \sum_{j=1}^{4} f_{ij} \quad ,$$

$$Y_i = \sum_{j=1}^{4} j f_{ij} \quad ,$$

$$Z_i = \sum_{j=1}^{4} j^2 f_{ij} \quad ,$$

$$f_{ij} = \prod_{n=1}^{j} \frac{N_{i,n+1}}{N_{i,n}} .$$

Convergence of this iteration is quadratic and global.

Plate 1. Luminosity vs. mass point and phase. Bright areas represent large luminosity; dark areas, low luminosity. Base of the envelope is at the top; surface, at the bottom. Two periods are shown.

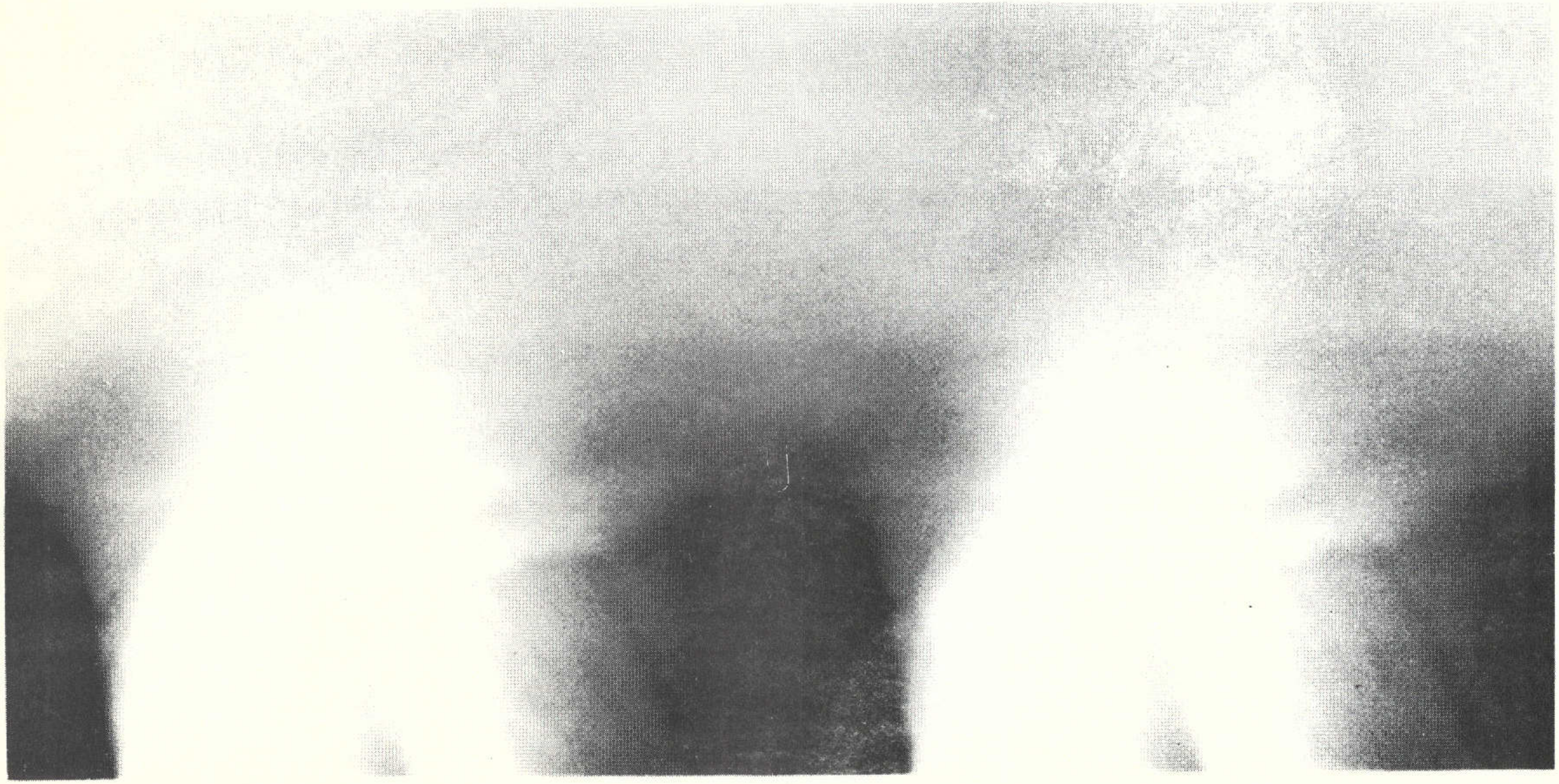

Plate II. Velocity vs. mass point and phase. Bright areas indicate expansion; dark areas contraction. Base of the envelope is at the top; surface at the bottom. Two periods are shown.

LITERATURE CITED

Abhyankar, K. D., 1964a, Astrophys. Journ., 140, 1353.

Abhyankar, K. D., 1964b, Astrophys. Journ., 140, 1368.

Abt, H. A., 1957, Astrophys. Journ., 126, 138.

Abt, H. A., 1958, Astrophys. Journ., 127, 658.

Abt, H. A., 1959, Astrophys. Journ., 130, 824.

Allen, C. W., 1963, Astrophysical Quantities, (London: Athlone Press).

Andersen, P. H., 1973, Pub. Astron. Soc. Pacific, 85, 666.

Arakelyan, M. A., 1969, Astrofizika, 5, 75.

Aydin, C., 1972, Astron. Astrophys., 19, 369.

Azusienis, A., and Straizys, V., 1969, Soviet Astron. Journ., 13, 316.

Baade, W., 1926, Astr. Nachr., 228, 359.

Baade, W., 1956, Pub. Astron. Soc. Pacific, 68, 5.

Baker, N., 1967, (quoted by King and Cox, 1968).

Baker, N., and Kippenhahn, R., 1962, Zeit.für Astrophys., 54, 114.

Baker, N., and Kippenhahn, R., 1965, Astrophys. Journ., 142, 868.

Becker, W., 1940, Zeit.für Astrophys., 19, 289.

Bell, R. A., 1974, unpublished.

Bell, R. A., and Parsons, S. B., 1974, in press.

Bell, R. A., and Rodgers, A. W., 1964, Mon. Not. R. Astr. Soc., 128, 365.

Bell, R. A., and Rodgers, A. W., 1967, Mon. Not. R. Astr. Soc., 135, 121.

Belopsky, A., 1895, Astrophys. Journ., 1, 160.

Bendt, J. E., and Davis, C. G., 1971, Astrophys. Journ., 169, 333.

Böhm-Vitense, E., 1972, Astron. Astrophys., 17, 335.

Bottlinger, K. F., 1928, Astron. Nach., 232, 3.

Caputo, F., and Natta, A., 1973, Astrophys. Space Science, 21, 73.

Carroll, J. A., 1928, Mon. Not. R. Astr. Soc., 88, 548.

Carroll, L., 1865, Alice's Adventures in Wonderland, (New York: Mac Millan).

Castor, J. I., 1968, Astrophys. Journ., 154, 793.

Chandrasekhar, S., 1945, Rev. Mod. Phys., 17, 138.

Christy, R. F., 1962, Astrophys. Journ., 136, 887.

Christy, R. F., 1968, Quarterly Journ. R. Astr. Soc., 9, 13.

Christy, R. F., 1969, Journ. R. Astr. Soc. Canada, 63, 299.

Christy, R. F., 1970, Journ. R. Astr. Soc. Canada, 64, 8.

Ciurla, T., 1966, Acta Astron., 16, 249.

Cogan, B. C., 1970, Astrophys. Journ., 162, 139.

Cox, A. N., and Wing, J. E., 1973, Bull. Amer. Astron. Soc., 5, 428.

Cox, J. P., 1963, Astrophys. Journ., 138, 487.

Cox, J. P., Cox, A. N., Olsen, K. H., King, D. S., and Eilers, D. D., 1966, Astrophys. Journ., 144, 1038.

Cox, J. P., and Giuli, R. T., 1968, Principles of Stellar Structure, (New York: Gordon and Breach).

Cox, J. P., King, D. S., and Stellingwerf, R. F., 1972, Astrophys. Journ., 171, 93.

Davis, C. G., 1971, Journ Quant. Spectrosc. Radiat. Transfer, 11, 647.

Dawe, J. A., 1969, Mon. Not. R. Astr. Soc., 145, 377.

DeLoore, C., 1970, Astrophys. Space Science, 6, 60.

Duquesne, J., and Schatzman, E., 1955, Ann. d'Astrophys., 18, 279.

Eddington, A. S., 1917, Observatory, 40, 290.

Eddington, A. S., 1918, Mon. Not. R. Astr. Soc., 79, 2.

Eddington, A. S., 1926, The Internal Constitution of the Stars, (Cambridge: Cambridge University Press).

Eoll, J. G., 1973, Bull. Amer. Astron. Soc., 5, 1.

Epstein, I., 1950, Astrophys. Journ., 112, 6.

Evans, J. C., and Schroeder, L. W., 1972, Pub. Astron. Soc. Pacific, 84, 454.

Fernie, J. D., 1968, Astrophys. Journ., 151, 197.

Fernie, J. D., 1969, Pub. Astron. Soc. Pacific, 81, 707.

Fernie, J. D., and Hube, J. O., 1967, Pub. Astron. Soc. Pacific, 79, 95.

Fricke, K., Stobie, R. S., and Strittmatter, P. A., 1971, Mon. Not. R. Astr. Soc., 154, 23.

Fricke, K., Stobie, R. S., and Strittmatter, P. A., 1972, Astrophys. Journ., 171, 593.

Getting, I. A., 1935, Mon. Not. R. Astr. Soc., 95, 139.

Goddricke, J., 1786, Phil. Trans., 76, 48 (as quoted by Rosseland 1949).

Gough, D. O. Ostriker, J. P., and Stobie, R. S., 1965, Astrophys. Journ., 142, 1649.

Grenfell, T. C., and Wallerstein, G., 1969, Pub. Astron. Soc. Pacific, 81, 732.

Hearn, A. G., 1974, Astron. Astrophys., 31, 415.

Henyey, L. G., Forbes, J. E., and Gould, N. L., 1964, Astrophys. Journ., 139, 306.

Hertzsprung, E., 1913, Astron. Nach., 196, 201.

Hertzsprung, E., 1926, Bull. Astron. Netherlands, 3, 115 (quoted by Rosseland 1949).

Hillendahl, R. W., 1968, Ph.D. Thesis, University of California, Berkeley.

Hillendahl, R. W., 1969, Astrophys. Letters, 4, 179.

Hillendahl, R. W., 1970, Pub. Astron. Soc. Pacific., 82, 1231.

Hoof, A. van, and Deurinck, R., 1952, Astrophys. Journ., 115, 166.

Huang, S.-S., and Struve, O., 1960, "Stellar Rotation and Atmospheric Turbulence," in Stellar Atmospheres, ed. J. L. Greenstein, (Chicago: University of Chicago Press).

Hutchinson, J. L., 1974, in press.

Iben, I., Jr., 1966, Astrophys. Journ., 143, 483.

Iben, I., Jr., and Tuggle, R. S., 1972a, Astrophys. Journ., 173, 135.

Iben, I., Jr., and Tuggle, R. S., 1972b, Astrophys. Journ., 178, 441.

Johnson, H. L., 1964, Astrophys. Journ., 141, 923.

Jung, J., 1970, Astron. Astrophys., 6, 130.

Karp, A. H., 1973, Astrophys. Journ., 180, 895.

Keller, C. F., and Mutschlecner, J. P., 1970, Astrophys. Journ., 161, 217.

Keller, C. F., and Mutschlecner, J. P., 1971, Astrophys. Journ., 167, 127.

King, D. S., 1972, unpublished.

King, D. S., and Cox, J. P., 1968, Pub. Astron. Soc., Pacific., 80, 365.

King, D. S., Cox, J. P., Eilers, D. D., and Davey, W. R., 1973, Astrophys. Journ., 182, 859.

Kippenhahn, R., Weigert, A., and Hofmeister, E., 1967, "Methods for Calculating Stellar Evolution," in Methods in Computational Physics, 7 ed. B. Adler, S. Fernbach, and M. Rotenberg, (New York: Academic Press).

Kourganoff, V., 1952, Basic Methods in Transfer Problems, (Oxford: Clarendon Press).

Kraft, R. P., 1961, Astrophys. Journ., 134, 616.

Kraft, R. P., 1966, Astrophys. Journ., 144, 1008.

Kraft, R. P., 1967, "The Line Spectrum of Pulsating Variable Stars," in Aerodynamic Phenomena in Stellar Atmospheres, IAU Symp. 28, ed. R. N. Thomas, (Berlin: Springer-Verlag).

Kraft, R. P., and Schmidt, M., 1963, Astrophys. Journ., 137, 249.

Kubiowski, J., and Ciurla, T., 1965, Acta Astron., 15, 177.

Kutter, G. S., and Sparks, W. M., 1972, Astrophys. Journ., 175, 407.

Lamb, H., 1932, Hydrodynamics, (New York: Dover).

Latour, J., 1970, Astron. Astrophys., 9, 277.

Ledoux, P., and Walraven, Th., 1958, "Variable Stars," in Handbuch der Physik, 51, ed. S. Flügge, (Berlin: Springer-Verlag).

Nikolov, N. S., 1968, Catalog of the Light and Color Curves of Cepheids in the UBV System, (Sofia: Bulgarian Academy of Sciences Press).

Nikolov, N. S., and Kunchev, P., 1969, Astrophys. Space Science, 3, 46.

Nikolov, N. S., and Tsvetkov, Ts., 1972, Astrophys. Space Science, 16, 445.

Oke, J. B., 1961a, Astrophys. Journ., 133, 90.

Oke, J. B., 1961b, Astrophys. Journ., 134, 214.

Oke, J. B., Giver, L. P., and Searle, L., 1962, Astrophys. Journ., 136, 393.

Osmer, P. S., 1972, Astrophys. Journn. Suppl., 24, 255.

Ortega, J. M., 1972, Numerical Analysis, (New York: Academic Press).

Paradijs, J. van, 1972, Nature Physical Science, 238, 37.

Parsons, S. B., 1969, Astrophys. Journ. Suppl., 18, 127.

Parsons, S. B., 1971a, Astron. Journ., 76, 562.

Parsons, S. B., 1971b, Mon. Not. R. Astr. Soc., 152, 121.

Parsons, S. B., 1971c, Astrophys. Journ., 164, 355.

Parsons, S. B., 1972, Astrophys. Journ., 174, 57.

Parsons, S. B., and Bouw, G. D., 1971, Mon. Not. R. Astr. Soc., 152, 133.

Payne-Gaposhkin, C., 1951, in Astrophysics, ed. J. A. Hynek, (New York: McGraw-Hill).

Pickering, E. C., 1912, Harvard Circ. No. 173, (quoted by Fernie 1969).

Richtmeyer, R. D., and Morton, K. W., 1967, Difference Methods for Initial Value Problems, (New York: Interscience).

Ritter, A., 1879, Hiedemanns Annalen, 8, 172 (quoted by Rosseland 1949).

Rodgers, A. W., 1970, Mon. Not. R. Astr. Soc., 151, 133.

Rodgers, A. W., and Bell, R. A., 1964, Mon. Not. R. Astr. Soc., 127, 471.

Rodgers, A. W., and Bell, R. A., 1968, Mon. Not. R. Astr. Soc., 138, 23.

Rose, W. K., and Smith, R. L., 1970, Astrophys. Journ., 159, 903.

Rose, W. K., and Smith, R. L., 1972, Astrophys. Journ., 173, 385.

Rosendahl, J. D., and Wegner, G., 1970, Astrophys. Journ., 162, 547.

Rosseland, S., 1949, The Pulsation Theory of Variable Stars, (Oxford: Clarendon Press).

Sandage, A., and Tammann, G. A., 1969, Astrophys. Journ., 157, 683.

Sanford, R. F., 1956, Astrophys. Journ., 123, 201.

Schaltenbrand, R., and Tammann, G. A., 1971, Astron. Astrophys. Suppl., 4, 265.

Schmidt. E. G., 1970, Astrophys. Journ., 162, 871.

Schmidt, E. G., 1971a, Astrophys. Journ., 165, 335.

Schmidt, E. G., 1971b, Astrophys. Journ., 170, 109.

Schmidt, E. G., 1973, Mon. Not. R. Astr. Soc., 163, 67.

Schmidt, E. G., 1974, Mon. Not. R. Astr. Soc., 167, 613.

Schwartzchild, M., Schwartzchild, B., and Adams, W. S., 1948, Astrophys. Journ., 108, 207.

Shapley, H., 1914, Astrophys. Journ., 40, 448.

Shapley, H., 1918, Astrophys. Journ., 48, 89.

Shapley, H., and Nicholson, S. B., 1919, Proc. Nat. Acad. Sci., 5, 417, (quoted by Parsons, 1972).

Skalafuris, A. J., 1974, Astrophys. Journ., 190, 91.

Stebbins, J., Kron, G. E., and Smith, J. L., 1952, Astrophys. Journ., 115, 292.

Stibbs, D.W.N., 1955, Mon. Not. R. Astr. Soc., 115, 363.

Stobie, R. S., 1969a, Mon. Not. R. Astr. Soc., 144, 461.

Stobie, R. S., 1969b, Mon. Not. R. Astr. Soc., 144, 485.

Stobie, R. S., 1969c, Mon. Not. R. Astr. Soc., 144, 511.

Struve, O., 1932, Pro. Nat. Acad. Sci., 18, 585 (quoted by Huang and Struve 1960).

Struve, O., and Elvey, C. T., 1934, Astrophys. Journ., 79, 409.

Underhill, A. B., 1947, Astrophys. Journ., 106, 128.

Van Genderen, A. M., 1970, Astron. Astrophys., 7, 244.

Wallerstein, G., 1972, Pub. Astr. Soc. Pacific, 84, 656.

Wesselink, A. J., 1946, Bull. Astr. Netherlands, 10, 91.

Whitney, C. A., 1955, Astrophys. Journ., 121, 682.

Whitney, C. A., 1956, Ann. d'Astrophys., 18, 375.

Whitney, C. A., 1967, in Aerodynamic Phenomena in Stellar Atmospheres, IAU Symp. 28, ed. R. N. Thomas, (Berlin: Springer-Verlag).

Wielen, R., 1974, Astron. Astrophys. Suppl., 15, 1.

Wisniewski, Z., and Johnson, H. L., 1968, Comm Lunar and Planet. Lab., 7, 57.

Wright, K. O., 1946, Journ. R. Astr. Soc. Canada, 40, 183.

Woolley, R., and Carter, B., 1973, Mon. Not. R. Astr. Soc., 162, 379.

Woolley, R., and Savage, A., 1971, R. Obs. Bull., 170, 365.

Worrall, G., and Wilson, A. M., 1972, Nature, 236, 15.

Zhevakin, S. A., 1953, Astr. Zh., 30, 161 (quoted by Zhevakin 1963).

Zhevakin, S. A., 1963, Ann. Rev. Astron. Astrophys., 1, 367.